EXPERIMENTAL AND THEORETICAL INVESTIGATION OF ROTORDYNAMIC INSTABILITY IN A SHROUDED TURBINE

by

Taras Andrew Palczynski Jr.

B.S. Mechanical Engineering
The Cooper Union for the Advancement of Science and Art, 1990

Submitted to the Department of Aeronautics and Astronautics
in Partial Fulfillment of the Requirements for the Degree of

MASTER OF SCIENCE

at the
MASSACHUSETTS INSTITUTE OF TECHNOLOGY
August 1992

Signature of Author _____
Department of Aeronautics and Astronautics
August 13, 1992

Certified by _____
Professor Manuel Martinez-Sanchez
Associate Professor of Aeronautics and Astronautics
Thesis Supervisor

Accepted by _____
Professor Harold Y. Wachman
Chairman, Departmental Graduate Committee

EXPERIMENTAL AND THEORETICAL INVESTIGATION OF ROTORDYNAMIC INSTABILITY IN A SHROUDED TURBINE

by

Taras Andrew Palczynski Jr.

Submitted to the Department of Aeronautics and Astronautics on
August 13, 1992 in Partial Fulfillment of the Requirements for the Degree of
Master of Science at the Massachusetts Institute of Technology

ABSTRACT

The destabilizing force responsible for rotordynamic instability in a shrouded turbine has been measured experimentally and determined theoretically. The experiments were done in a closed loop, freon based facility where the turbine rotor was capable of being statically displaced up to 0.457 mm (18 mils) from its concentric rotating position. The turbine was operated at its design speed of 3440 rpm and at two off design speeds of 2408 rpm and 3784 rpm where the mass flow rate and inlet stagnation pressure was kept constant at 3.15 kg/s and 2.21 atm respectively. At these three speeds measurements of the forces in the direction of displacement (a restoring force) and perpendicular to the direction of displacement (potentially destabilizing force) were achieved by using a system of strain gauges mounted in the rotor's shaft directly below the rotor. These forces were also measured by analyzing the pressure distribution around the outer circumference of the shroud. The data from strain gauge measurements were repeatable and for operation at design with eccentricities varying from -0.381 mm (-15 mils) to +0.381 mm (+15 mils) the magnitude of the destabilizing force was found to be linear with magnitudes from -5.56 N (-1.25 lbf) to 15.57 N (3.50 lbf). The destabilizing forces calculated from pressure measurements for operation at design were found to be smaller than strain gauge results, which was expected, due to not accounting for the contribution from the aerodynamic effects (The Alford Force).

The theoretical model is based on the work of Kostyuk, Iwatsubo and Millsaps and is an attempt to model the shroud of this turbine. This model is one-dimensional in the circumferential direction and is coupled to the axial mass flow rate. A linear perturbation approximation with harmonic solutions is used to arrive at a system of two algebraic equations with two unknowns. The solution predicts the pressure and velocity nonuniformity within the cavity of the shroud. The model is extended to include the effect of inlet and exit pressure and velocity nonuniformities. This allows one to analyze the effect these nonuniformities have on the model's prediction of the pressure and velocity perturbation in the cavity. It was found that the inlet and exit nonuniformities have a large effect on the model's predictions by increasing the magnitude of both the restoring force and the destabilizing force.

The results of both experiment and theory were compared and it was found that the model still under predicts the experimentally measured forces. However, the inclusion of the model's dependence on inlet and exit pressure and velocity nonuniformities have brought the model's predictions of the forces to within 37% of experiment compared to 220% before the inclusion of these nonuniformities. It was proven that the discrepancy between theory and experiment are not due to the nonlinear effects. A fourth order Runge-Kutta numerical solution to the time independent (non-whirling, statically offset) nonlinear system of ordinary differential equations was completed. The nonlinear results are very close to those results obtained from the linearized solution.

Thesis Supervisor: Dr. Manuel Martinez-Sanchez
Title: Associate Professor of Aeronautics and Astronautics

Acknowledgments

I will always be in debt to Professor Manuel Martinez-Sanchez for directing me through the many obstacles that have arisen in completing this work. He has always supplied a wealth of information and, what is more important, had the time to make sure I understood those ideas. He has presented himself both as a strong advisor and as a friend who understood the problems and was there to help me through them. Thank You!

S. J. Song has been a fantastic worker and great experimental researcher. Since the start of this project he has always been there to explain the workings of both the experimental facility and M.I.T. in general. I wish to express sincere gratitude to S. J. for all of his help. I also consider him to be a good friend and hope he has success in all of his future endeavors.

I wish to extend many thanks to Knox Millsaps (now Doctor Millsaps) for the many hours he spent explaining the analytical model to me. He must be commended for both his teaching style and friendly approach.

The experimental project would have never succeeded without the help of Viktor Dubrowski. His machining talent along with his general knowledge on the workings of almost anything has made the difference between a disaster and the completion of this work. I thank Viktor for all his help and especially for his never ending smile.

Soomyung Yoo has been a great help and I thank him for all of his useful contributions that literally saved me hundreds of hours.

I thank Doctor B. Jery for his contributions while he was here.

My friends at the Gas Turbine Lab have made my stay here enjoyable. Aaron Gleixner has become a close friend who's exploits have not only entertained me but many others here in the Lab. I thank him for the rides in the plane and for taking Tatiana and me on all those road trips. David Tew's friendship extends beyond that of office mate. He has shown me the importance of relaxing occasionally and in the process illustrated the power of the parking brake. Peter "Garage" Silkowski has been both a great friend and a good work out partner. He had many good ideas on lifting techniques and I hope he continues to lift in the future. I wish you the best in your future plans.

I thank the lunch crowd: Aaron Gleixner, Dave Tew, Peter Silkowski, Knox Millsaps, Dan Gysling and Jon Simon for making the day more enjoyable.

My cousin Victor Kruchowy deserves many thanks for taking time to visit me in Boston and for treating me to dinner and beers. I wish him the best in his graduate work. My future brother in-laws Borys and Evon Wenglowskyj have made my vacations in Miami extremely enjoyable. I thank them for the laughs and I thank Borys for just being himself. Evon and I hope that Borys keeps out of those newspaper headlines and movie titles.

Never ending thanks and love go to my grandparents, parents and sisters. All four of my grandparents have supported me in many ways throughout my time away from home and I will always be grateful to them. I am especially thankful to grandpa and my father, for purchasing the computer that helped me in my studies. My mother has always been there to help me through the difficult times while my father always took the time to make sure I continue to explore my full potential. They have always given and never asked for anything in return. I will always be in debt to them for all of their love and caring. The older of my two sisters, Verusha has cheered up many gloomy days with all of her stories of blond experiences. Continue to "Ladder" along and watch for guys falling on the hood of your car when you begin to drive. I wish the best for you in College and I know you will be at the top of your class as you always have been. My youngest sister, Natalka, a kindred spirit whom I really can't call "Shrimpo" any longer, has always been able to make me laugh. Sub's are our favorite topic. For such a very young lady to have so very much sophistication is amazing especially when her name doesn't even end with an "e". Junior high will be as easy as grammar school was for you and I know you will make Valedictorian again.

My fiancee, Tatiana "Tots" Wenglowskyj, has been a wealth of love and caring throughout. She has always put me first and I will never be able to repay her for all that she has done. I will always have the utmost respect and love for her. She has patiently put up with my obsessive work behavior and has always understood why many exciting plans had to be canceled so that I could work or study. I hope I can be as helpful to her as she was to me when she continues with her studies.

My master's education was made possible by the Air Force Research in Aero Propulsion Technology Scholarship under grant # AFOSR-91-0052. Daniel J. Fant Major U. S. A. F. was monitor The experimental project was funded by NASA Marshal Space Flight Center under contract # NAS8-35018. The technical monitor was Mr. Glen Wilmer. I thank these people for the opportunity to advance my education.

Table of Contents

List of Figures

List of Tables

Nomenclature

Variable	Description	Units
a	Square of the ratio of stator blade height to the rotor blade height	-
a_s	Speed of sound	m/s
A_1	Effective area	m^2
$[B]$	Calibration matrix	N/volts
B_H	Rotor Blade height	m
c	Chord length	m
c_x	Axial flow velocity	m/s
C_c	Contraction coefficient	-
C_{xx}	Damping in the x-direction from a x displacement due to fluid interaction	N·s/m
C_{xy}	Damping in the x-direction from a y displacement due to fluid interaction	N·s/m
C_{yx}	Damping in the y-direction from a x displacement due to fluid interaction	N·s/m
C_{yy}	Damping in the y-direction from a y displacement due to fluid interaction	N·s/m
d	Distance from the trailing edge of the stator blade to the mid-span of the leading edge of the rotor blades	m
d'	Rotor hub-to-Stator hub distance	m
D	Mean (nominal) gap to seal depth	-
D_h	Hydraulic Diameter (four times the cross sectional area divided by the wetted perimeter)	m
e	Magnitude of eccentricity	m
$\vec{f}$	Six component force vector	N
F_N	Normal force, force acting in the direction of the instantaneous minimum gap	N
F_T	Tangential force, force acting 90° ahead of the instantaneous minimum gap	N

Variable	Description	Units
F_x	Direct force, force acting in the direction of the static minimum gap	N
F_y	Cross force, force acting 90° ahead of the static minimum gap	N
$\overline{F}_S$	Force on rotor due to its position	N
$\overline{F}_D$	Force on rotor due to its velocity	N
F_1	Instantaneous measured force	N
F_2	Instantaneous measured force	N
h	Vertical height of the sealing knives	m
H	Seal depth to seal radius	-
K	Analogous to α where $K \sim \frac{1}{\alpha} - 1$ but K is actually defined as $K = \frac{\kappa \delta_1^*}{\mu_2^*}$	-
K_s	Shaft stiffness	N/m
k_{xx}	Direct stiffness	N/m
k_{xy}	Cross stiffness	N/m
K_{xx}	Stiffness in the x-direction from a x displacement due to fluid interaction	N/m
K_{xy}	Stiffness in the x-direction from a y displacement due to fluid interaction	N/m
K_{yx}	Stiffness in the y-direction from a x displacement due to fluid interaction	N/m
K_{yy}	Stiffness in the y-direction from a y displacement due to fluid interaction	N/m
$\overline{K}_{xx}$	Direct stiffness coefficient	-
$\overline{K}_{xy}$	Cross stiffness coefficient	-
l	Length of the land in the shroud, distance between knife edges (axial length of cavity)	m
l_e	Effective seal pitch (distance fluid must travel from one knife to the next)	m

Variable	Description	Units
L	Seal width to seal radius	-
m	Mass of shrouded rotor disk	kg
$\dot{m}$	Mass flow rate	kg/s
$m1$	DC offset for the pressure sinusoidal curve fit equation	psid
$m2$	Magnitude of the sine component for the pressure sinusoidal curve fit equation	psid
$m3$	Magnitude of the cosine component for the pressure sinusoidal curve fit equation	psid
M_{air}	Molecular weight of air	kg/kmol
M_{freon}	Molecular weight of freon	kg/kmol
M_{xx}	Apparent Mass	kg
M_{yy}	Apparent Mass	kg
p	Variable in Schwarz-Christoffel transformation	-
P_i	Nonuniform stagnation pressure at the inlet to the shroud	Pa
P	Nonuniform static pressure in the cavity of the shroud	Pa
P_o	Nonuniform static pressure at the exit of the shroud	Pa
q_1	Mass flow rate per unit circumferential length into the shroud's cavity	kg/s·m
q_2	Mass flow rate per unit circumferential length out of the shroud's cavity	kg/s·m
r	Amplitude of the whirling motion (radial displacement or eccentricity)	m
r_d	Amplitude of shaft deflection	m
R	Gas constant for freon	J/kg·K
R_m	Mean radius (distance from the center line to the mean rotor blade height)	m
R_s	Radius of the shroud, distance from center line to outer radius of the land (NOT the knife tips)	m
Re_s^*	Reynolds number at the casing	-

Variable	Description	Units
Re_r^*	Reynolds number at the rotor	-
S	Spin rate of seal to swirling fluid velocity in gland	-
T	Temperature before, within and after the shroud	°K
T_Q	Torque measured in experimental facility	N·m
u	Stators trailing edge velocity near the upper wall in the half plane (Schwarz-Christofell transformation)	m/s
$\vec{u}_i$	Velocity at the inlet to the shroud	m/s
U_{es}	Axial velocity at the exit of the stator	m/s
U_{0es}	Axial velocity at the exit of the stator that would exist if there were no blockage by the shroud	m/s
V_i	Nonuniform fluid tangential velocity at the inlet to the shroud	m/s
V	Nonuniform fluid tangential velocity in the cavity of the shroud	m/s
$\vec{V}_v$	Six component voltage vector	volts
w_1	Axial velocity over sealing knife	m/s
W	Whirling spin rate to swirling fluid velocity in gland	-
α	Convergence or divergence of seal	-
α_i	Inlet swirl into the rotor	rad
α_2	Stator exit angle	rad
β	Carry-over factor	-
β_x	Alford force coefficient describing the direct force	-
β_y	Alford force coefficient describing the cross force	-
χ_{air}	Mole fraction of air	-
χ_{freon}	Mole fraction of freon	-
δ	Instantaneous sealing gap	m
δ_1	Sealing clearance between inlet knife and casing	m
δ_2	Sealing clearance between outlet knife and casing	m

Variable	Description	Units
ε	Tolerance to test convergence of V^*	m/s
ε_1	Normalized eccentricity	-
ϕ	Circumferential location of first dynamometer sample	rad
Φ	Empirical relation variable	-
γ	Ratio of specific heats	-
η_i	Velocity perturbation around the circumference of the rotor at the inlet to the shroud	-
η	Velocity perturbation around the circumference of the rotor within the shroud cavity	-
κ	Sensitivity of the carry-over factor to radial displacement	m^{-1}
λ	Eigenvalues of the rotordynamic system of equations	s^{-1}
λ_r	Friction factor at rotor	-
λ_s	Friction factor at stator	-
μ	Fraction of mass flow that escapes over the sealing knives of the shroud	-
μ_1	Flow coefficient at inlet to the shroud	-
μ_2	Flow coefficient at exit of the shroud	-
ν	Kinematic viscosity	m^2/s
θ	Arbitrary circumferential location	rad
ρ_1	Density over the first sealing knife	kg/m^3
ρ	Density within the cavity of the shroud	kg/m^3
ρ_i	Density at the inlet to the shroud	kg/m^3
τ_r	Shear at rotor	N/m^2
τ_s	Shear at casing (wall)	N/m^2
ς	Density perturbation around the circumference of the rotor within the shroud cavity	-
ω	Frequency of rotation of the shaft	1/s

Variable	Description	Units
ω_D	Design frequency of rotation of the shaft	1/s
ω_n	Natural frequency of system	1/s
Ω	Whirling frequency of rotor	1/s
ξ_i	Pressure perturbation around the circumference of the rotor at the inlet to the shroud	-
ξ	Pressure perturbation around the circumference of the rotor within the shroud cavity	-
ξ_o	Pressure perturbation around the circumference of the rotor at the outlet to the shroud	-
ψ_η	Phase angle ahead of minimum gap where maximum value of velocity occurs	rad
ψ_ξ	Phase angle ahead of minimum gap where maximum value of pressure occurs	rad
ζ_1	Flow rate perturbation around the circumference of the rotor at the inlet to the shroud	-
ζ_2	Flow rate perturbation around the circumference of the rotor at the outlet to the shroud	-

Chapter 1

Introduction

1.1 Background & Motivation

The literature contains many cases of severe vibration problems in rotating machinery. One such case is that of the Space Shuttle Main Engine (SSME) High Pressure Fuel Turbopump (HPFTP) and the SSME High Pressure Oxidizer Turbopump (HPOTP) where unexpected severe vibration problems were encountered during initial testing. The severity of the vibration problems was reduced after six months of redesign at an average cost of half a million dollars a day.[4,10] From the point of view of both time and money it is clear that a better understanding of vibration in rotating components and a more comprehensive theory of rotordynamic instability is needed.

The term rotor whirl is used to describe a certain type of vibration inherent in the initial tests of the SSME HPFTP and HPOTP. Generally, whirl is used to describe a satelliting lateral (transverse) deflection of a rotating shaft. This deflection can trace out elliptical orbits and in ideal cases circular orbits. Other deflections are possible, such as longitudinal (axial) and torsional (angular), however, these type of vibrations will not be discussed or investigated in this work. An ideal turbomachine has its centerline matched with the axis of rotation and the result is the absence of whirl for all speeds. In reality turbomachines operate with some amount of whirl since they are less than ideal and operate in less than ideal conditions When rotor whirl continues to grow in amplitude the machine is said to be unstable. The forces that develop which promote rotor whirl are termed destabilizing forces and the reinforcing interaction of the forces with the whirl is called rotordynamic instability.

The problem of severe vibration in the Space Shuttle's Main Engine components should further be discussed in order to build a foundation for the rest of this thesis.[4,10] The HPFTP was designed to run at 37,000 rpm between the second and third critical speeds (critical speeds are discussed in detail in section 1.2.1). During initial tests, as the HPFTP was being spooled up to design speed, a nonsynchronous rotor whirl[1] was noticed at a shaft speed of 19,000 rpm. As the rotational speed was increased accelerometer saturation was noticed at a shaft speed of 22,000 rpm where the vibration amplitude was severe enough to stop testing. In the case of the HPOTP whose design speed is at 30,400 rpm and produces 22,000 kW (29,000 hp), the whirl began to develop at a shaft speed of twice the critical frequency and the whirl itself was at the critical frequency. Therefore, both these turbopumps had vibration problems which, before the design changes, rendered them inoperable. The case study of the SSME HPFTP and HPOTP is meant to place due emphasis on the need to understand destabilizing forces and rotordynamic instability. This thesis concentrates on the experimental measurement of the destabilizing forces and the theoretical model of rotordynamic instability for a shrouded[2] turbine. The use of a shrouded turbine is an attempt to model the turbine in the SSME HPOTP.

Rotational shaft speeds of 30,000 rpm are quite high and it is important to understand why turbomachines need to be designed to withstand such high rotational speeds. The need for a compact size and hence, low weight is essential to aerospace applications. It is known that power is proportional to the square of the dimensions and to the cube of velocity, therefore, a compact size with high power output is obtained by increasing the rotational shaft speed. Section 1.2 explains why high shaft rotational speeds tend to destabilize rotating components.

---

[1]If one is unfamiliar with the meaning of synchronous and nonsynchronous whirl one may read section 1.2.2 at this time.

[2]For those who are unfamiliar with what is meant by a shroud, one may refer to Figure 2.4 and Figure 2.5. The shroud is a band with radial sealing knives which fits over the tips of the rotor blades in order to prevent leakage flows over their tips from the pressure side of the blade to the suction side of the blade.

The next section contains a discussion of critical frequencies and rotor whirl, followed by an explanation of the difference between forced vibration and self-excited vibration. The chapter concludes with a formulation of a model to aid in a discussion of rotordynamic instability. The following chapters present the experimental facility where the shrouded turbine resides and where the destabilizing forces are measured. The results of those experiments are presented and explained. Following the experimental investigation, a theoretical model of the shroud turbine is developed. This theoretical model attempts to explain how the fluid dynamics and geometry interact within the shroud to produce instability. This thesis ends with a comparison of the experimental data to the results obtained from the theoretical model.

1.2 Terminology of Rotordynamic Instability

Before a model is developed, certain terms related to rotordynamic instabilities are reviewed. In this section, critical frequencies are reviewed, rotor whirl is defined and the difference between forced and self-excited vibrations is explained.

1.2.1 Critical Frequencies

An unbalanced rotating disk shown in Figure 1.1 is used to illustrate and explain critical frequencies.[5,10] In this simplified case gravity is neglected and the shaft is taken to be massless. First, this disk is said to have the center of gravity located a distance, e, from the center of the shaft. This eccentricity is represented by the distance between points S (shaft center) and G (gravity center) in the A-A cross section view in Figure 1.1. The eccentric center of gravity creates a rotating centrifugal force equal to $m\omega^2 e$ where m is the mass of the disk and ω is the constant frequency. This rotating unbalance deflects the shaft and the shaft deflection is the distance r_d between points B (bearing center) and S in Figure 1.1 A-A cross section view. This deflection adds to the centrifugal force and the total centrifugal force is $m\omega^2(r_d + e)$.

Shaft deflection is dependent on the bending stiffness of the shaft. Due to bending, a restoring force is present which acts in the direction opposite to the centrifugal force. If the bending stiffness of the shaft is given by K_s and the deflection is r_d, then the restoring force is given by $K_s r_d$. Equating these forces one obtains equation (1.1).

$$K_s r_d = m\omega^2 (r_d + e) \tag{1.1}$$

An unbalance, such as the eccentric center of gravity, creates a vibration in the plane of the disk and the amplitude of the vibration depends on the angular speed (rotational shaft speed) of the disk. These vibrations are largest at the natural frequency of the system, that is, where the angular frequency, ω, equals the natural frequency, ω_n. Operation of a rotating system at its natural frequency can lead to large vibrations and possible destruction of the shaft and its components.

The angular speed at which $\omega = \omega_n$ is termed the critical speed. Mathematically the critical speed is found in terms of the bending stiffness of the shaft and its mass. This is done by first solving equation (1.1) for the shaft deflection.

$$r_d = \frac{m\omega^2 e}{K_s - m\omega^2} \tag{1.2}$$

It can be seen from equation (1.2) that the deflection is infinite when $K_s = m\omega^2$, therefore, the critical frequency is given by equation (1.3).

$$\omega_n = \omega_c = \sqrt{\frac{K_s}{m}} \tag{1.3}$$

In order to gain insight into the relationship between the shaft angular frequency and its critical speed, equation (1. 2) is rearranged and equation (1.3) is substituted into that new equation and equation (1.4) results:

$$r_d = e\frac{\left(\frac{\omega}{\omega_n}\right)^2}{1-\left(\frac{\omega}{\omega_n}\right)^2} \tag{1.4}$$

It is seen in equation (1.4) that if a shaft increases its angular speed from below the critical speed to above the critical speed the deflection changes sign and decreases in magnitude. To explain this more precisely one is referred once again to Figure 1.1 where the cross section of the unbalanced rotating disk is shown and the deflection magnitude versus the angular frequency is illustrated. For an angular frequency below the critical frequency, the gravity center, G, is the furthest point from the bearing center. As the angular speed is increased above the critical speed the gravity center, G, reverses its relative position. This causes the gravity center, G, and the bearing center, B, to converge and for the vibration magnitude to decrease as is illustrated by the deflection vs. frequency graph. For very slow rotations r_d = BS is practically zero, for rotation at the critical speed r_d = BS is infinite and for very fast rotational speeds the center of gravity, G, is at the bearing center (r_d = BS = e). Notice that for this final case the maximum amplitude of vibration is the eccentricity of the center of gravity. It is observed that at very large rotational speeds the center of gravity does not move, for if it did move the inertia force would become very large.

The model that is presented above is an extremely simplified model of a rotating system. It is meant to illustrate how a shaft responds to an unbalance and in particular at what angular speeds will the worst vibrations be expected. In a "real" system other factors exist such as the fact that the shaft is not limited to vibrations in the plane of the rotating mass and the shaft may contain more than one mass with any number of supports. The shaft and bearings interact, and the rotating components can be operating in various fluids with a wide range of viscous properties. These interactions can

provide damping which may be positive or negative.[3] The components of the system may also be subject to both steady and unsteady loads.

As one can see the problem of determining the systems properties becomes quite complex and impossible to solve when one takes into account all the variables. Estimates of the actual critical speeds are used, however, it must be emphasized that such a complex system has an infinite number of critical speeds. Most engineers and researchers only concern themselves with estimating the first two or three critical speeds. These estimates are usually obtained by creating a model of the system which only accounts for some of the variables, therefore, the system begins to resemble the simplified model presented above. The better the model, the more accurate the estimates and the more difficult the model is to solve.

The first couple of critical frequencies are very important to estimate since the operating point of a machine will tend to lie between these critical frequencies and, thus, will have to be brought through those potentially damaging speeds. When components are designed they must provide enough damping such that the machine is able to operate with very small levels of whirl at its designated speeds. Also, enough damping must be provided such that the machine is able to operate below or be brought through any of the critical speeds without having a destructive outcome. The severe amplitudes associated with operation at the critical speeds does not occur at once, it takes some time to build. Therefore, a machine is usually able to be brought through the critical speeds without any damage whatsoever.

1.2.2 Whirl

Some amount of whirl is always present in rotating machinery.[10] It is when the whirl becomes excessive and is able to violate the clearances within the machinery

[3]Dry friction and oil whip are two causes of self-excited vibrations which can occur in rotating machinery and may be thought of as having negative damping. Self-excited vibration will be explained in section 1.2.3.

that this is of major concern. The simplified example presented in the previous section is a little narrow or misleading when thinking about what types of whirl can occur. The example given concentrates on a forced vibration to place emphasis on critical frequencies, however, such an example is insufficient when one wishes to explain the types of whirl which occur in rotating machinery. In pure simplified forced vibration (as shown in the previous section) the whirl is synchronous. A synchronous whirl means that the frequency or whirl, Ω, is equal to the frequency of rotation, ω ($\Omega = \omega$).

Two other classes of whirl are also possible and they are termed subsynchronous, when $\Omega < \omega$, and supersynchronous, when $\Omega > \omega$. The whirling motion is either in the forward or backward direction. It is possible for several different whirls to be present at the same time. As mentioned in section 1.1, the SSME turbopumps suffered from subsynchronous whirl which was locked to the natural frequency of the system. In order to understand how this type of whirl is possible self-excited vibrations are discussed. Sections 1.2.3 and 1.3 expand on these ideas.

1.2.3 Forced vs. Self Excited Vibration

The definitions of the two types of vibrations will be reviewed and then it will be shown that self-excited vibration is pertinent to the matter at hand. Both forced and self excited vibrations can cause rotordynamic instability.

It is explained in section 1.2.1 that forced vibration in rotating machinery occurs due to some type of unbalance and the resulting whirl is always synchronous. However, an unbalance is not the only means of producing a forced vibration. A forced vibration may also be caused by a force which occurs once per turn, like a rub, or a concentrated aerodynamic force fixed to the casing. The amplitude of this type of whirl is largest at the critical frequencies of the system and "the sustaining alternating force exists independently of the motion and persists even when the vibratory motion is stopped" [5]. Forced whirl is always in the forward direction.

Self-excited vibration is sustained through the extraction of energy from some outside source due to the whirl. It is important to understand this concept which is reiterated in the following way: "the alternating force that sustains the motion is created or controlled by the motion itself; when the motion stops the alternating force disappears."[5] The flutter of an aircraft wing is a perfect example of self-excited vibration. Flutter is not noticed until a certain velocity is achieved. As the fluid velocity with respect to the wing is increased the flutter amplitude grows. It is not until the motion of the fluid is stopped or goes below a certain velocity that the vibration stops. Another way of looking at self excited vibration is in the case that is of importance in this thesis, namely the fluid effects contributing to the whirl of a shrouded turbine rotor. The whirling motion is extracting energy from the passing fluid in such a way as to increase the rotor's whirl amplitude. Remember that in the case study of the SSME HPOTP the whirl began to develop at a shaft speed of twice the critical frequency and the whirl itself was at the critical frequency. This is a perfect example of self-excited vibration and subsynchronous whirl.

Whirling at the critical frequency of the system is expected in the case of a self-excited system. Self-excited vibration has no forcing function and is simply represented by a homogeneous equation. It is known that in a one-dimensional free vibration with zero damping the frequency of vibration is the natural frequency of the system. Taking this one step further, when one adds damping (positive or negative) to the one-degree of freedom system, the damping force lowers the natural frequency, but not by much.[4] In most practical cases the difference between the natural frequency of a damped system and that of an undamped system is negligible. This statement leads one to support the claim that self-excited vibration is considered to occur at the (undamped) critical frequency of the system [5].

---

[4]In the 2-dimensional case it is the cross damping and direct stiffness which affect the frequency. This will be shown in section 1.3.

Mathematically, self-excited vibration has no forcing function and in a one dimensional vibration it is viewed as a free vibration with negative damping. The negative damping is destabilizing. When a two dimensional vibration is considered the destabilizing mechanisms are more complex and generally involve negative direct damping and positive cross stiffness.[5]

Self-excited vibration may not occur until a certain rotational speed is reached. This speed is termed OSI (Onset Speed of Instability). Above OSI, the instability mechanism is first noticed. However, different types of self-excited vibrations have different "onset" mechanisms, and some have none. For the case of the shrouded turbine the shroud-driven and aerodynamic instabilities are present at all speeds, therefore, there is no OSI (or OSI is at a speed of zero). The instability present in the shrouded turbine increases with shaft power and at some power level it is able to overcome machine damping at which point the machine is in danger of destruction.

In order to compare and summarize these two type of vibration problems in a single frame one is now referred to Figure 1.2. The vertical axis is the vibration amplitude while the horizontal axis shows the rotational speed. In the discussion above, the amplitude of forced vibration reaches its maximum at the critical frequency, where rotational speed (ω) is equal to the critical frequency (ω_n). As the shafts rotational speed is increased above the critical frequency the vibration amplitude decreases. The effects of self-excited vibration are always present in the shrouded turbine, however, do not become severe until high power levels are reached. Figure 1.2 shows that the amplitude of vibration due to the self-excited force grows as the shaft rotational speed is increased. This is the reason why during initial tests of the HPFTP the effects of the self-excited vibration where not noticed until high rotational speeds of 19,000 rpm were reached. One should now understand the importance of distinguishing between the two types of vibrations. It should also be clear why the need

[5]The 2-dimensional case of instability will further be discussed in section 1.3.

to understand self-excited vibration is pertinent when investigating vibration problems such as those that were present in the initial tests of the SSME HPOTP and the SSME HPFTP.

1.3 Rotordynamic Instability Model

A two degree-of-freedom model is developed to explain the lateral motion of a rotating disk immersed in a fluid. This is a simplified model which attempts to explain the lateral destabilizing motions which are observed in turbomachines.[6] Of course, as in all simplified models not all the variables are taken into account, however, the pertinent information is included and stability criteria are extracted.

Figure 1.3 illustrates the model used. The shaft is massless and has a stiffness of K_S. One end of the shaft is fixed while the other is free to move in the vertical direction. It is assumed that all the mass is concentrated within a thin disk of mass m and that this disk is limited in it's movement to the X-Y plane. There is a force due to the disk's position and is given by equation (1.5).

$$\vec{F}_S = -\begin{bmatrix} K_s + K_{xx} & K_{xy} \\ K_{yx} & K_s + K_{yy} \end{bmatrix} \begin{bmatrix} x \\ y \end{bmatrix} \tag{1.5}$$

The stiffness variables K_{xx}, K_{xy}, K_{yx}, and K_{yy} arise from the fluid interaction with the rotating mass. Both K_{xx} and K_{yy} are termed the direct stiffness because they relate a displacement in one direction to a force in that same direction. The other two stiffnesses, K_{xy} and K_{yx}, are called cross stiffnesses because they relate a displacement in one direction to a force perpendicular to that direction. The presence of these cross stiffness terms affect the model's stability. In the physical sense one can predict why these cross stiffness can be destabilizing. Since K_{xy} and K_{yx} relate a displacement to a force perpendicular to that displacement this tangential force will tend to promote whirl

[6]In particular we wish to model the SSME HPOTP. This will be further discussed in the Experimental sections located in Chapters 2 and 3.

and destabilize the rotating components if the tangential force and the whirl are in the same direction. If the whirl is in the opposite direction to the tangential force, the cross stiffness terms tend to stabilize the whirl.

Since the thin disk is free to whirl it also has velocity in the X-Y plane, therefore, the fluid has damping effects on the rotating components and the force due to the disk's velocity is given by equation (1.6).

$$\vec{F}_D = -\begin{bmatrix} C_{xx} & C_{xy} \\ C_{yx} & C_{yy} \end{bmatrix} \begin{bmatrix} \dot{x} \\ \dot{y} \end{bmatrix} \tag{1.6}$$

The direct damping terms (C_{xx} and C_{yy}) relate the disk's velocity in one direction to a force in that same direction, while the cross damping terms (C_{xy} and C_{yx}) relate the disk's velocity in one direction to a forces perpendicular to that velocity. The terms which are important for stability analysis are discussed once the solution is derived.

The same type of argument as presented for the derivation of the forces due to stiffness and damping can be applied to inertial effects and higher order terms, however, for simplicity only the direct added mass inertial terms are used. Applying Newton's Second Law to the stiffness, damping, and inertial forces, one obtains the following system of differential equations.

$$\begin{bmatrix} m+M_{xx} & 0 \\ 0 & m+M_{yy} \end{bmatrix} \begin{bmatrix} \ddot{x} \\ \ddot{y} \end{bmatrix} + \begin{bmatrix} C_{xx} & C_{xy} \\ C_{yx} & C_{yy} \end{bmatrix} \begin{bmatrix} \dot{x} \\ \dot{y} \end{bmatrix} + \begin{bmatrix} K_s+K_{xx} & K_{xy} \\ K_{yx} & K_s+K_{yy} \end{bmatrix} \begin{bmatrix} x \\ y \end{bmatrix} = \vec{0} \tag{1.7}$$

Equation (1.7) is a homogeneous equation. The solution to this equation brings insight into the stability of the model and reinforces the predictions of stability presented above.

In order to solve equation (1.7), first the circular symmetry of the problem is taken into account, from which one obtains the following simplifications: $[\ ]_{xx} = [\ ]_{yy}$ and $[\ ]_{xy} = -[\ ]_{yx}$. Next, one assumes a complex displacement vector for the solution. This complex displacement vector is given by equation (1.9).[15]

$$z = x + iy = \hat{z}e^{\lambda t} \tag{1.9}$$

If $|K_{ij}| << K_s$ and $\Omega|C_{ij}| << K_s$ the frequency and amplitude of the displacement vector will be given by λ in equation (1.10). The amplitude is the real part of the eigenvalue while the frequency is the imaginary part of the eigenvalue.

$$\lambda = \mp\frac{K_{xy}}{2\sqrt{K_s(m+M_{xx})}} - \frac{C_{xx}}{2(m+M_{xx})} + i\left(\pm\sqrt{\frac{K_s}{m+M_{xx}}} \pm \frac{K_{xx}}{2\sqrt{K_s(m+M_{xx})}} + \frac{C_{xy}}{2(m+M_{xx})}\right) \tag{1.10}$$

There are a few things to notice about equation (1.10). First, if the second and third terms of the imaginary part of equation (1.10) are small compared to the first term, then the whirl occurs at nearly the natural frequency of the system. This is discussed above[7]. Next, notice that one of the roots might be unstable due to the $\pm\frac{K_{xy}}{2\sqrt{K_s(m+M_{xx})}}$ term.

If this cross stiffness-induced term interacts with the direct damping-induced term, $-\frac{C_{xx}}{2(m+M_{xx})}$, resulting in a positive eigenvalue, the system is unstable. Once again, the instability that might arise due to cross stiffness is anticipated, since cross stiffness creates a cross force which when it acts in the direction of the whirl it tends to destabilize the rotating disk. Lastly, it is the direct damping term, C_{xx}, not the cross damping term, C_{xy}, which affects the stability of the system. It is only the frequency of the system that is slightly changed due to cross damping.

1.4 The Destabilizing Forces

[7]Remember that the whirl in the SSME HPOTP and HPFTP occurred at first critical frequency (natural frequency) of the system. Also, remember that it was stated previously that whirl due to self-excited vibrations usually occurs at the critical frequency of the system. (See sections 1.2.1-1.2.3)

In section 1.3 the rotordynamic stability model is derived by assuming forces due to the shaft's stiffness, the fluid's stiffness and the fluid's damping. These forces act on the disk because of the eccentricity of the system. From these components, stability criteria are derived. However, a physical reason why these forces exist has not been given. In this section a brief explanation of the physical mechanisms that give rise to these forces is explained and, thus, aids in the understanding of the reasons for certain measurements undertaken in the experimental facility (chapter 2).

1.4.1 Nonuniformity in Circumferential Pressure

In its concentric position the pressure distribution around the circumference of the shrouded rotor is uniform, both within the seal and upstream and downstream of the rotor. As the rotor is moved eccentric this azimuthal uniform pressure distribution is replace by a nonuniform distribution of pressure. As is shown by experiment, this nonuniformity is present within the shroud, upstream of the rotor and downstream of the rotor. It is the nonuniformity in pressure within the cavity of the shroud (between the knives of the shroud) that gives rise to a net force placed on the rotor. This force is calculated via equations (1.11) and (1.12).

$$F_N = -R_s \int_0^{2\pi} \int_0^l P(\theta,x,t) Cos\theta dx d\theta \tag{1.11}$$

$$F_T = -R_s \int_0^{2\pi} \int_0^l P(\theta,x,t) Sin\theta dx d\theta \tag{1.12}$$

where F_N is the normal force or the force in the direction of displacement, F_T is the tangential force of the force perpendicular to the direction of displacement, $P(\theta,x,t)$ is the pressure distribution, l is the length of the land (distance between the shroud's knife edges) and R_s is the radius of the seal. Figure 1.4 illustrates the shrouded rotor eccentrically positioned within the casing along with the resulting forces due to the nonuniform pressure distribution. The pressure distribution in the axial direction is

uniform between the sealing knives, therefore, equation (1.11) and (1.12) may be simplified to:

$$F_N = -R_s l \int_0^{2\pi} P(\theta,t) Cos\theta d\theta \tag{1.13}$$

$$F_T = -R_s l \int_0^{2\pi} P(\theta,t) Sin\theta d\theta \tag{1.14}$$

Throughout this work the normal force is sometimes be referred to as the direct force, F_x, and the tangential force is sometimes be referred to as the cross force, F_y. The direct and cross forces are a special case of the normal and tangential forces. The direct and cross force terminology is used in this experimental work since the turbine is statically displaced (whirl is zero).[8] A statically displaced turbine allows one to map the forces directly to an inertial frame (lab reference frame), therefore, the forces are no longer function of whirl and time. Because of this, equations (1.13) and (1.14) are further simplified to:

$$F_x = F_N = -R_s l \int_0^{2\pi} P(\theta) Cos\theta d\theta \tag{1.15}$$

$$F_y = F_T = -R_s l \int_0^{2\pi} P(\theta) Sin\theta d\theta \tag{1.16}$$

As can be seen by the above equations, if the pressure nonuniformity within the cavity of the shroud is known the direct and cross forces can be computed. The experiments explained in chapter 2 measure this pressure distribution within this cavity.

In chapter 4, the theoretical approach to determining this nonuniform pressure is shown. However, in order to calculate this asymmetric pressure distribution within the shroud, using a theoretical approach, the magnitude and phase of the nonuniform pressure upstream and downstream of the shrouded rotor must be known. For a simple seal-land geometry, with no turbine blades, this pressure can be calculated theoretically.

[8]The statically displaced turbine experiments will further be explained in chapter 2 (Experimental Facility).

[17] However, no simple theory exists for a shroud in the presence of the eccentric turbine. Experiments are used to determine these upstream and downstream pressure nonuniformities. The theory is then used incorporating these measured values. The result of the theoretical calculation gives the pressure distribution, $P(\theta,t)$, within the land of the shroud. Equations (1.13) and (1.14) are then used to find the normal and tangential forces. If the theory is run with the shrouded rotor statically displaced then equations (1.15) and (1.16) are used to find the direct and cross forces.

1.4.2 The Alford Effect

The azimuthal nonuniformity in pressure is one of two contributions to the existence of normal (direct) and tangential (cross) forces. The second contribution is due to the Alford effect.[1]

A turbomachine which is operating in an eccentric position has a variation in blade tip clearances around the circumference of the rotor. Alford theorized that when a turbomachine is operating in this state the blades which are closer to the casing are operating locally more efficiently than those blades which have a larger tip clearance. Since, the blade forces vary approximately with the efficiency those blades which are closer to the casing have a heavier loading than those which are further from the casing. This variation in blade forces, when integrated around the circumference of the rotor yields a net force which acts both in the direction of the rotors displacement (normal force) and tangential to that displacement (tangential force). Figure 1.5 illustrates this concept in schematic form. As is seen in the figure a large blade force exists and when this force acts in the direction of rotor whirl the system is unstable.

Note that Figure 1.5 illustrates this effect with an unshrouded turbine, however, this effect is also present in a shrouded turbine. The Alford force arises whenever there is blade tip leakage, however, this leakage is reduced in the shrouded turbine because of the shroud. Therefore, the reduction of blade tip leakage causes the shrouded turbine to

exhibit a smaller Alford effect than that which exists in an unshrouded turbine. Also, the Alford force in a shrouded turbine is small compared to the forces developed from the pressure nonuniformity, however, this Alford effect is still not negligible.

One result of Alford's efforts is a widely used nondimensional variable which describes the magnitude of the normal (direct) and tangential (cross) forces developed due to eccentric rotation. Since our experimental turbine is prevented from whirling these forces will be referred to as direct and cross forces. The forces are the summation of the two effects, the pressure effect and the Alford effect. This Alford factor nondimensionalizes these force by the torque developed, T_Q,the mean radius of the rotor, R_m, the blade height, B_H, and the eccentricity, e. This is shown by equations (1.17) and (1.18).

$$\beta_x = \frac{2\left(\frac{F_x}{e}\right)R_m B_H}{T_Q} \tag{1.17}$$

$$\beta_y = \frac{2\left(\frac{F_y}{e}\right)R_m B_H}{T_Q} \tag{1.18}$$

Chapter 3 incorporates these nondimensional variables when presenting the experimental results. The bracketed terms in the above equations, $\frac{F_x}{e}$ and $\frac{F_y}{e}$, are simply the slopes of the linear curve fits through the data point on a plot of direct & cross force vs. eccentricity.

Once again, the total direct and total cross force are the summations of the forces contributed by both the pressure effect and the Alford effect.

1.5 Objective

The primary objective of this work is to measure the direct and cross forces on a shrouded turbine (Chapter 2 and 3). These forces are determined by a direct

measurement via a rotating dynamometer. They are also determined by a second method which requires the measurement of the pressure distribution around the circumference of the rotor (pressure effect) and the measurement of the velocities circumferential around the exit of the rotor (Alford effect). Through these measurements the direct and cross forces are determined.

The final objective is to expand upon a theoretical model (Chapters 4 and 5). This model is an extension of the work of several authors [12, 9, 16,17], most recently Millsaps [16,17]. The contribution presented in this work consists of the incorporation of nonzero upstream and downstream nonuniformities, and of their effect on the pressure within the cavity of the shroud. The results of these calculations are compared to those measured experimentally. The development of a good theoretical model is essential. From a good working model designers of these turbomachines gain knowledge of the proper geometry and operating conditions such to minimize pressure nonuniformities in order to minimize the resulting destabilizing forces .

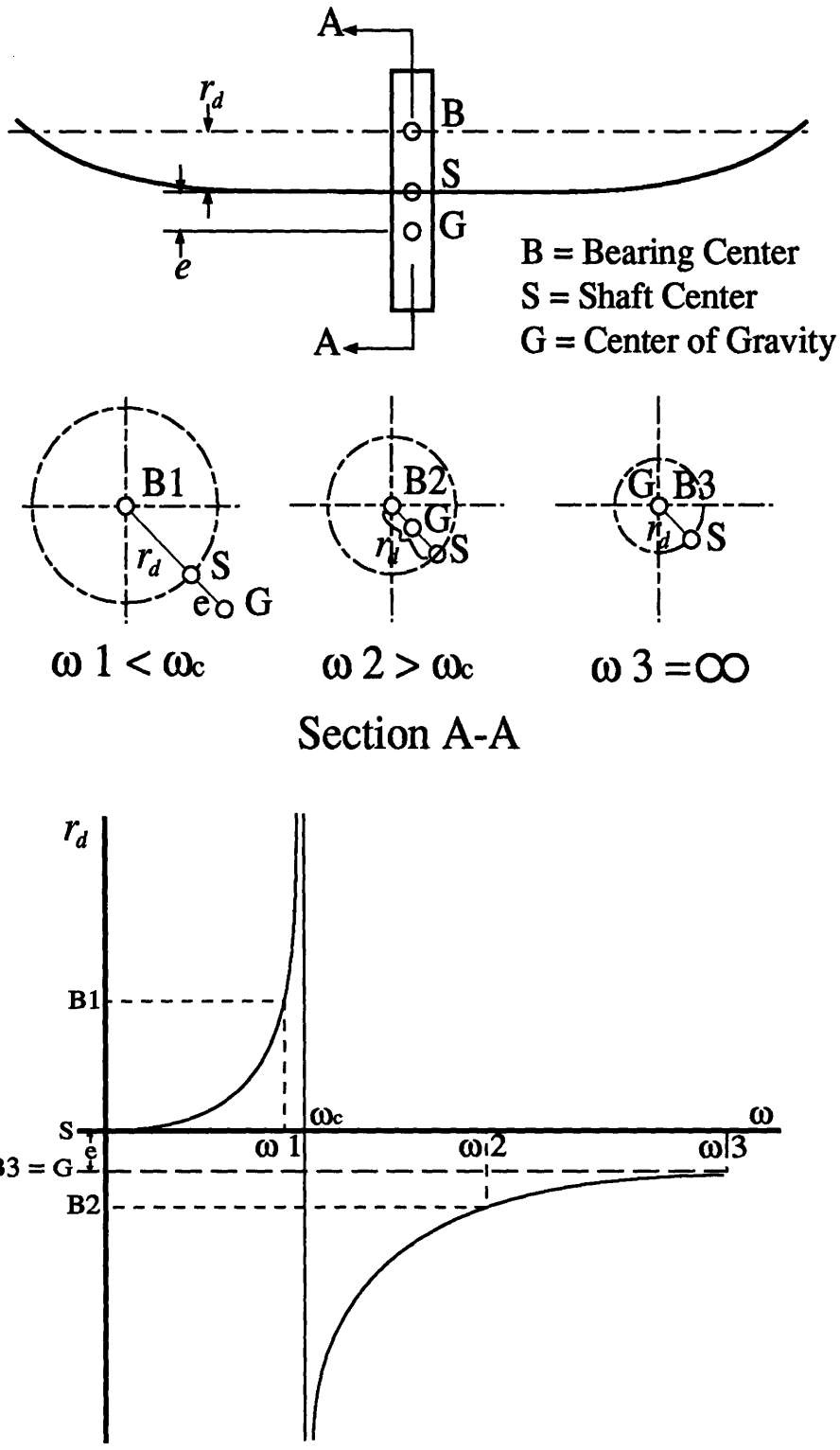

Deflection vs. Frequency of Rotation Illustrating the Relative Locations of S, G and B for the Above Examples

Figure 1.1: Representation of rotor whirl due to a mass unbalance of a weightless vertical shaft without damping.[5,10]

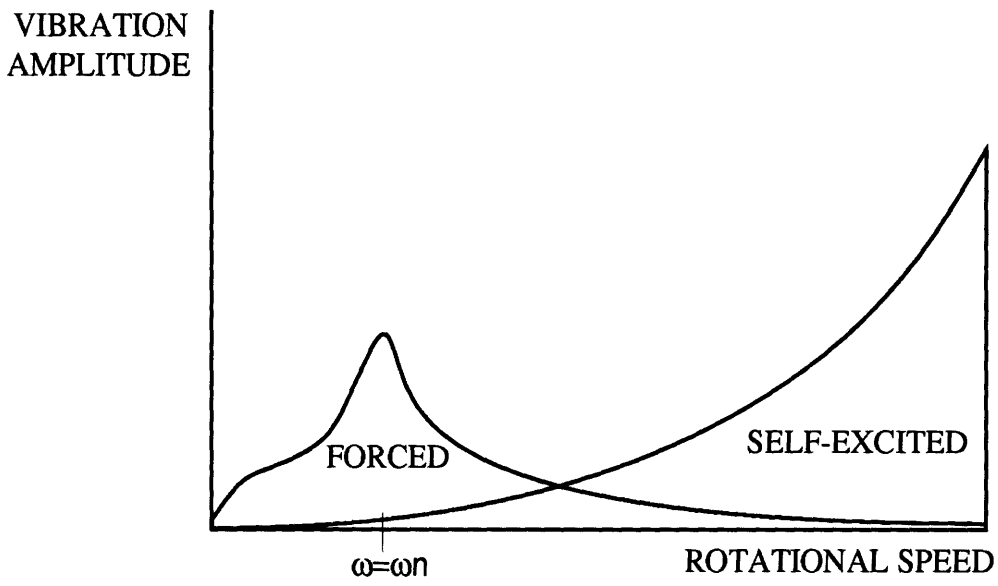

Figure 1.2: Graph of Vibration Amplitude vs. Rotational Speed Illustrating the Differences Between Forced and Self-Excited Vibrations.

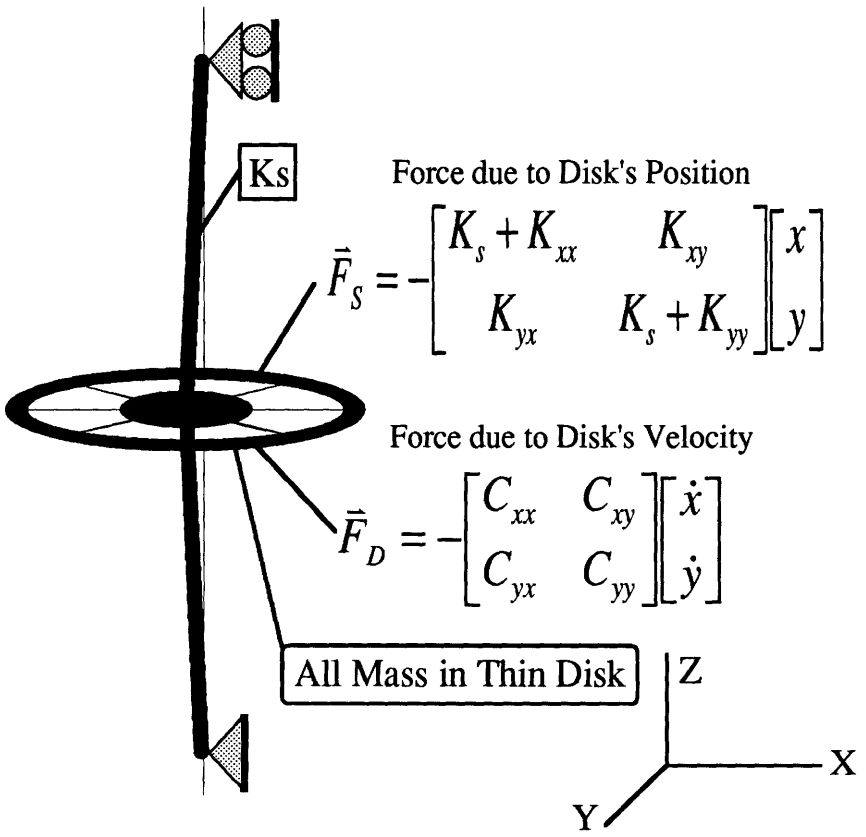

Figure 1.3: Two Degree-of-Freedom Model Used to Derive the Equations to Explain the Lateral Motion of a Rotating Disk Immersed in a Fluid.

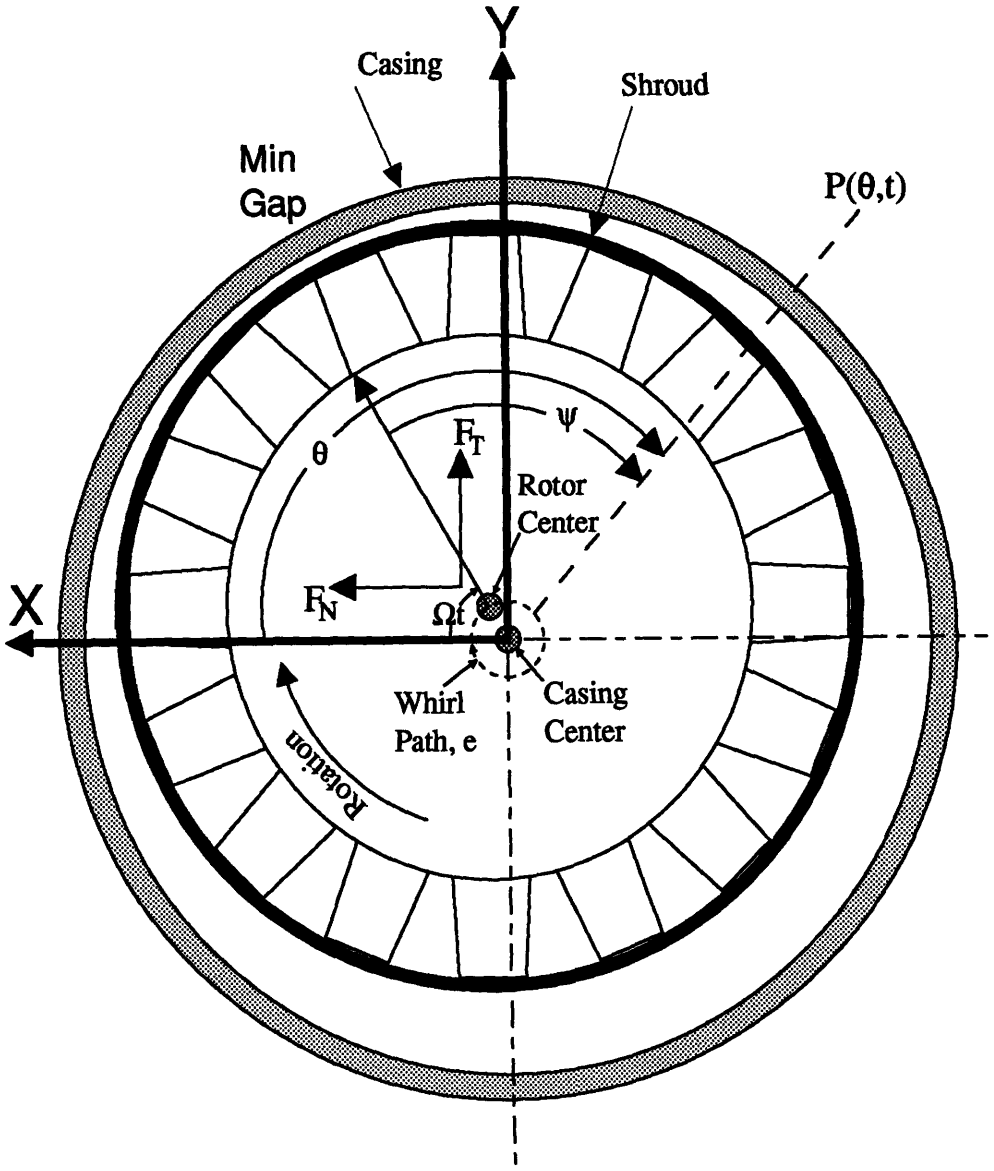

Figure 1.4: Pressure Effect Coordinate System and the Pressure Nonuniformity.

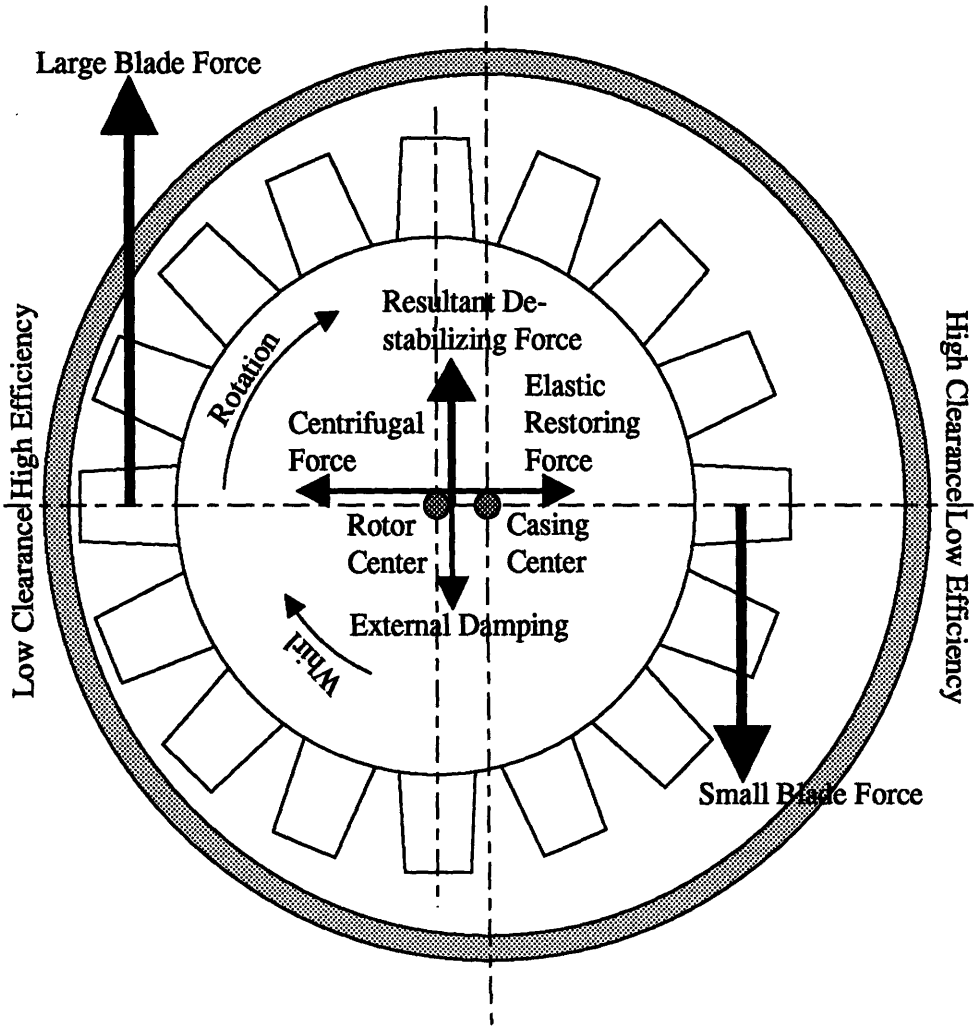

Figure 1.5: Alford Force Destabilizing Mechanism.[8]

Chapter 2

Experimental Facility

2.1 Preliminaries

An experimental facility was designed by Jery, Qiu, Martinez-Sanchez and Greitzer to study destabilizing forces and the associated flow conditions for concentric and statically offset eccentric turbine rotors.[11] Loose constructed the facility and performed initial tests on an unshrouded turbine.[13] Song continued tests on the unshrouded turbine for various geometric configurations.[15] The final investigation into destabilizing forces undertaken within this facility are the static tests performed with a shrouded turbine. This thesis concentrates on the experimentation performed using the shrouded turbine. The experimental facility is reviewed, the modification made to the turbine's rotor is explained and the series of tests performed are outlined within this chapter.

At this point it is important to understand that only static experimentation can be undertaken in this facility. This means that the turbine's rotor can only be offset statically. Therefore, the stiffness terms are the only terms that are found. Higher order terms involving velocities, accelerations, etc. can only be measured if the shaft were set free to whirl in a controlled environment. This type of facility exists, however, it was designed to measure rotordynamic instabilities in seals (shrouds) alone. [17] Millsaps found that fluid damping (direct damping terms: C_{xx} and C_{yy}) is always positive, therefore, it is the magnitude of the cross stiffness terms compared to the direct damping terms which will determine the systems stability (refer to equation (1.10)). As mentioned above, the stiffness is what is found using this experimental facility.

The pressure effect and the Alford effect both create destabilizing forces. This experimental facility is designed to measure that total destabilizing force, the force only due to the pressure effect and the force only due to the Alford effect. The experimental and theoretical work done on the rotordynamic instability of seals by Millsaps and the experimental work of Loose and Song involving destabilizing forces in an unshrouded turbine are both very important foundations for this thesis. The experimental work explained here involves both a seal of similar geometry to that used in Millsaps experiments and a modified version of the turbine used in the unshrouded experiments performed by Loose and Song. This work will show how the direct and cross forces are measured experimentally and, in later chapters, calculated theoretically.

2.2 The Layout of the Experimental Facility

The experimental facility is a closed loop facility where air or Freon 12 may be used as the working fluid. All the tests carried out within this work are done with freon as the working fluid. It will become clear why freon was chosen in section 2.2.1 Turbine Test Section.

First, however, an overview of the facility is presented and please note that one may refer to the following references if additional information is needed: [11,13,14,15]. Figures 2.1 and 2.2 [13] show the front view of the facility and the side view of the facility respectively. Upon viewing Figure 2.1 one notices that the fluid travels around the loop in a counterclockwise direction. A 100 hp electric motor and compressor assembly (located at 2 in Figure 2.1 or at 1 and 2 respectively in Figure 2.2) provide the energy to the fluid and a heat exchanger (located at 3 in Figures 2.1 & 2.2) removes any excess heat added to the fluid by the compressor. Within the loop one will find flow straighteners, and a Venturi meter whose locations may be seen in the figures. The test section which contains the stator and rotor along with a battery of testing instruments is

located at 1 in Figure 2.1 and at 6 in Figure 2.2. Its associated exhaust plenum is located just below within the test stand.

The fluid transmits energy to the rotor and this energy must be damped in order to control the rotational speed. Also, for calibration purposes the rotor needs to be rotated without the use of a fluid. The damping is provided by a DC generator-resistor network and for calibration purposes the rotor is powered by a DC motor. The DC motor and the DC generator are combined within one unit which is located at 14 in Figure 2.2. The excitation field of this motor/generator can be varied to control the turbine speed. Along with the control of the rotational speed, the mass flow rate of the loop must be controlled. This is done with the use of the throttle valve located at 7 in Figure 2.1 and also with the use of a bypass loop and its associated servo driven valve located at 4 and 5 respectively in Figure 2.1.

The above information is of a general nature and should provide one with enough background on how the loop is organized and on the main areas where control is needed. The following subsections go into greater detail about what is discussed above. In particular, section 2.2.1 describes the stator-rotor assembly, the modifications made for shrouded turbine tests and the actual test conditions that are used to provide a realistic test environment.

2.2.1 Turbine Test Section

It is important to understand that the primary objective of this facility is to measure the direct and cross forces that act on the rotor when the rotor is offset from its concentric rotation. The test turbine developed for this facility and used in the unshrouded turbine tests is a 1:1 replica of the SSME HPFTP (first stage only). For the work presented here, this turbine's rotor is modified to incorporate a sealing shroud. The discussion begins with an explanation of the stator-rotor stage and the

modifications made to that stage for shrouded tests. This section concludes with the incorporation of that stage within the test section area.

Figure 2.3 shows a machine drawing of the unshrouded turbine's test rotor. Since, this rotor is a 1:1 replica of the SSME HPFTP's rotor the geometric ratios and flow angles are preserved, therefore, the flow and work coefficients are the same as in the SSME HPFTP's rotor. Both the test turbine and the actual SSME HPFTP turbine have low Mach numbers (M<0.5). Freon is used as the working fluid in order to achieve realistic Reynolds numbers within the testing environment. The SSME HPFTP operates in the turbulent region at a Reynolds number of 5.6×10^6. Therefore, it is important to be in the turbulent region when performing these test because operation below the turbulent regime would introduce difficulties in predicting how factors such as blade aspect ratio and solidity affect performance.[13] Using Freon in the test facility produces a Reynolds number of 9×10^5 which is above the laminar-turbulent transition region. Basically, the use of Freon allows testing to be performed within a reasonably sized closed loop facility where flow conditions are realistically matched to existing aerospace applications.

For the tests presented in this work the unshrouded turbine shown in Figure 2.3 is modified with a full shroud band fitted with two sealing bands. In the interest of brevity the entire shroud band-sealing band combination is simply referred to as a shroud in this thesis. The entire shroud is shown in Figure 2.4 and a cross section view is shown in figure 2.5. The band is designed with a 2/1000 inch (2 mils) interference and is shrunk-fit over the blades. The blades were previously cut and ground to the required height (reduced by 30%) in order to accommodate the shroud. Note that the shroud length is such as to cover exactly the blade tip axial chord. The tensile stress developed in the shroud due to the shrink-fit is 2×10^{11} N/m^2, well within the strength of stainless steel. It is also verified by calculation that the additional bending stress due to the slight straightening tendency of the band between blades is negligibly small.

This is because of the large number of blades, which makes the bowing between blades very slight. Centrifugal effects can at most add the equivalent of 0.5/1000 inch (0.5 mil) to the band radius. Therefore, even if centrifugal growth of the rest of the disk is ignored, the fit should remain tight, which it did. No significant differential thermal effects are expected.

The sealing band angles and tip thicknesses are similar to those used by Millsaps in his seals rig.[17] The ratio $\frac{l Tan6^\circ}{\delta}$ is approximately 2.0, where l is the distance between knife edges and δ is the nominal gap. This ratio is important because it provides information on how much fluid escapes directly over the second sealing knife due to the jet created by the first sealing knife. If the ratio is to small, then most of the fluid entering the seal escapes via the jet created by the first sealing knife and there is no sealing effect.

The stator and shrouded rotor are located within the test section at locations 13 and 9 respectively as shown in Figure 2.6.[15] Further upstream, however, the flow first enters the test section area where it encounters the honeycomb flow straightener and wire screen (1 & 2 respectively in Figure 2.6). The dome of the stator assembly and the stator blades are next as the flow travels vertically downward through the test section. At 0.295 inches after the trailing edge of the stator the flow begins travel through the shrouded rotor. Since the casing is left smooth and hence the shroud is not recessed, the turbine is not as efficient[1] as when the rotor was unshrouded[2]. On the other hand, this configuration is very similar to the configuration presented in Millsaps work which allows for cross comparisons. [17]. The outer casing, identified by the number 12 in figure 2.6, is highly instrumented with velocity probes, static pressure taps and thermocouple gages. This casing has the ability to rotate such that the

[1]The operating point (mass flow rate & rotational speed for largest efficiency) is shown below.
[2]See the work of Loose and Song, references [13] & [15] respectively.

instrumentation may be used throughout the circumference of the test section. Further discussion of the instrument locations is discussed below.

Upon leaving the rotor the flow travels through the remaining part of the upper test section. The rotating dynamometer (location shown by 14 in Figure 2.6) is located in this area within the shaft assembly. The forces acting upon the rotor are directly measured by this rotating dynamometer and this device is explained in greater detail below.

The flow enters the lower part of the test section next. This area contains the means to offset the rotor from its concentric position. Turbine-offsetting rods, identified by the number 16 in Figure 2.6, are used to displace the rotor statically in a linear direction either to the left or the right. This displacement is considered the X-direction within this report and the forces in this direction are called direct or normal forces. The Y-direction is perpendicular into and out of the plane of the paper and the forces associated with this direction are called cross or tangential forces.[3] In order to secure the eccentric position of the shaft and rotor at a given eccentricity stainless steel shims are inserted at location 11 in figure 2.6 and the bolts identified by the number 15 are tightened. Concentric tests and eccentric tests with an eccentricity up to the nominal gap of 29/1000 inch (29 mils) are possible. For safety reasons and to preserve the experimental facilities integrity, eccentricities are limited to a maximum of 18 mils.

The flow exits the test section into an exhaust plenum. In the exhaust plenum one can locate the optical encoder identified by 18 in Figure 2.6. This encoder broke well before any shrouded testing began. The encoder was an essential device which locked the sampling of forces by the dynamometer and its related equipment to 32 times every revolution no matter what the speed. A second method was developed in order to overcome the problem of the broken encoder. This method uses a 32 tooth gear mounted on the bottom section of the shaft with a proximeter probe facing the

[3]Remember, the presence of a cross force will be destabilizing if the cross force is in the direction of whirl. These are static experiments, whirl is inhibited, however, cross forces are measured.

teeth of the gear. The proximeter provides electrical signals identifying the passing of each gear tooth which provides a triggering mechanism similar to that of the optical encoder. Circuits were developed in order to take these electrical pulses and convert them to the method compatible with the existing equipment and software. This new method is not as reliable as the optical encoder and before the reliability problem was identified and solved this new method gave mysterious results which cost nearly a year of lost time. Further discussion of the reliability of this new triggering system is provided when the data reduction procedures are discussed.

2.2.2 Upper Turbine Test Section: Stator-Rotor Geometry

This facility is built with the capability to vary stator and rotor blade spacing along with the capability to vary the amount of gap between hubs of the stator and rotor. The geometrical variables are quite important, so much so, that Song devoted much of his work into investigating the variation of these parameters. Figure 2.7 presents these variables through a schematic diagram of the upper turbine test section. The variable d is the distance from the trailing edge of the stator blade to the mid-span of the leading edge of the rotor blade. The rotor-stator axial spacing is d=0.295 inches. The mid-span chord length, c, of the rotor blade is 0.870 inches. The rotor blade height is designated, B_H, and has a value of 0.652 inches. The blade height does not include any section of the shroud, which is shown as a black strip in Figure 2.7. The hub-to-hub distance between stator and rotor is d'=0.005 inches (5 mils). This distance can be easily changed by the insertion of spacers. In this work, a spacer of thickness 0.120 inches is used and in Figure 2.7 is represented by a black box attached to the stator. Once again the nominal gap is given by δ, and is 0.029 inches (29 mils).

The configuration of the axial gap in this shrouded turbine is the same as two of the configurations that were completed by Song in his unshrouded tests, namely, d'=0.57% and d=33.9% which are given as percent of chord.[15] The stator in these

shrouded tests is the same stator used in the Song's unshrouded turbine tests. This stator has an exit angle of $\alpha_2 = 70°$. In the unshrouded case it is fairly easy to calculate inlet conditions at the rotor because of the un-obscured flow field. Therefore, at this point the reader should be made aware of some of the difficulties that the shroud creates when one wishes to determine flow conditions at the rotor and at the shroud entrance. The flow reaches the seal region directly from the stator exit, leaving the stator with an angle to the axial direction of $\alpha_2 = 70°$, and the tangential velocity at the seal inlet is $(c_x)_{rotor} Tan70°$. Notice that, because of contraction, $(c_x)_{stator} < (c_x)_{rotor}$. In addition, the presence of the unrecessed shroud acts as an obstacle to the flow and further reduces c_x near the outer casing. Thus, some care must be exercised in estimating the tangential velocity at the shroud inlet. These estimates of tangential velocity are discussed further when the shroud theory is presented.

2.2.3 The Flow Loop

For all the test presented in this work Freon-12 is used as the working fluid. In order to pressurize the loop with the freon all the air must first be evacuated from the loop using a vacuum pump. Then the loop is pressurized with the freon by using standard holding canisters of pressurized freon. For all the tests, the loop was either brought to a stagnation pressure of 1.24 atm or 2.21 atm. The loop is capable of a maximum absolute pressure of 2.36 atm (34.7 psia). One should note that all the air can not be evacuated from the loop. The vacuum pump can bring the pressure within the loop down to 0.028 atm. If the vacuum pump is used before each run to evacuate the loop and then the freon is added to the loop, approximately 1% of the fluid is air when the loop is running at its design condition of 2.21 atm. In the tests it is assumed that the loop is pressurized with 100% Freon, therefore, the error in density may be calculated using equation 2.1.[13]

$$\%error = \frac{\chi_{air} M_{air} + (\chi_{Freon} - 1) M_{Freon}}{\chi_{air} M_{air} + \chi_{Freon} M_{Freon}} 100 \qquad (2.1)$$

The equation is derived from the ideal gas relations, where χ is the mole fraction and M is the molecular weight. For 1% air within the loop the density is overestimated by 0.77%. This has a negligible effect on the results. A more comprehensive treatment of the specifics of the experimentation and the results will be covered in the next chapter and it is seen section 3.1.3 that the air content within the loop was probably larger than the 1% discussed here.

The Freon is circulated throughout the loop by a 90 hp (67 kW) compressor driven by a General Electric 100 hp (75 kW) AC motor (see Figure 2.2). The compressor imparts energy to the freon and causes the Freon temperature in the loop to rise. The turbine absorbs approximately (15 kW), therefore, the heat exchanger is rated at 177,430 btu/hr (52 kW).

The mass flow rate is measured by a B I F Plastic Insert Venturi Tube, whose location within the loop can be seen at 8 in Figure 2.1. Throttle valves and a by-pass loop control the mass flow rate. The throttle valves are hand operated and are sufficient to control the mass flow rate for unshrouded turbine experimentation. However, shrouded turbine experimentation requires the use of the by-pass loop because the hand operated throttle valves prove to be insufficient to control the mass flow rate accurately. The flow through the by-pass loop is controlled by a servo driven butterfly valve and this loop allows a fraction of the flow that exits the heat exchanger to directly return to the compressor, thereby by-passing the turbine test section. This by-pass scheme may be followed in Figure 2.1.

The unshrouded turbine (investigated by Song) has an optimal efficiency of 79% at a mass flow rate of 4.48 kg/s for a wheel speed of 3440 rpm. Because of the reduced blade height, down from 0.941 in (23.9 mm) for the unshrouded turbine to 0.652 in (16.6 mm) for the shrouded turbine, with the wheel speed and the average

pressure remaining the same as in the unshrouded turbine the flow rate for best efficiency, theoretically should be reduced by approximately the same factor, to 4.48x(16.3/23.9) = 3.06 kg/s. A series of tests were conducted to verify this and to select the nominal conditions for the experimental tests into these destabilizing forces. A design operating point was found by varying the mass flow rate at turbine rotor speeds of 2000, 2408, 3000, 3440, and 3784 rpm and recording torque, pressure and temperature measurements in order to calculate the total-to-static efficiency. The result is shown in Figure 2.8. Figure 2.8 is a graph of efficiency vs. the mass flow rate for the speed of 3440 RPM, which was determined to be the speed where the optimal efficiency lies. It can be seen from Figure 2.8 that the flow rate which yields the highest efficiency is $\dot{m}$=3.15 kg/s. These tests were conducted at 2.2 atm mean pressure and they yielded results close to the simple estimate presented previously. It was decided, in analogy to the other configurations, to conduct static force measurements at the pressure of 2.2 atm, at the flow rate of 3.15 kg/s and at $\omega = 0.7\omega_D$, $\omega = 1.0\omega_D$, and at $\omega = 1.1\omega_D$. Since the shroud is not recessed, the efficiency of the shrouded turbine is somewhat degraded from that of the unshrouded turbine, $\eta_{ts} = 74\%$ for the shrouded compared to $\eta_{ts} = 79\%$ for the unshrouded [15]. The pressure ratios for 3440 RPM are shown in Figure 2.9 and are somewhat lower in this shrouded turbine, due to smaller flow acceleration in the stator.

2.2.4 The Transmission and Power Absorption System

The turbine operating point was discussed in the previous section which required one to have the knowledge of the complete operation of this facility. However, the process of controlling the speed of the turbine has not yet been explained completely. Therefore, in this section, a complete explanation of the transmission and power absorption system is given.

Once again, the transmission and power absorption system are shown in Figure 2.2 at location 14. This system is responsible for the absorption of the power created by the turbine as well as powering the turbine when the compressor is shut down. Two Hewlett Packard DC power supplies are used to provide power to the field and armature in the DC motor/generator. When the system is operating such as to absorb power only the motor's field has electricity supplied to it. The electrical energy created is then dissipated through a mesh of resistors. The resistors are cooled by air which is forced through the resistive network by the means of the M.I.T. Gas Turbine Lab steam ejector. During calibration and diagnostics the transmission and power absorption system is used as a motor and the turbine is rotated without the need of the compressor. Here both DC power supplies are used and they supply electricity to both the field and armature in the DC motor. Through these power supplies one is able to control the speed of the turbine for any type of test.

As mentioned in section 2.2.1 the turbine's rotor and upper shaft are displaced eccentrically in these experiments. In order to accommodate these displacements flexible couplings are used to connect the upper shaft to the intermediate shaft and the intermediate shaft to the lower shaft. These coupling and their locations may be seen in Figure 2.6 at locations 17 and 24. Along with special couplings to accommodate the shaft eccentricity a double faced seal was used at the point where the shaft exits the exhaust plenum (location 20 in figure 2.6). This seal is able to operate in both vacuum and pressure situations. The lower shaft of the turbine assembly is connected to the DC motor/generator through a belt and sprocket arrangement as shown schematically at locations 12 and 13 in Figure 2.2.

Details on the names and model numbers of the equipment used in the facility may be found in the work presented by Loose.

2.3 A Summary of the Design Parameters

Here the shrouded turbine's design parameters are reviewed and compared to the unshrouded turbine's and the SSME HPFTP turbine's design parameters. This is neatly accomplished through the use of a table. Table 2.1 lists and compares all the relevant design parameters of the three turbines .

2.4 Instrumentation

As mentioned previously, the destabilizing forces on an eccentrically rotating rotor may be measured and determined using two different methods. The first method is to directly measure the forces acting on the rotor through a series of strain gauges mounted directly below the rotor in the rotor's shaft. This device is called a rotating dynamometer and is explained in subsection 2.4.1. The second method, which gives only the pressure-derived part of the forces, is less direct than the first and involves the measurement of the static pressure distributions before, within and after the rotor's shroud. After integrating the circumferential static pressure distribution within the shroud using equations (1.15) and (1.16) one obtains the partial forces acting on the rotor. Nonuniformity in the circumferential pressure distribution creates the destabilizing forces and is the most important effect in the shrouded turbine. This effect dominant in the work done by Millsaps.[17] The instrumentation used in measuring the pressures in the test section and the location of this instrumentation is reviewed in subsection 2.4.2. The remaining force contribution is due to the Alford effect as described in section 1.4.2. This effect is determined through the measurement of the flow's circumferential velocity distribution before and after the rotor. Once again, the Alford effect is a blade tip clearance effect and because of the shroud this effect is reduced, but not negligible. The measurements of the flow velocity and the location of these probes are described in subsection 2.4.2. Blade tip clearance effects are dominant in the unshrouded turbine as is shown in the work of Loose and Song.[13,15] The summation of the forces due to the pressure effect and the Alford

Table 2.1: Design Parameters for the SSME HPFTP Turbine, Unshrouded Turbine and the Shrouded Turbine.

	SSME HPFTP	Unshrouded Turbine in M.I.T. Test Facility	Shrouded Turbine in M.I.T. Test Facility
Flow coefficient, ϕ	0.58	0.58	0.58
Work coefficient, ψ	1.508	1.508	1.508
Stator exit angle	70°	70°	70°
Relative rotor inlet angle	43.9°	43.9°	43.9°
Rotor exit angle	60°	60°	60°
Absolute exit angle	-3.1°	-3.1°	-3.1°
Degree of reaction	0.216	0.216	0.216
Rotor mean radius, cm (in)	12.88 (5.07)	12.88 (5.07)	12.53 (4.93)
Number of rotor blades	63	63	63
Rotor blade height, cm (in)	2.17 (0.854)	2.17 (0.854)	1.66 (0.652)
Rotor blade chord, cm (in)	2.21 (0.870)	2.21 (0.870)	2.21 (0.870)
Design rotation rate, rpm	34,560	3440	3440
Axial flow velocity, m/s (in/s)	262 (10,300)	26 (1020)	11 (433.1)
Mass flow rate, kg/s (slug/s)	71.8 (4.92)	4.48 (0.307)	3.15 (0.216)
Inlet pressure, kPa (psi)	34,950 (5069)	223.9 (32.5)	223.9 (32.5)
Inlet temperature, K (°F)	1053 (1436)	300 (80)	300 (80)
Pressure ratio	1.192	1.231	1.138
Efficiency	0.821	0.79	0.74

effect should equal that measured directly by the rotating dynamometer. Lastly, the data acquisition system is briefly reviewed in subsection 2.4.3.

2.4.1 Rotating Dynamometer

The rotating dynamometer is located directly below the rotor and can be seen at location 14 in Figure 2.6. Four equally spaced stainless steel square posts which run parallel to the rotors axis at a radius of 0.053 m (2.1 in) make up the structure of this dynamometer. Nine strain gauge sets are mounted on each post. The posts are 0.005 m (0.2 in) on the side and 0.0254 m (1.0 in) in length. Figure 2.10 shows the orientation of the these strain gauges on the stainless steel posts. These thirty-six strain gauges are wired such as to create nine sets of full wheatstone bridges which are sensitive to all components of force and moment. The wiring of these gauges is shown in schematic form in Figure 2.11 and this figure also illustrates which bridge is sensitive to which component of force and moment.[13]

The dynamometer rotates with the rotor since it is part of the shaft, therefore, the forces measured by these bridges must be converted from the rotating frame to an inertial reference frame. The procedure of converting the forces from the rotating frame to the inertial frame is explained in the next chapter where the actual experimentation is discussed and the experimental results are given. Note that since the bridges are rotating with the shaft the necessary wiring is also rotating. A slip ring assembly (location 23 in Figure 2.6) is used to transfer the signals from the rotating elements to the stationary amplifiers and data acquisition system. For details on the materials and amplifiers used one may consult the work of Loose.[13]

The dynamometer was calibrated by Loose and Song.[13,15] The calibration procedures yield a six-by-six calibration matrix, which is the slope of the voltage output of each bridge for each of the six components of force and moment. The effects of eccentricity and load showed that the bridge output was linear, therefore, the

calibration matrix is used in a linear algebraic expression in order to determine actual force from voltage. The output voltages of six bridges and the inverse of the calibration matrix associated with those six bridges are multiplied and result is a six component force vector. This is illustrated by equation 2.2:

$$\vec{f} = [B]\vec{V}_v \tag{2.2}$$

where $\vec{f}$ is the six component force vector, $[B]$ is the inverse of the calibration matrix and $\vec{V}_v$ is the six component voltage vector. Once again, this force vector is in the rotating frame and must be converted to the lab reference frame. This procedure is explained in the next chapter. A detailed explanation of the calibration procedures and techniques are given by Loose.[13]

The dynamometer was used in order to determine the lateral and torsional natural frequencies of the rotor-shaft assembly. It was found that the lateral natural frequencies of the system were at 105 Hz (1002.7 rpm) and 580 Hz (5538.6 rpm). All experimental tests were done between these two natural frequencies. It was also determined that the torsional natural frequency of the system occurs at 18 Hz (171.9 rpm)

2.4.2 Test Section Instrumentation

The test section which was described in sections 2.2.1 and 2.2.2 is heavily instrumented with proximity probes, wall pressure taps, velocity probes and thermocouples. In order to gain the greatest use of these instruments the casing of the test section can rotate so that a particular probe may be used at different circumferential locations. Combinations of these instruments are located at ten different axial locations and at several circumferential locations at a particular axial location. The eleven axial locations are numbered from 0 to 10 and each number's position in the test section is shown if Figure 2.12. In order to better understand what type of instrumentation is

located circumferentially at each axial location one is referred to Figure 2.13 which is modified from [15]. The top half of the figure shows the location of the eleven axial positions with respect to the stator and rotor. The bottom half of this figure shows the circumferential location and the type of probe at each of the eleven axial locations.

A Pitot static probe is located at station 0. This location is far upstream and mainly provides information about the loop total pressure and temperature. Station 1 is also far upstream while station 9 is far downstream. Both these stations have identical circumferential characteristics meaning that at each of these stations there reside two wall static ports 180° apart and two 3-hole velocity probes with thermocouples. The 3-hole velocity probes can measure both static and total pressure along with the temperature and the yaw angle of the flow. The purpose of these stations is to identify whether pressure and velocity non-uniformities exist far upstream and far downstream. Closer to the leading edge of the stator and to the trailing edge of the rotor one finds stations 2 and 8 respectively. Both these stations contain two 5-hole velocity probes each while only station 8 is instrumented with wall static ports. The 5-hole velocity probes can measure all that the 3-hole velocity probes measure along with the pitch angle of the flow. Once again, these stations are used to determine the degree of non-uniformity that exists in the flow at the entrance and exit of this turbine stage. Stations 3 and 4 are at the entrance to the stator and rotor respectively. These stations are composed solely of wall static pressure taps used to determine the extent of the pressure non-uniformity at these locations. One should note that the stator is attached to the outer rotatable casing, therefore, the stator rotates with the casing. In order to obtain a circumferential distribution of pressure between stator blades, five static pressure taps are equally spaced within the region between two stator blades. Stations 5 and 7 are close to the first and second seal knives respectively and contain two static wall pressure taps each which are 180° apart. The most important location within this rig for pressure measurements is location 6. This location is within the cavity of the shroud

and the non-uniformity in pressure associated with this location[4] gives rise to the destabilizing forces which this experimental facility was built to investigate. Eight static wall pressure ports are located at this axial location. Two proximity probes are also located here, however, they are of importance in unshrouded turbine tests rather than in these shrouded turbine tests. Station 10 is very far down stream and is not used in the experimental work presented here.

In order to read in all the information provided by the vast array of pressure measurements a 48 channel double Scanivalve system was used. The details of the calibration of all the for mentioned probes, and the calibration and detailed instrumentation of the Scanivalve system is provided by Loose and Song.[13,15]

2.4.3 Data Acquisition

Three analog-to-digital (A/D) converter systems connected to one IBM PC-AT are used to acquire and log all the data. Figure 2.14 is a flow chart representing the instruments used, the A/D systems incorporated and the IBM computer.

The voltage signals obtained from the bridges in the rotating dynamometer are first sent to conditioning amplifiers and then to a LeCroy sampling data logger. Ultimately the IBM PC obtains, logs and saves the data. The data logger is capable of handling 32 individual inputs at a sampling rate of 5 kHz with a 12 bit resolution. For a usual run, the sampling data logger is set to sample the bridge voltages 32 times per revolutions for 256 revolutions. The trigger information[5] was initially provided by an optical encoder, however, this device broke (as mentioned previously) and a 32 tooth gear and proximity system was devised instead. The problem with this new system is that it misfires at times and instead of providing a constant 32 signals per revolution it provides any number from 1 to 68. The data reduction software, which takes the raw

[4]It will be seen in chapter 4 that the non-uniformity in pressure at the entrance and at the exit of the rotor stage also contributes to the direction and magnitude of the destabilizing force.
[5]The trigger tells the sampling device when to sample a signal.

voltage signals and ultimately provides the steady inertial forces, assumed a constant 32 samples per revolution. Therefore, a misfire would alter the angle at which the forces would be projected onto the inertial frame[6]. This caused the results to have excessive scatter and in many cases prove meaningless. This problem was not immediately identified because a misfire would occur very rarely, most of the time it was once out of 256 revolutions and the existing software did not contain means of identifying such a problem. Once the problem was found the revolutions which contained samples other than 32 per revolutions were discarded. The capability of re-reducing the raw data without the troublesome revolutions existed because each run's raw data was saved. In order to re-reduce the runs and obtain the correct results the reduction software was re-written such that it counts the number of samples per revolutions and eliminates the revolutions which contain a number of samples other than 32. A complete explanation of the data reduction procedure is provided in Chapter 3 where the experimental results are presented.

Most of the pressure measurements are accomplished via the double scanivalve system. This system is then connected to a Scanivalve Digital Interface Unit (SDIU) where a two channel A/D exists and an internal memory system resides. The SDIU also controls the sampling of the pressures done by the double scanivalve system. The IBM PC ultimately receives the sampled pressure readings through an IEEE-488 output connection located at the rear of the SDIU.

The final A/D system converts the analog signals provided by the thermocouples, the Venturi system, the inlet pressure probe, and the lower torque bridge to digital signals read by the IBM PC. This A/D system is an interface card developed by Omega Engineering and plugs into the IBM computer. This card is operated through software provided by the company.

---

[6]The data reduction procedures and software is explained in Chapter 3 Experimental Results.

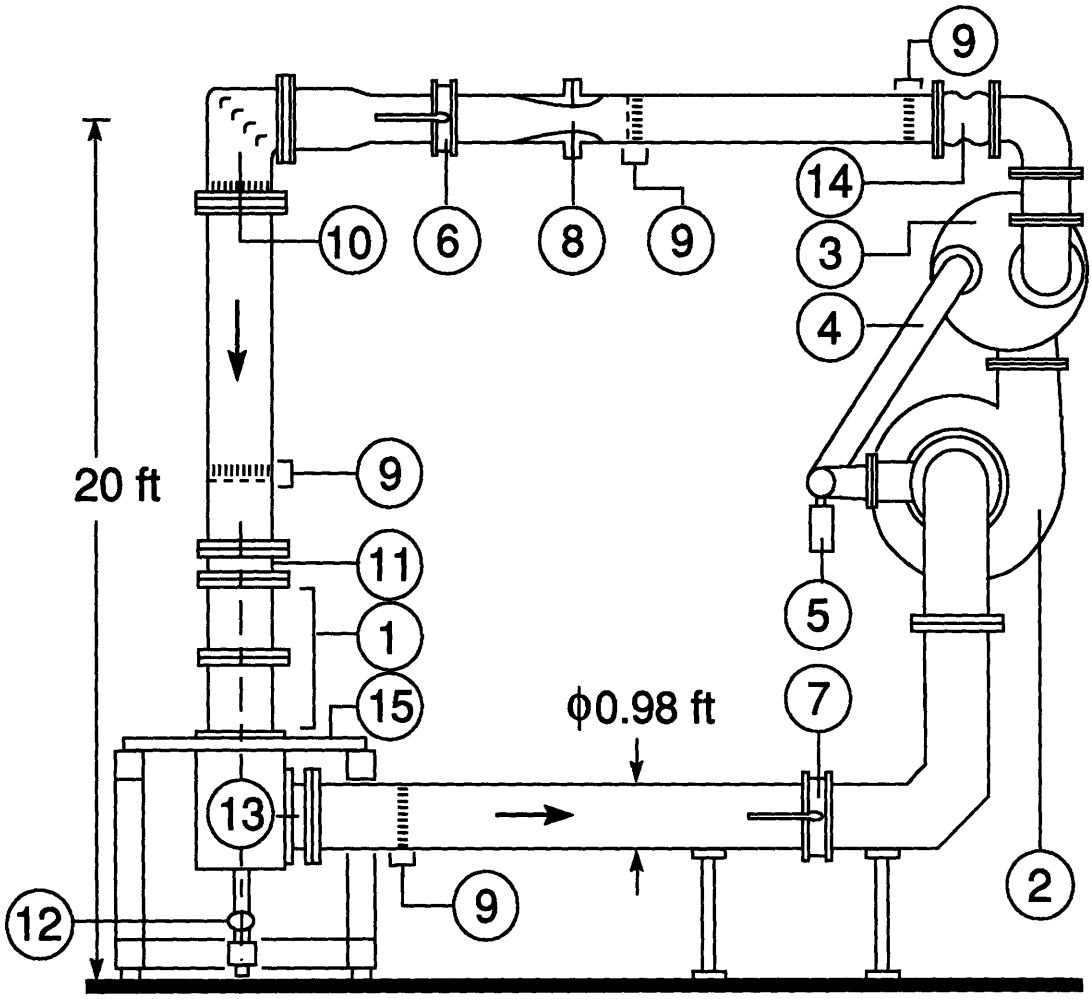

Figure 2.1: Front View of Experimental Facility. (1) Turbine Test Section, (2) 100 hp Electric Motor & Compressor, (3) Heat Exchanger, (4) By-Pass Loop, (5) Servo Driven Valve, (6) Throttle Valve, (7) Throttle Valve, (8) Venturi Meter, (9) Flow Straighteners, (10) 90° Bend with Flow Straightener, (11) Vibration Isolator, (12) Flexible Shaft Coupling, (13) Exhaust Plenum, (14) Vibration Isolator, (15) Test Stand [13]

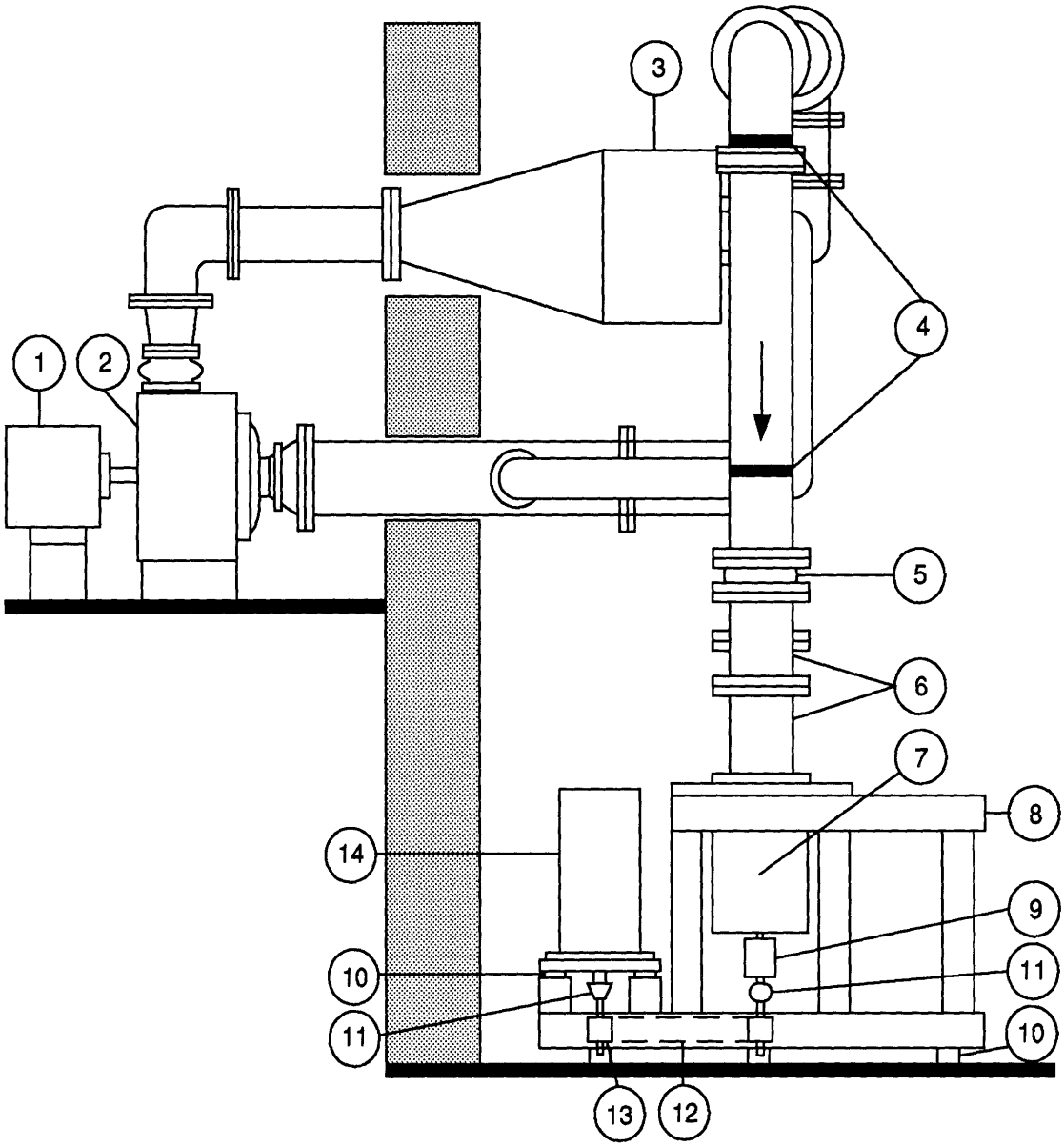

Figure 2.2: Side View of Experimental Facility. (1) 100 hp Electric Motor, (2) Compressor, (3) Heat Exchanger, (4) Flow Straightener, (5) Vibration Isolator, (6) Test Section, (7) Exhaust Plenum, (8) Test Stand, (9) Slipping Assembly, (10) Vibration Absorbing Mounts, (11) Flexible Shaft Coupling, (12) Drive Belt, (13) Pulley Sprocket, (14) DC Motor/Generator [13]

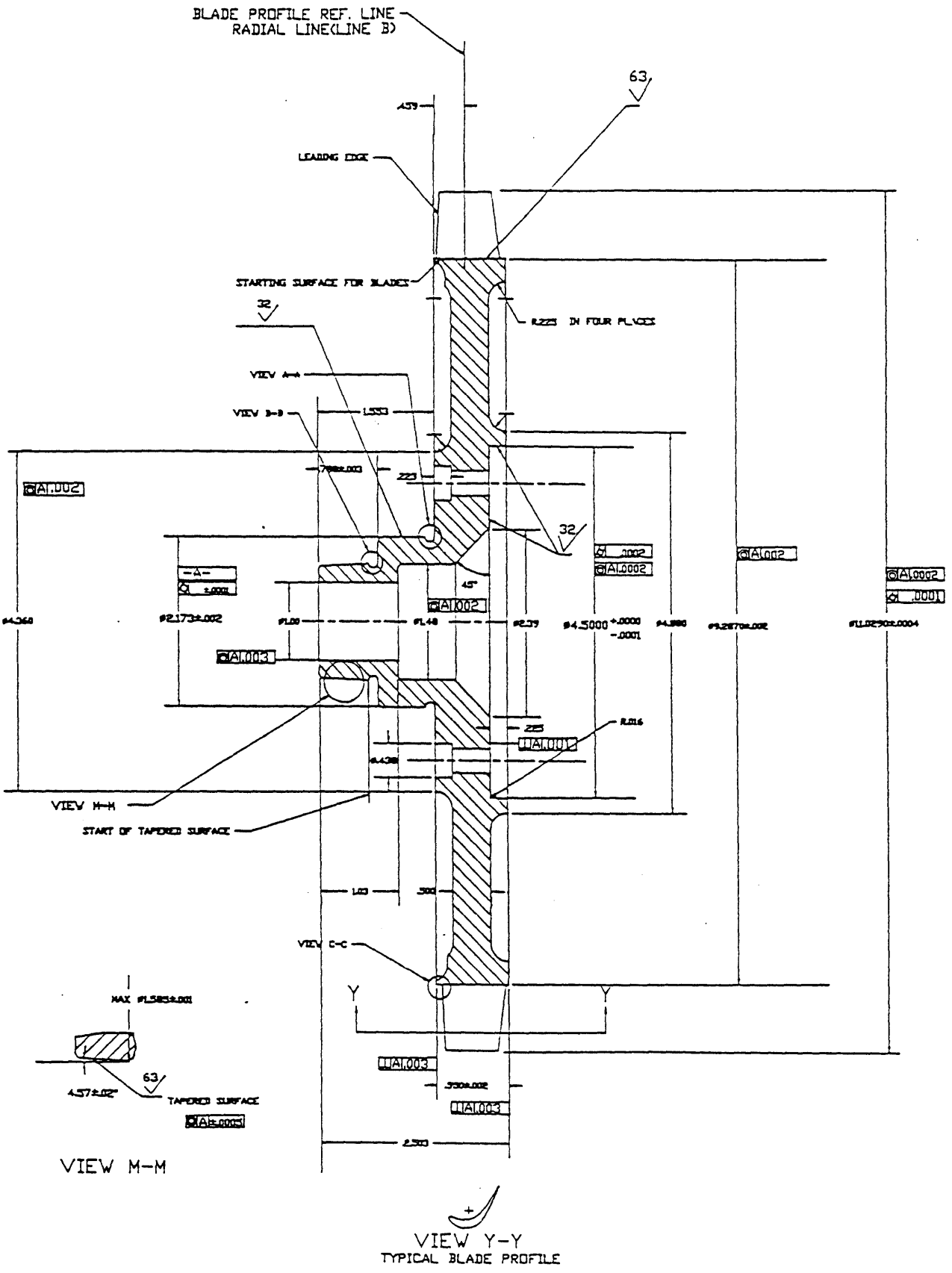

Figure 2.3: Machine Drawing of Turbine Test Rotor [13]

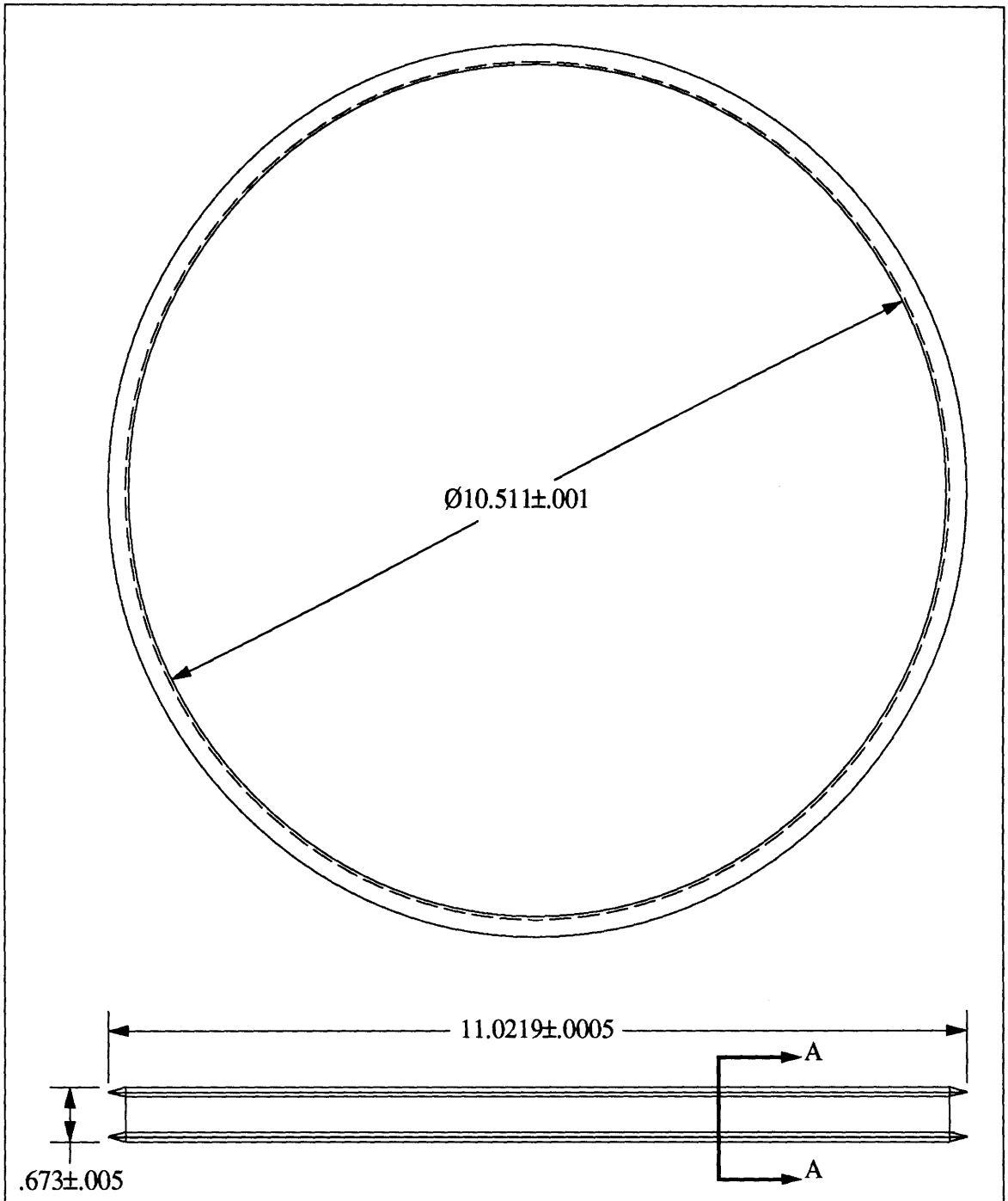

Figure 2.4: Shroud
Material: Stainless Steel
Scale: 1 to 4
Dimensions: inches

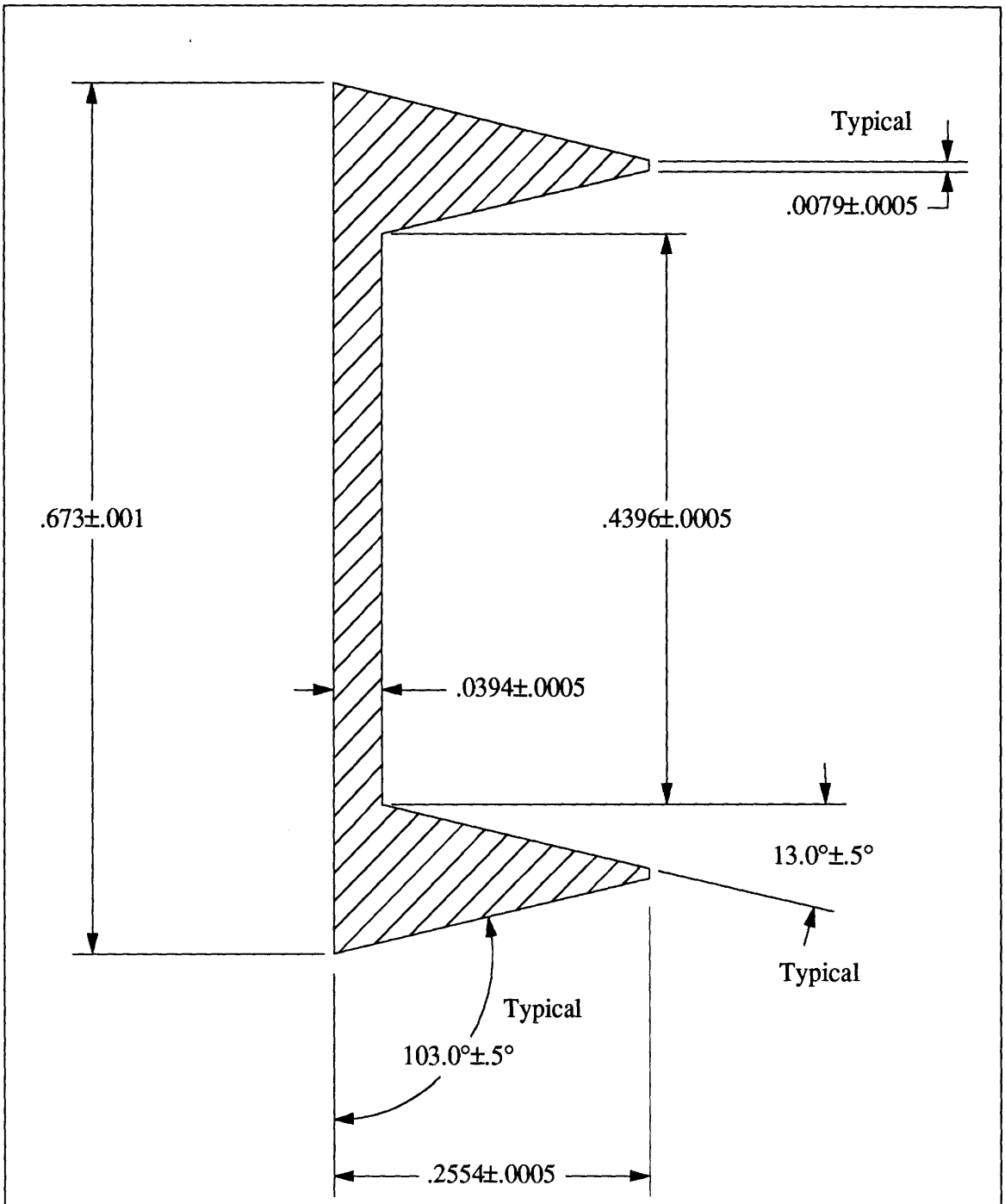

Figure 2.5: Cross Section A-A
Material: Stainless Steel
Scale: 1 to 8
Dimensions: inches

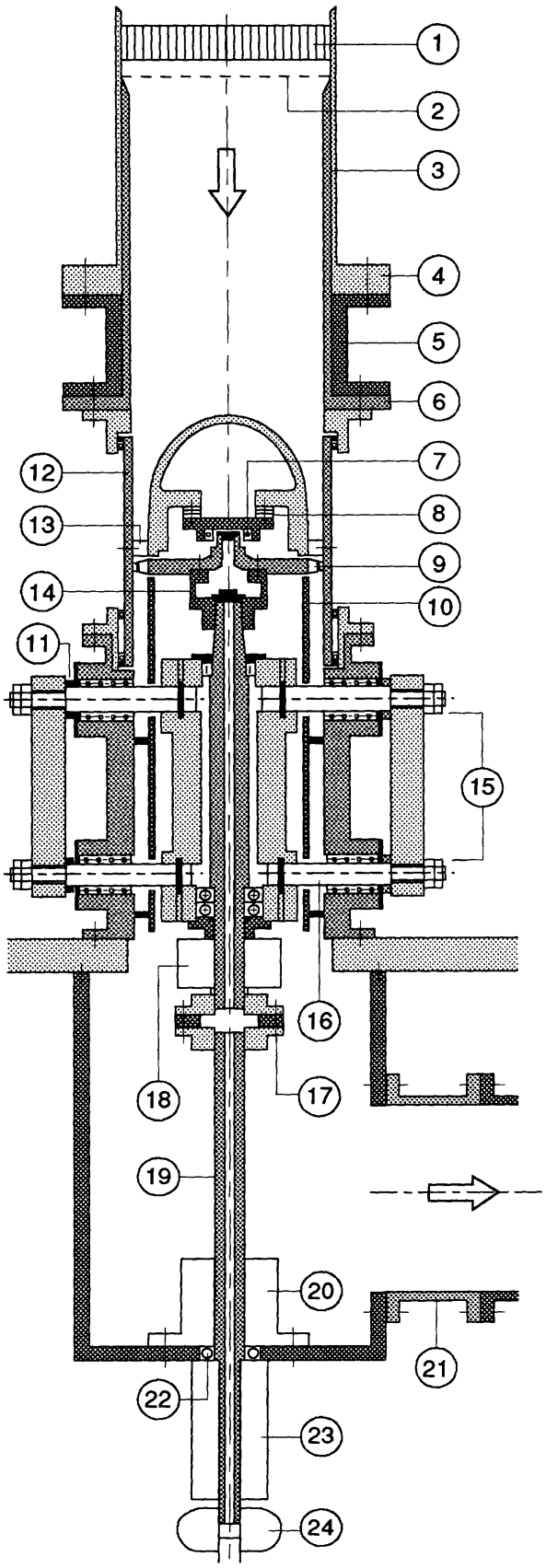

(1) Flow straightener
(2) Screen
(3) Main loop piping
(4) Flange
(5) Flexible insert
(6) Liner
(7) Snubber bearing
(8) Snubber support
(9) Test turbine
(10) Flow-smoothing shield
(11) Shims
(12) Rotatable casing
(13) Stator blades
(14) Rotating dynamometer
(15) Bolts to secure shaft
(16) Turbine-offsetting rods
(17) Upper flex joint
(18) Optical encoder
(19) Intermediate shaft
(20) Double-acting seal
(21) Flexible insert
(22) Pivoting bearing
(23) Slip ring assembly
(24) Lower flex joint

Figure 2.6: Schematic of the Turbine Test Section [15]

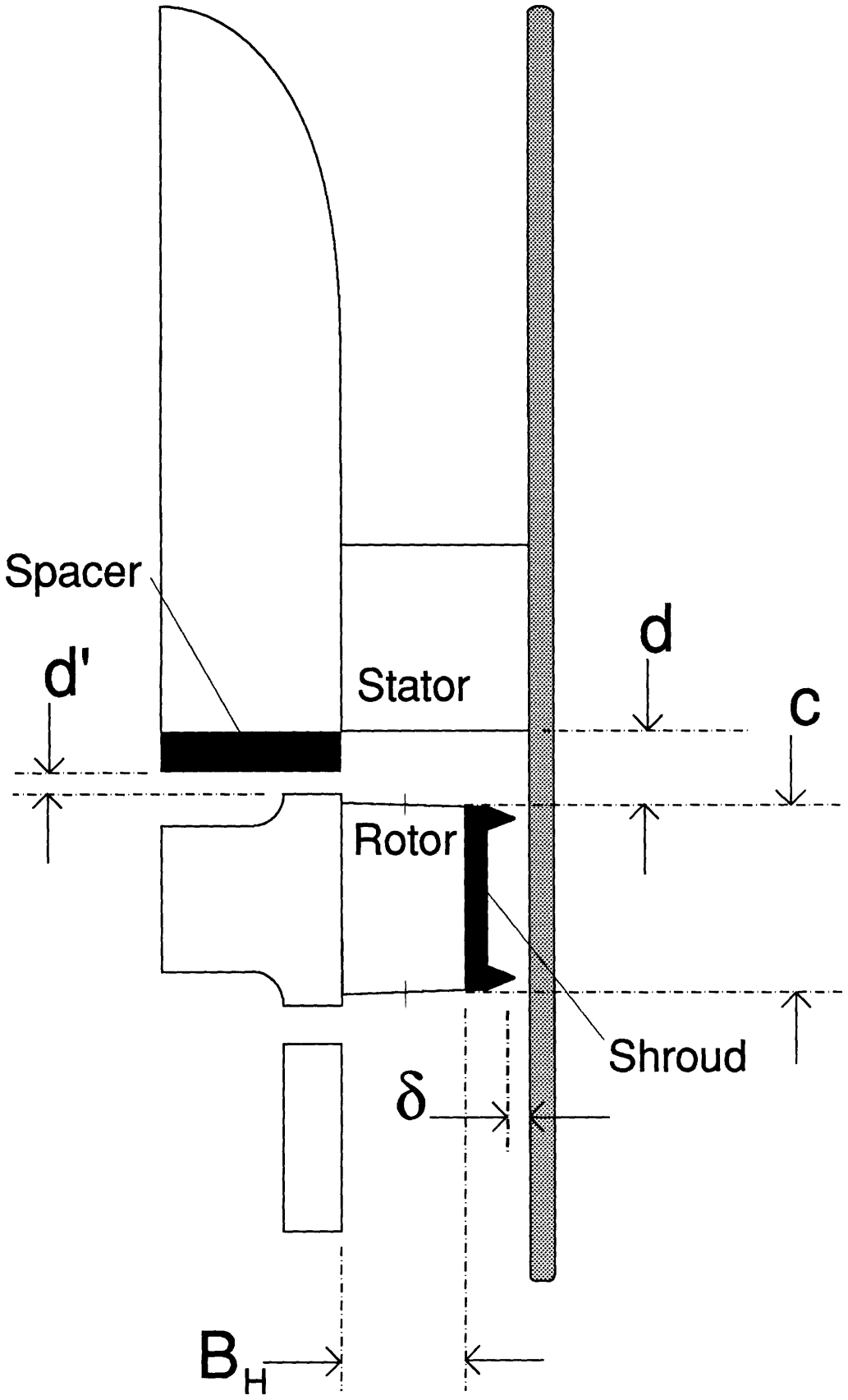

Figure 2.7: Schematic Illustrating the Pertinent Geometric Variables

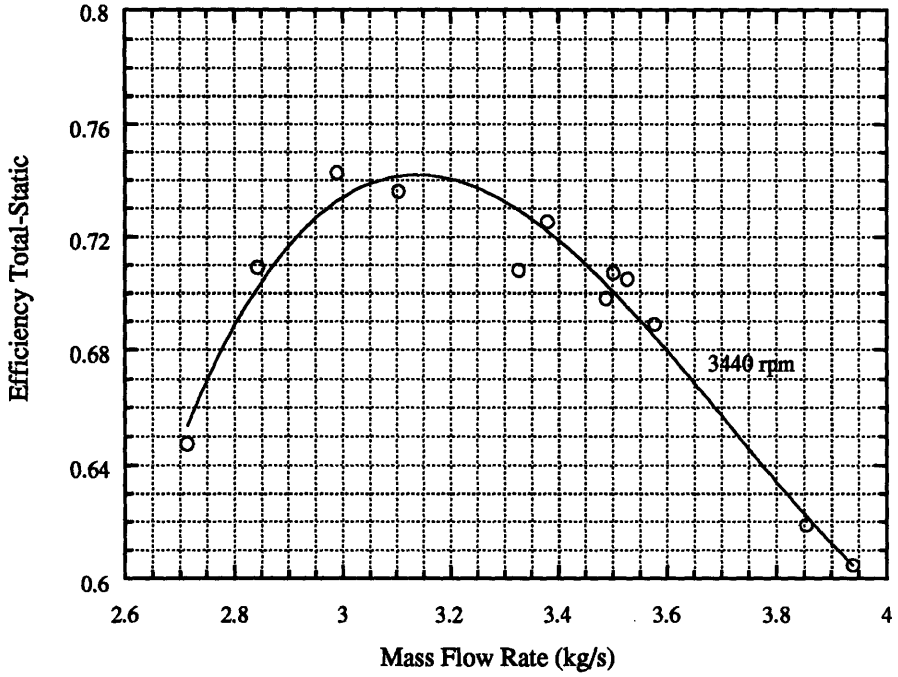

Figure 2.8: Total-to-Static efficiency vs. mass flow rate at optimal speed of 3440 rpm.

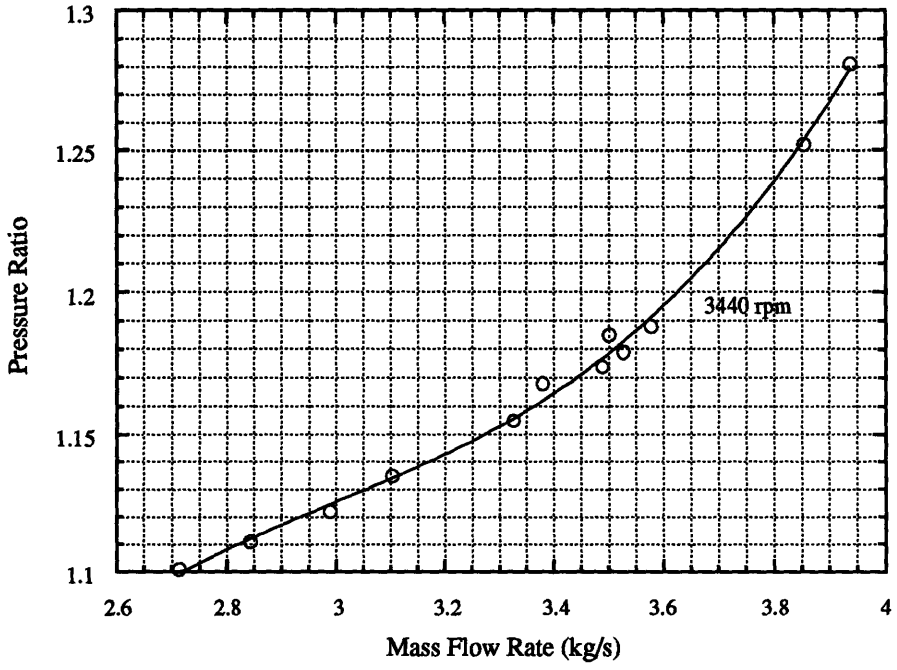

Figure 2.9: Pressure ratio vs. mass flow rate at Optimal speed of 3440 rpm.

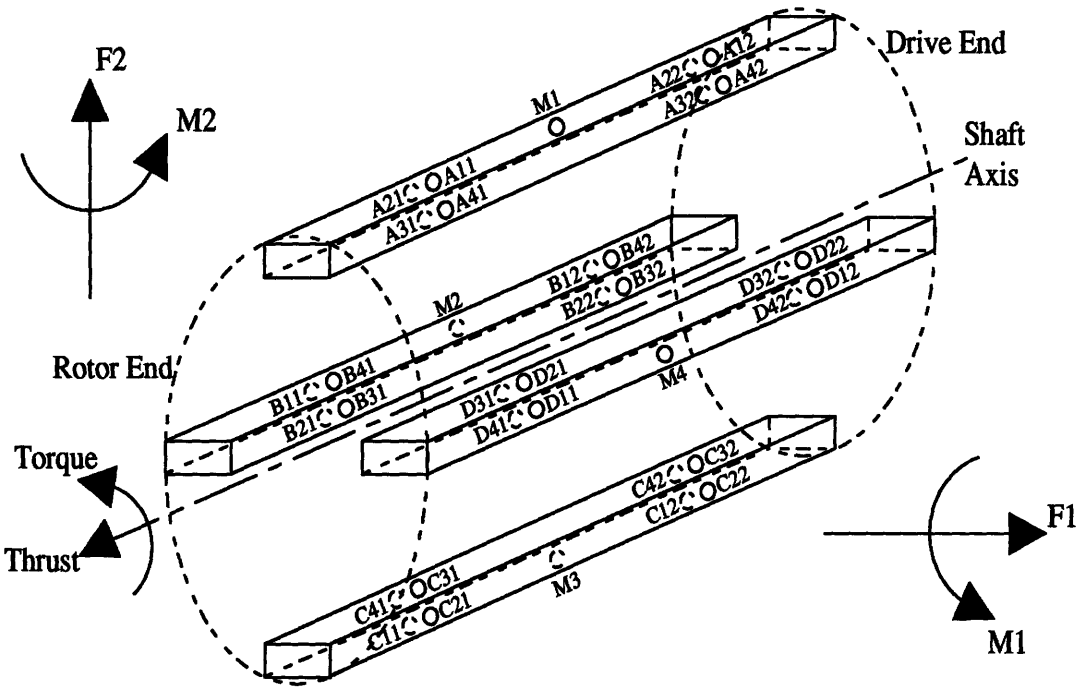

Figure 2.10: Schematic of the Rotating Dynamometer Showing the Four Stainless Steel Posts Which Contain the 36 Strain Gages. Each Post is Instrumented with 9 Strain gages: Four at Quarter Length, One at Mid Length and Four at Three-Quarter Length. Forces and Moments are Defined as Acting on the Rotor at the Rotor End of the Dynamometer.[13]

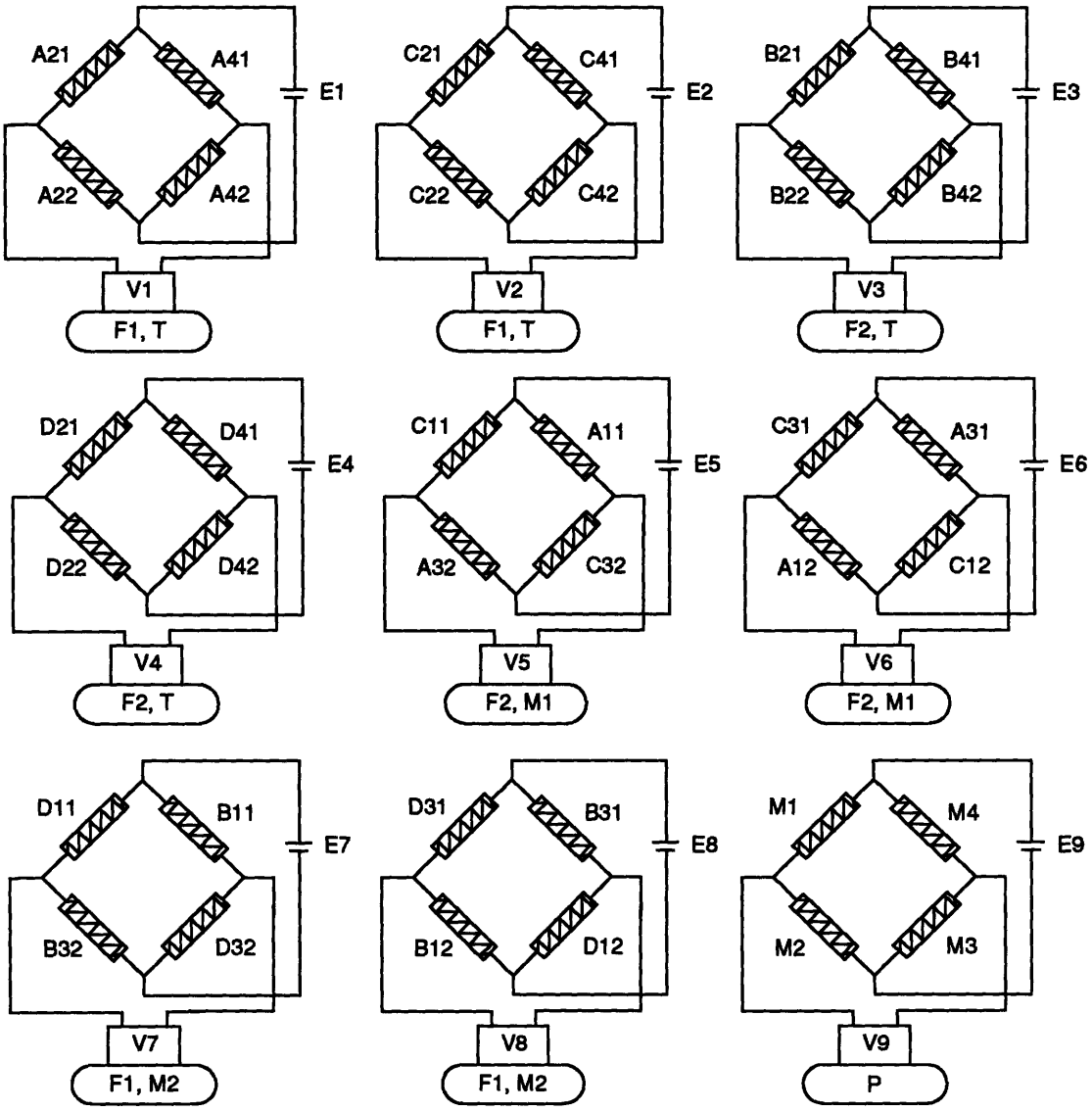

Figure 2.11: The wiring arrangement of the 36 semi-conductor strain gauges into the nine Wheatstone bridges. The excitation voltages are given by E1 through E9 and the bridge output voltages are given by V1 through V9. The sensitivity of each bridge is given in the oval below each bridge output voltage symbol.[13]

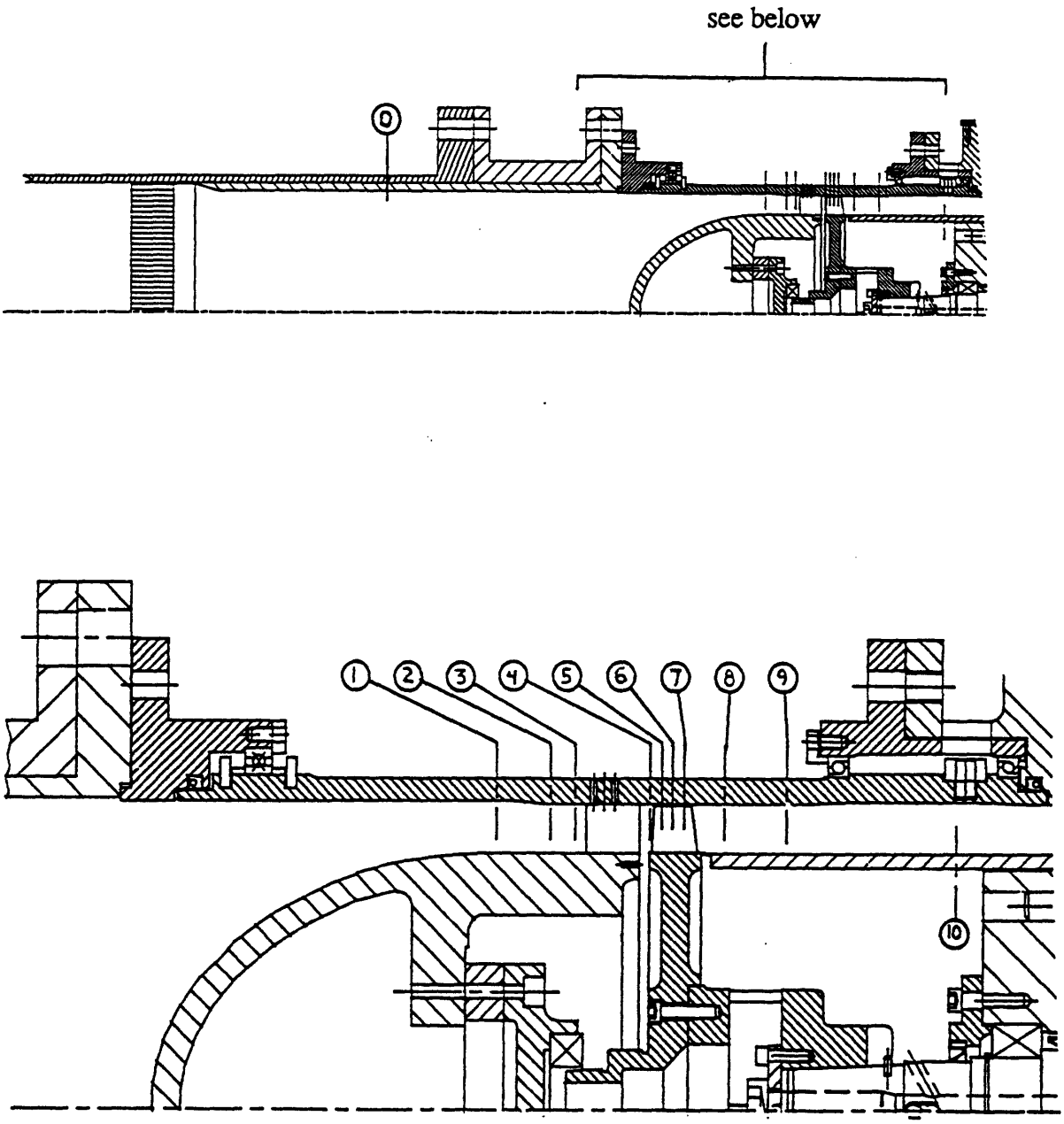

Figure 2.12: Axial Instrument Station Locations [13]

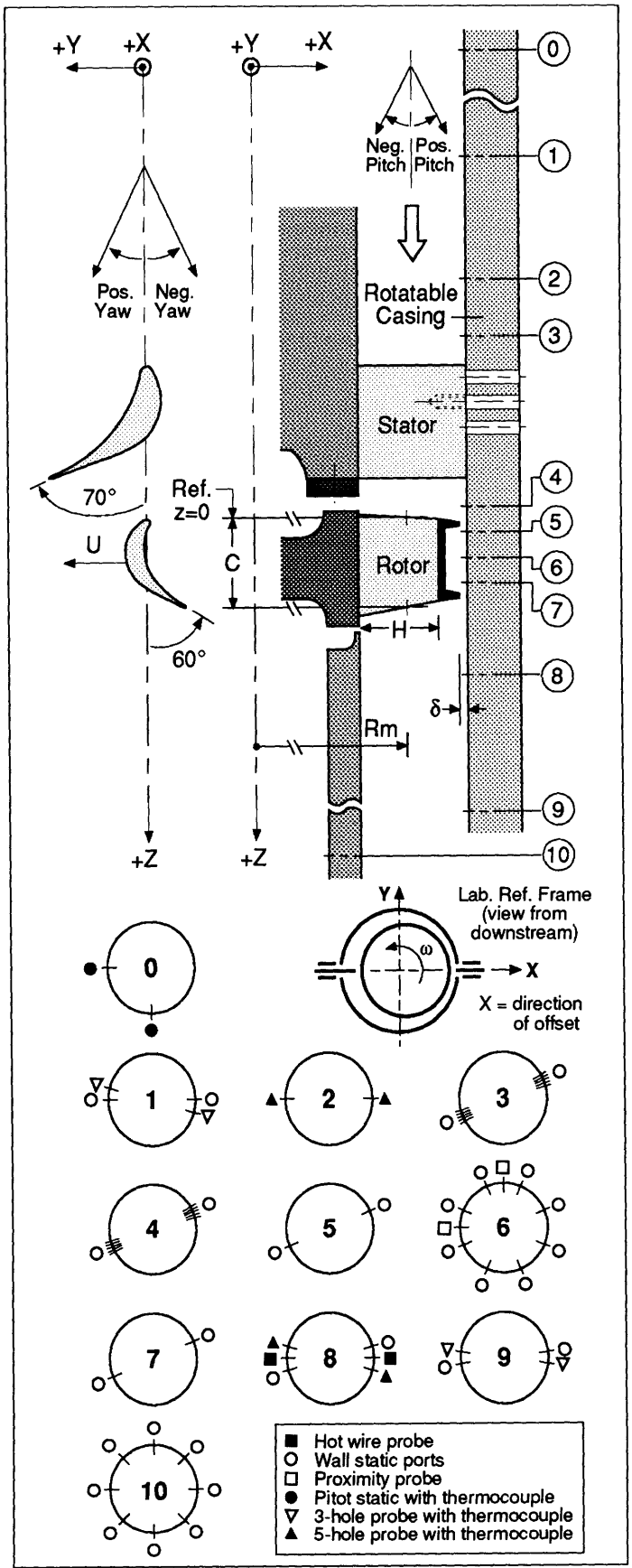

Figure 2.13: Types of Instruments used at each Station [15]

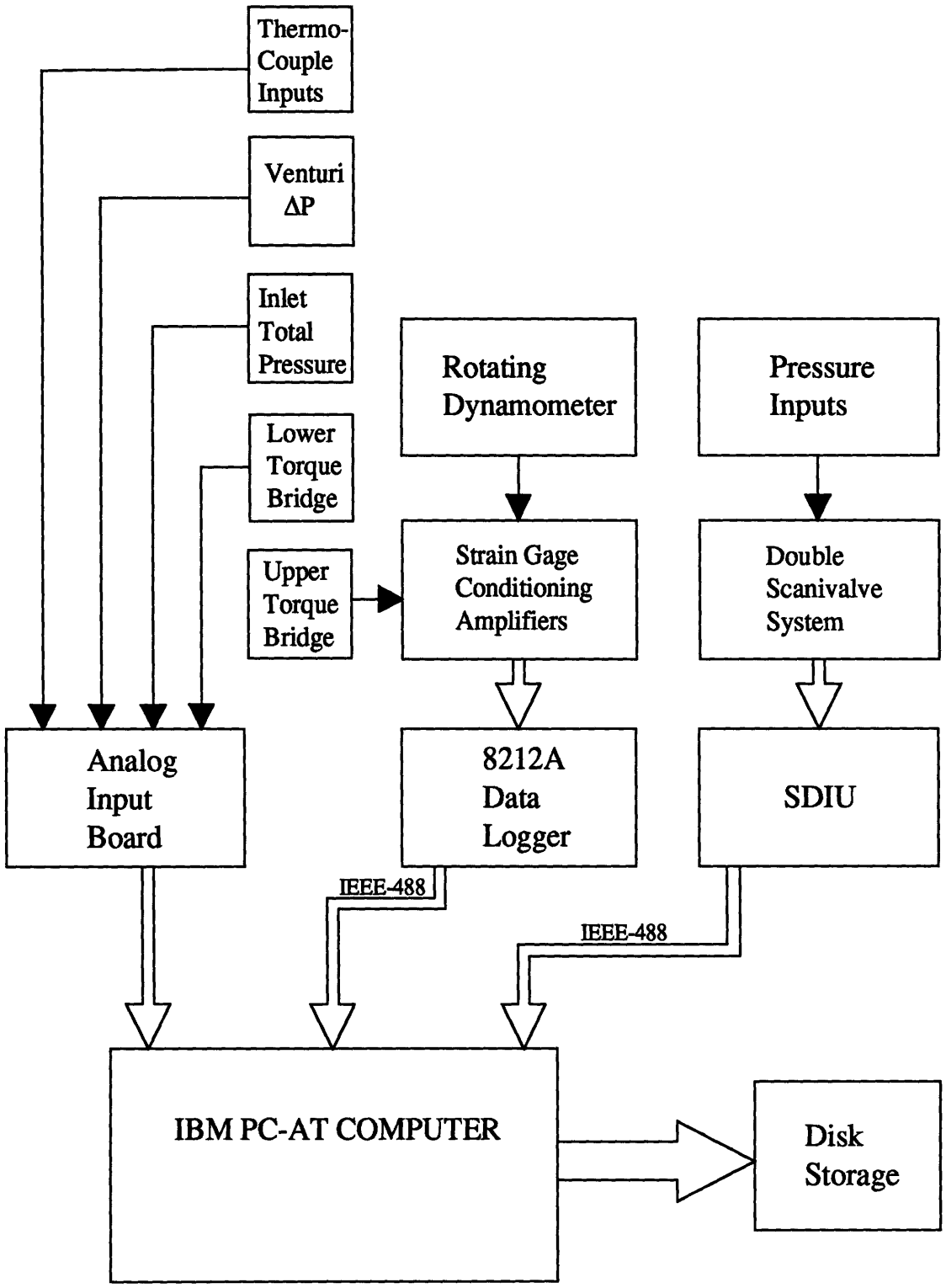

Figure 2.14: Flow Chart of the Data Acquisition Scheme [13]

Chapter 3

Experimental Results

3.1 Rotating Dynamometer Results

In this section the data reduction procedures to convert the raw voltages, provided by the rotating dynamometer, to forces in the inertial frame are explained. The series of tests are outlined followed by the results of those tests.

3.1.1 Reduction of the Raw Data

As mentioned in section 2.4.3 (Data Acquisition), 32 voltage samples of each of the nine Wheatstone bridges are taken per revolution for 256 revolutions by the LeCroy data acquisition system. This results in 8196 voltage readings per bridge for a single run at a given mass flow rate, rotational speed and eccentricity. In addition to reading the voltage output generated by the bridges, once per revolution signals created by a magnetic pickup[1] are also sampled. Other measuring devices are also connected to the LeCroy data acquisition system, however, those devices are used mostly for calibration purposes and are not required to be discussed here. After each run the raw voltage readings are transferred from the LeCroy to the IBM PC. These readings are then placed on 5.25 inch floppy disks and also converted to 3.5 inch floppy disks for permanent storage and for reduction on a Macintosh computer. A reduction routine was written for the Macintosh computer by Soomyung Yoo and later modified by the author. The modification checks weather each revolution contains exactly 32 samples.

[1]A magnetic pickup provides a large positive spike when a metal object is approaching its sensor and then immediately spikes negative as the metal object passes the sensor. A small metal piece was inserted on the lower shaft such that the magnetic pickup would sense this piece once per revolution.

If a revolution has more than or less than 32 samples that revolution is discarded. Before this reduction routine existed the IBM-PC and its related software were used for reduction, however, this system took orders of magnitude longer to reduce any given set of data.

The reduction routine written for the Macintosh first reads in the raw voltage readings which were originally saved on the IBM PC. Because an IBM was used to save the raw data the Macintosh program must first convert the numbers into a format that it can understand. Once these voltage readings are converted to a Macintosh format they are then stored in a 8196 by 10 array . Only the information from the nine wheatstone bridges and the magnetic pickup is stored in the array. The array contains a total of 8196 samples per bridge for each of the nine bridges and also 8196 samples from the once per revolution signal. Following the creation of this array the once per revolution signals are checked to determine whether a misfire has occurred for any of the 256 revolutions. The number of samples between the voltage spikes created by this magnetic pickup is one's guide in determining which of the revolutions are bad. If the number of samples in a revolution is larger or smaller than 32 a misfire has occurred an that entire revolution is discarded. The associated Wheatstone bridge voltage signals for that revolution are also eliminated. Once the bad revolutions are discarded, the remaining revolutions are averaged and the result of this averaging gives 32 six component vectors. The 32 vectors contain the average bridge readings for each of the 32 sample locations in a revolution. The vector has six entries because only six of the nine bridges are needed to determine the six components, namely the three components of force and the three components of moment. These 32 six component vectors are then multiplied by the calibration matrix as explained in section 2.4.1 (Rotating Dynamometer). The result of this linear algebraic multiplication are 32 six component vectors containing both forces and moments. Each of these vectors is the instantaneous force or moment at one of the 32 circumferential locations.

Our interests lie in the direct (X-axis or normal) and cross (Y-axis or tangential) forces, therefore, only two components of the six component vector are used. These forces must be converted from the rotating frame to the fixed frame and Figure 3.1 is referred to in order to aid in this discussion. In Figure 3.1 e is the eccentricity of the rotor, ϕ is the angle to the X-axis at time $t = 0$ at which time sampling begins, $F_1(0)$ & $F_2(0)$ are the forces at the first sample location ($t = 0$), ψ is the angle at time t after the initial sample and $F_1(t)$ & $F_2(t)$ are the respective forces. The positive X-axis is to the left and this corresponds to moving the shaft eccentrically to the left as one looks down onto the test facility from above. The positive Y-axis points up which corresponds to the axis pointing towards the power absorption system when one looks down into the test section from above. Equations (3.1) and (3.2) are used to convert the forces from the rotating frame to the fixed or inertial frame.

$$F_x(\psi) = F_1 Cos(\psi - \phi) + F_2 Sin(\psi - \phi) \tag{3.1}$$

$$F_y(\psi) = F_1 Sin(\psi - \phi) - F_2 Cos(\psi - \phi) \tag{3.2}$$

Once converted to the inertial frame 32 forces per revolution in both the X and Y directions result. These forces in each direction are then averaged over all the revolutions to obtain the final fixed reference frame direct (normal) and cross (tangential) force.

The direct and cross force obtained from the above procedure are for one test run. The turbine is set at an eccentric location, the mass flow is adjusted to the design flow rate and the turbine is operated at a steady speed. This reduction routine is repeated for every test run performed and the following section describes the battery of test completed using the rotating dynamometer to find these forces.

3.1.2 Test Series

It has been determined in section 2.2.3 (The Flow Loop) that the design speed and mass flow rate are 3440 rpm and 3.15 kg/s respectively. Thus, the testing is centered about this design condition. The three speeds investigated are 2408 rpm ($0.7\omega_D$), 3440 rpm ($1.0\omega_D$) and 3784 rpm ($1.1\omega_D$). These speeds are identical to the three speeds investigated in the unshrouded turbine tests performed by Song.[15] 6 eccentric positions and the concentric position are tested for each of these speeds. The eccentric positions investigated are for turbine rotor displacements of -15, -10, -4, +4, +10, +15 mils (thousands of an inch) where positive indicates a displacement in the positive X-direction as indicated in Figure 3.1. Three independent test runs are taken at each speed and each eccentricity. Therefore, a test series consists of 63 individual test runs. For example, three independent test runs are taken at 2408 rpm at an eccentricity of -15 mils. An entire test series is completed in one day.

Four test series were completed for the shrouded turbine. Two of the series were done at 1.24 atm mean loop pressure and the other two series were completed at 2.21 mean loop pressure. Originally, the reason for completing four test series was that the results had excessive scatter and were, in many cases, meaningless. Therefore, it was determined that the experimentation must be continued aggressively in order to find the cause of the bad results. As has been explained above, the problem was found and corrected, and the four series of tests completed were all salvaged and proved to be very repeatable. The results of these tests are now presented.

3.1.3 Rotating Dynamometer Results

To illustrate the results each test series is divided into three figures. One figure for each of the three speeds (2408 rpm $\{0.7\omega_D\}$, 3440 rpm $\{1.0\omega_D\}$ and 3784 rpm $\{1.1\omega_D\}$). On each figure the direct (normal) and the cross (tangential) forces (lbf) at a given speed are plotted vs. eccentricity (mils). Through these data points a least square linear curve fit was performed. Above each figure one finds the legend which contains

the linear fit equations and the goodness of fit. The test series number and the mean loop pressure are given in the title of each figure. A negative direct force, F_x, is a restoring force. For a positive eccentricity, following the convention given in Figure 3.1, a negative direct force acts in the direction opposite to the displacement (towards the concentric position). A positive cross force, F_y, act in the direction of rotation following the convention given in Figure 3.1.

Figures 3.2 through 3.13 contain all the results of the rotating dynamometer tests and Table 3.1 gives greater detail on the conditions of each test series at a given speed.

Table 3.1: Test Conditions and Measured Torque for Dynamometer Tests

Test Series	ω/ω_D	P_0(atm)	$\dot{m}$(kg/s)	T_Q(N m)
1	0.7	2.21	3.22	23.68
1	1.0	2.21	3.20	18.84
1	1.1	2.21	3.22	17.32
2	0.7	1.25	1.75	13.87
2	1.0	1.24	1.70	9.76
2	1.1	1.24	1.78	9.99
3	0.7	2.21	3.16	23.36
3	1.0	2.21	3.19	18.27
3	1.1	2.21	3.14	16.89
4	0.7	1.24	1.74	13.77
4	1.0	1.24	1.75	10.69
4	1.1	1.24	1.75	9.79

The figures are organized such that each successive group of four figures is at one speed and the first two figures of each group are tests performed at a mean loop pressure of 2.21 atm and the second two figures of each group are tests performed at a mean loop pressure of 1.24 atm. All these figures show that the results are very repeatable within each test series at a given speed. Remember, that each point on the graph contains three runs and if only one point is seen it is because the results lie right on top of one another.

The slope of the linear curve fits, $\frac{F_x}{e}$ and $\frac{F_y}{e}$, are shown in Table 3.2. Note that each of these slopes are adjusted to 2.21 atm. This means that for the runs performed at 1.24 atm, those runs were multiplied by 2.21 and divided by 1.24. Since the experiments are done statically the slopes give the direct and cross stiffnesses.

Table 3.2: Slopes of Linear Curve Fits in lbf/mil. Adjusted to 2.21 atm.

Test Series	Slope$_x$ k_{xx} $\frac{\omega}{\omega_D}=0.7$	Slope$_y$ k_{xy} $\frac{\omega}{\omega_D}=0.7$	Slope$_x$ k_{xx} $\frac{\omega}{\omega_D}=1.0$	Slope$_y$ k_{xy} $\frac{\omega}{\omega_D}=1.0$	Slope$_x$ k_{xx} $\frac{\omega}{\omega_D}=1.1$	Slope$_y$ k_{xy} $\frac{\omega}{\omega_D}=1.1$
1	-0.134	0.202	-0.147	0.158	-0.143	0.151
2	-0.139	0.201	-0.147	0.168	-0.150	0.158
3	-0.136	0.199	-0.144	0.167	-0.147	0.156
4	-0.136	0.195	-0.140	0.151	-0.142	0.152
Average	-0.136	0.199	-0.144	0.161	-0.145	0.154
Max. Diff.	3.7%	3.6%	5.0%	11.3%	5.3%	4.6%

As can be seen, an average of each row is given at the bottom of the table. It was stated previously that the results are very repeatable within one day's or test series experimentation, however, the repeatability is a little worse when one compares the

results from test series to test series. In Table 3.2 the bottom row presents the worst difference between test series at a given speed. This was calculated by taking the difference between the largest and smallest slopes and then dividing by the smaller slope. It can be seen that for all but one column the maximum difference between runs is 5.3%. Because of the cross force of test series 4 at design speed this column has a maximum error of 11.3%. If that one case is eliminated the error falls to 6.3%. An error of approximately 5% is reasonable and expected since between test series the loop was not always fully evacuated[2]. The freon from previous runs was left within the loop and as days passed between runs a small amount of air was expected to leak in. Instead of evacuating the entire loop and repressurizing, this alternate procedure was used in order to save Freon. The project ran out of funding and the small amounts of Freon left had to suffice for the rest of the experimentation.

The slopes of the linear curve fits are also used to calculate the Alford coefficients, β_x and β_y. These coefficients are given by equations (1.17) and (1.18) in section 1.4.2. In order to calculate these coefficients the blade height of B_H=16.6 mm (0.652 in) and the mean radius of R_m=125 mm (4.932 in) [3] are needed along with the torque values for each test series which are given in Table 3.1. The results are tabulated in Table 3.3.

These Alford coefficients may be directly compared to those obtained from the work of Song.[15] His experimental work utilized this same turbine, however, without the shroud. The rotors blades were longer since in order to incorporate a shroud the rotor blades had to be clipped. With the shroud the Alford coefficients are approximately 50% larger than those measured in the experimental facility utilizing the unshrouded turbine. Once again a maximum difference for each test series at a given speed is calculated. As one would expect, the difference increases from the differences

[2]For a fully evacuated loop which is then pressurized with freon has a density error of approximately 0.77%. (See Section 2.2.3) However, this ideal method could not be used because of budget constraints.
[3]Note that the mean radius is taken from the hub to the tip of the blade, not to the tip of the knife edge on the shroud.

presented in Table 3.2 because the non-dimensionalization contains a torque measurement which introduces further errors. The errors for the off-design cases are no larger than 7.4%, however, the design case has errors of 15.0% and 21.4% for the direct and cross Alford coefficients respectively. Most of this large error is due to test series 4 as was the case in the pervious discussion about the slopes. If the values from this series were eliminated the maximum difference would become a little more reasonable at 8.4% and 15.2% for both the cross and direct Alford coefficients respectively.

Table 3.3: Alford Coefficients from the Dynamometer Tests

Test Series	β_x $\frac{\omega}{\omega_D}=0.7$	β_y $\frac{\omega}{\omega_D}=0.7$	β_x $\frac{\omega}{\omega_D}=1.0$	β_y $\frac{\omega}{\omega_D}=1.0$	β_x $\frac{\omega}{\omega_D}=1.1$	β_y $\frac{\omega}{\omega_D}=1.1$
1	-4.05	6.10	-5.58	6.00	-5.92	6.25
2	-4.05	5.88	-6.05	6.91	-6.04	6.36
3	-4.16	6.11	-5.64	6.53	-6.22	6.61
4	-3.98	5.69	-5.26	5.69	-5.82	6.25
Average	-4.06	5.94	-5.63	6.28	-6.00	6.37
Max. Diff.	4.5%	7.4%	15.0%	21.4%	6.9%	5.8%

For comparison with the results presented by Millsaps [17], Table 3.4 takes the non-adjusted linear curve fits from Figures 3.2 through 3.13 and creates the stiffness coefficients. The stiffness coefficients are given by the following equation:

$$\overline{K}_{xx,xy} = \frac{\left(\frac{F_{x,y}}{e}\right)\delta^*}{lR_m(p_i - p_o)} \tag{3.3}$$

Where $\frac{F_{x,y}}{e}$ is the slope of the line, δ^* is the nominal gap, l is the length of the land, R_m is the mean radius and $(p_i - p_o)$ is the pressure difference across the rotor. These

values can be compared to those obtained from the seals rig, except that here $\overline{K}_{xx} < 0$ is a restoring force, whereas in Millsaps work the opposite convention is used. Note also that these contain both, the pressure effect and the blade (work loss) effects where as Millsaps facility concentrated on the shroud alone (the pressure effect).

Table 3.4: Stiffness Coefficients from the Dynamometer Tests

Test Series	$\overline{K}_{xx}$ $\frac{\omega}{\omega_D} = 0.7$	$\overline{K}_{xy}$ $\frac{\omega}{\omega_D} = 0.7$	$\overline{K}_{xx}$ $\frac{\omega}{\omega_D} = 1.0$	$\overline{K}_{xy}$ $\frac{\omega}{\omega_D} = 1.0$	$\overline{K}_{xx}$ $\frac{\omega}{\omega_D} = 1.1$	$\overline{K}_{xy}$ $\frac{\omega}{\omega_D} = 1.1$
1	-0.440	0.662	-0.437	0.470	-0.401	0.424
2	-0.448	0.649	-0.412	0.471	-0.479	0.504
3	-0.410	0.602	-0.435	0.504	-0.435	0.462
4	-0.469	0.670	-0.436	0.472	-0.434	0.466
Average	-0.441	0.646	-0.430	0.479	-0.437	0.464

3.2 Wall Tap Static Pressure Results (The Pressure Effect)

In this section the data reduction procedures used to obtain the static pressure at various circumferential locations for 6 axial locations is explained. The series of tests is then outlined followed by the results of those tests.

3.2.1 Reduction of the Raw Data

In order to calculate the direct and cross forces the nonuniformity in pressure at axial location 6 is measured[4]. Axial locations 4, 5, 7, 8 and 9 are also measured and the results and importance of those tests is also discussed below. As mentioned in section 2.4.2 the wall tap pressure is measured with the aid of a double scanivalve system which is controlled by an IBM PC-AT Computer. The measurements taken by this

[4]If one is unfamiliar with the numbering of the axial locations please review section 2.4.2 and refer to Figures 2.12 and 2.13.

scanivalve system are also stored on the PC. Each time the scanivalve system samples the wall tap pressures, it samples the pressure at all the wall tap locations throughout the test section. However, for the tests presented here only the wall tap pressure readings at axial locations 4 through 9 are fully reduced. A program written by Song for the Macintosh computer is used to reduce this data. For each sampling the program reads in the pressure values for all the circumferential locations at the six axial locations of interest and then takes the eight circumferential readings at station 6 and averages them for use as a reference point. This reference pressure is then subtracted from each of the wall tap pressure measurements taken at each of the six axial locations. The resulting pressures are stored in an array such that measurements taken at a particular circumferential and axial location for the concentric operation of the shrouded turbine are subtracted from the results of the eccentric operation. Before the results of these tests are presented the following section explains the series of tests that were accomplished.

3.2.2 Test Series

The wall tap pressure experiments were done at the design speed (3440 rpm) and at the design mass flow rate (3.15 kg/s). Two cases are investigated; the first is the concentric rotation of the turbine and the second is the eccentric rotation. The eccentricity was set to +18 mils. A sample run consists of setting the turbine either concentrically or eccentically, bringing the turbine to its design condition and then triggering the scanivalve system to read all the wall tap pressure ports. Once a sample run is completed the casing is rotated such that the wall tap pressure ports may read the pressures at a different circumferential location. Six circumferential locations are investigated. These same six circumferential locations are measured seven times at identical operating conditions. This will show the repeatability of the data. Therefore, a test series consists of operating the shrouded turbine at its design condition while

taking wall tap pressure measurements seven times at each of the six circumferential locations for both the concentric and eccentric rotor positions[5]. Two test series are reviewed in this work, both at a mean loop pressure of 2.21 atm, however, each test series is done on a different day. The results of these test are presented in the next section.

3.2.3 Wall Tap Pressure Results

In the experimental facility the shrouded turbine is displaced statically in what is defined as the X-direction. As was seen in previous figures, when the test facility is viewed from below (downstream) as in Figure 2.13 the positive X-direction points to the right and the Y-direction points upward, however, when the facility is viewed from above (upstream) as in Figure 3.1 the positive X-direction points to the left and the Y-direction is unchanged. In order to define the circumferential positions Figure 3.14 is referred to and it presents the facility coordinates as viewed from the top (upstream). At the minimum gap or at a positive displacement the circumferential position is $\theta = 0°$. It is shown below that at station 6 (within the shroud seal cavity) the minimum pressure occurs at $\theta = 127°$ and the maximum pressure occurs at $\theta = 307°$ in the direction of rotation. With the pressure skewed in this manner one does expect a forward-whirling cross force, and as one knows there is one because of the dynamometer results. There would be a zero cross force only if the minimum pressure occurred at $\theta = 180°$ and the maximum at $\theta = 0°$ or *vice versa.*

The graphs of the pressure perturbation around the circumference of the inner casing at the six axial locations are all presented in a similar manner. The Y-axis is the difference in pressure between the concentric and eccentric runs for a given station. The units are in psid. The X-axis is the circumferential position as defined in the

[5]The actual reason why seven trials are performed is because the velocity probes used to calculated the Alford effect move radially at each of the circumferential locations. Therefore, at each of the circumferential locations seven different radial measurements of the velocity are performed. The Scanivalve not only acquires wall tap pressure measurements but velocity information also. Section 3.3 explains this further.

previous paragraph using Figure 3.14. All the figures except those used to show the activity at station 8 have a curve defined by equation (3.4) fitted through the data points for a given trial.

$$\Delta P = m1 + m2Sin(\theta) + m3Cos(\theta) \tag{3.4}$$

Each trial has it own curve and the trial and its respective curve are represented in a legend above each graph. The sinusoidal curve fits at station 6 along with equations (1.15) and (1.16) are used to calculate the direct and cross forces. The averages of the magnitude and phase of the curve fits at stations 4 and 9 are used as inputs for the analytical model which is derived in chapter 4 and is applied in chapter 5.

Figures 3.15 through 3.28 contain all the results of the wall tap pressure tests and Table 3.5 gives additional information on the test conditions for each test series.

Table 3.5: Test Conditions and Measured Torque for Wall Tap Pressure Tests

Test Series	ω/ω_D	P_0 (atm)	$\dot{m}$ (kg/s)	T_Q (N·m)
1	1.0	2.21	3.19	18.21
2	1.0	2.21	3.14	18.48

Figures 3.15 through 3.26 are organized such that each page contains two figure each at the same station but one for test series 1 and the other for test series 2. Figure 3.27 for test series 1, and 3.28 for test series 2, are different from all the rest of the wall tap pressure figures in that they plot stations 4,5,6,7, and 9 on one graph for comparison. The repeatability in the results increases as one goes from station 4 to station 6 and then decreases dramatically at station 8 and then once again increases at station 9. Stations 6 and 7 are very repeatable when analyzed from both a trial to trial and a test series to test series point of view.

The pressure tap holes at station 4 are before the seal. One notices a perturbation in pressure at station 4 and this is seen in Figure 3.15 for test series 1 and in Figure 3.16 for test series 2. Once again, the magnitude and phase of these perturbations are used as an input for the theoretical model. It is shown in chapter 5 that the theory is sensitive to both pressure and velocity perturbations at the inlet to the shroud. It is also shown, that the theory predicts an increase in the cross force with these measured inlet perturbations as compared to no inlet perturbations whatsoever. Therefore, perturbations in pressure and velocity exist at the inlet and they do have an effect on the final theoretical result.[6] The pressure tap holes at station 5 are approximately over the first seal knife edge, which is at a location where static pressures are rapidly changing. This makes their interpretation difficult. Figure 3.17 and 3.18 show these results for test series 1 and 2 respectively. However, the pattern is still very similar to those observed for the unshrouded cases.[15]

Stations 6 and 7 are both inside the cavity of the shroud, 6 being near its center and 7 near its exit. The corresponding wall pressures are shown in Figures 3.19 and 3.20 for station 6 and Figures 3.21 and 3.22 for station 7. These show identical nonuniformity patterns, and each station's phase and magnitude are shown on one figure for better comparison. Figures 3.27 (test series 1) and 3.28 (test series 2) show the comparisons between stations 4,5,6,7 and 9 for trial 1. Compared to the distributions seen in these locations with no shroud [15], one notices a large increase in amplitude, by about a factor of two, and also a phase shift away from the region of maximum gap and towards the 90° location. This shift has the effect of further increasing the contribution of these pressure forces to the forward-whirling cross force component F_y.

Stations 8 and 9 are at the exit of the shroud. A recirculation region exist at the immediate exit of the shroud (station 8) because the shroud is in the flow field and acts

[6]See Chapter 5.

as a blunt body. This causes the wall tap pressure measurements at station 8 to be extremely noisy and unable to yield significant results. The results of station 8 for trials 1 and 2 are shown in Figures 3.23 and 3.24 respectively. However, station 9 is not as noisy as station 8 and this station shows the sinusoidal pattern, therefore,. a magnitude and phase can be extracted. Figures 3.25 and 3.26 show the results at station 9 for test series 1 and 2 respectively. From the curve fits through the seven trial points for both test series at station 9 an average of the magnitude and phase of the perturbation in pressure is used as an input to the theory in order to calculate the direct and cross forces. As in the case of the perturbation in pressure at the inlet to the seal, the perturbation in pressure at the exit has an effect on increasing the cross force in the theoretical calculations.

The total forces due to the gland pressure distribution can be calculated using equations (1.15), (1.16) and (3.4). The values for $m1$, $m2$ and $m3$ at station 6 for both test series 1 and 2 are listed in Appendix A. An average of these values for each test series is taken. The length of the land, l, is 13.63 mm (0.537 in) and the radius is R_s = 135 mm (5.297 in). For non-dimensionalization (Equations (1.17) & (1.18)), the torque is given in Table 3.5, the blade height, B_H is 16.6 mm (0.652 in), the mean radius, R_m is 125 mm (4.932 in) and the eccentricity e = 0.46 mm (18 mil). The results of these calculations are listed in Table 3.6 on the following page.

3.3 Velocity Probe Results (The Alford Effect)

In order to find the magnitude of the Alford effect the test section is instrumented with velocity probes, as described in section 2.4.2. At a given circumferential location these probes traverse radially to measure stator inlet and rotor exit velocities along the span of the turbine blades. Seven radial samples of velocities are taken at a given circumferential location. Wall tap pressure measurements are taken at the same time velocity measurements are taken, therefore, there are seven wall tap

Table 3.6: Results of Wall Tap Pressure Measurements

Test Series	F_x N (lbf) $\frac{\omega}{\omega_D}=1.0$	F_y N (lbf) $\frac{\omega}{\omega_D}=1.0$	k_{xx} lbf/mil $\frac{\omega}{\omega_D}=1.0$	k_{xy} lbf/mil $\frac{\omega}{\omega_D}=1.0$	β_x - $\frac{\omega}{\omega_D}=1.0$	β_y - $\frac{\omega}{\omega_D}=1.0$
1	-7.695 (-1.730)	11.321 (2.545)	-0.0961	0.141	-3.84	5.63
2	-8.278 (-1.861)	11.962 (2.689)	-0.103	0.149	-4.06	5.86
Average	-7.987 (-1.795)	11.642 (2.617)	-0.0998	0.145	- 3.95	5.75
Max. Diff.	7.58%	5.66%	7.58%	5.66%	5.85%	4.08%

pressure samples at a given circumferential position[7] and the test series for these velocity measurements are the same as in the wall tap pressure section.

A problem with velocity measurements in this shrouded turbine facility is that the turbine's shroud in not recessed and the velocity probes at the rotor's exit can only radially span approximately 25% of the turbine hub to casing distance closest to the wall. Most of this distance is occupied by the shroud, therefore, these probes are in the shroud's wake. As one might deduce, this gives unpredictable results.

The velocity measurements at station 8 yielded scattered results with no particular pattern. However, the survey at station 9, further downstream, did give valid results, and is shown in Figure 3.29. Here a 5-hole probe was used, which could not be inserted past the radial limit described above. Therefore, three readings (circle, square and diamond) are all at the radial limit closest to the hub and the last three readings (x, triangle and +) are at different radial locations closest to the casing. These last three depths (nearest the casing) are in the direct wake of the shroud, but since this station is three chord lengths downstream of the rotor, the wake is probably sufficiently diffused.

[7]See section 3.2

The lack of coincidence at the identical radial locations (circle, square and diamond) gives a measure of the data scatter. The under turning shown in Figure 3.29 is, in fact, greater than that seen in the unshrouded cases (see Song). A value of the direct and cross force cannot be determined from the existing velocity measurements because not enough information is known at other radial locations in order to make a good approximation of these values.

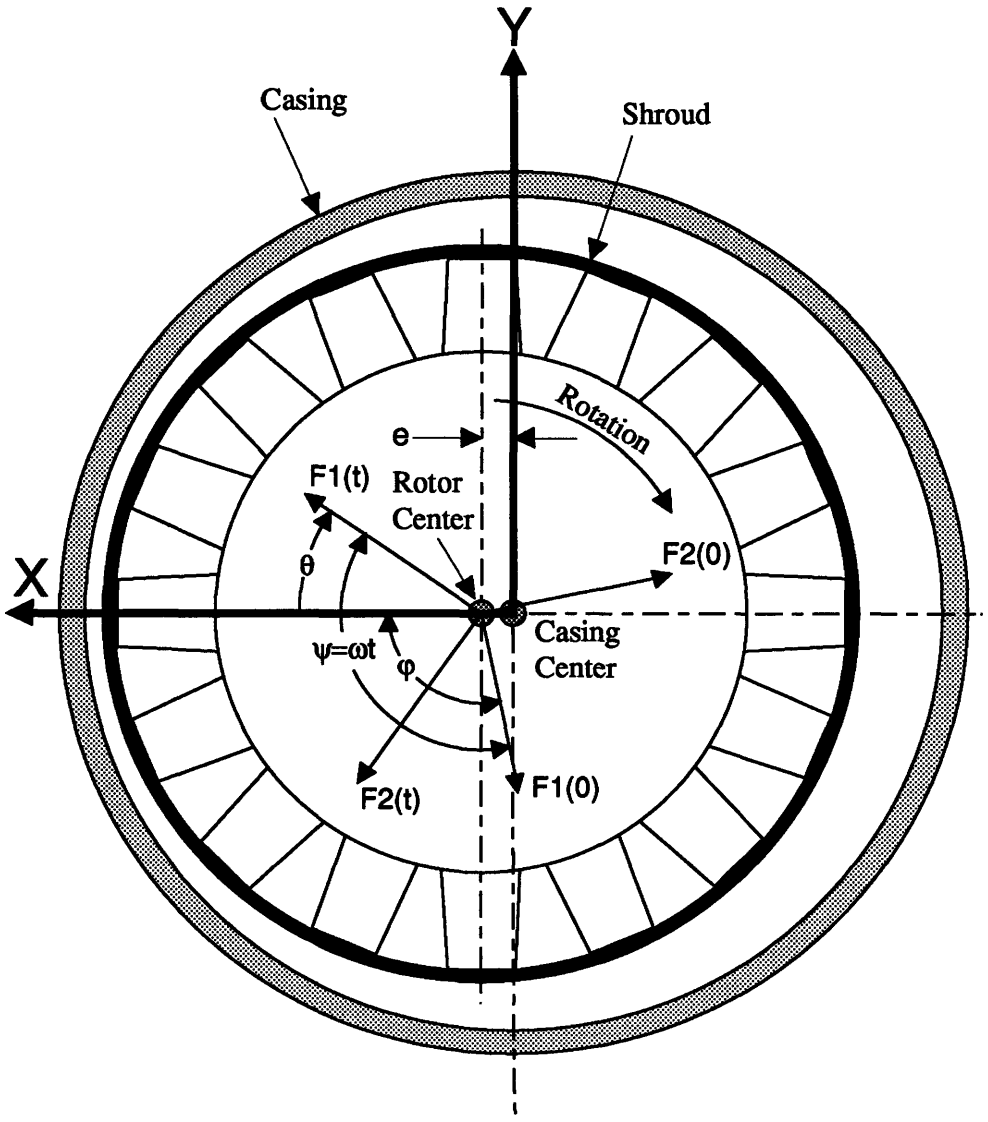

Figure 3.1: Data Reduction and Experimental Facility Coordinates. (View From Upstream) [13]

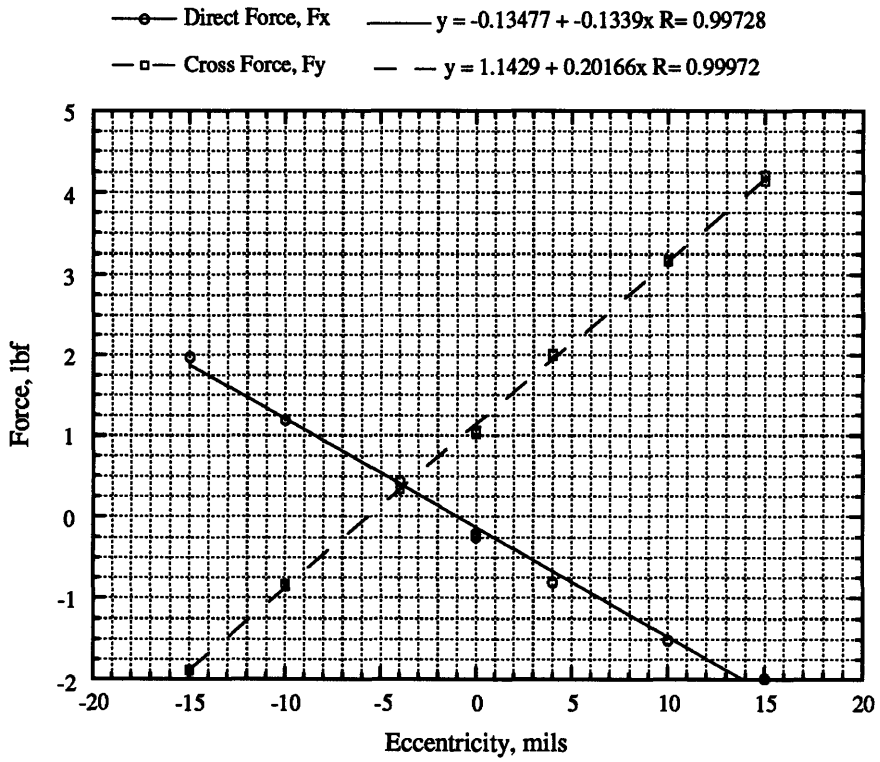

Figure 3.2: Test Series 1, P_0=2.21 atm. Off-design Speed at 2408 rpm ($\omega = 0.7\omega_D$).

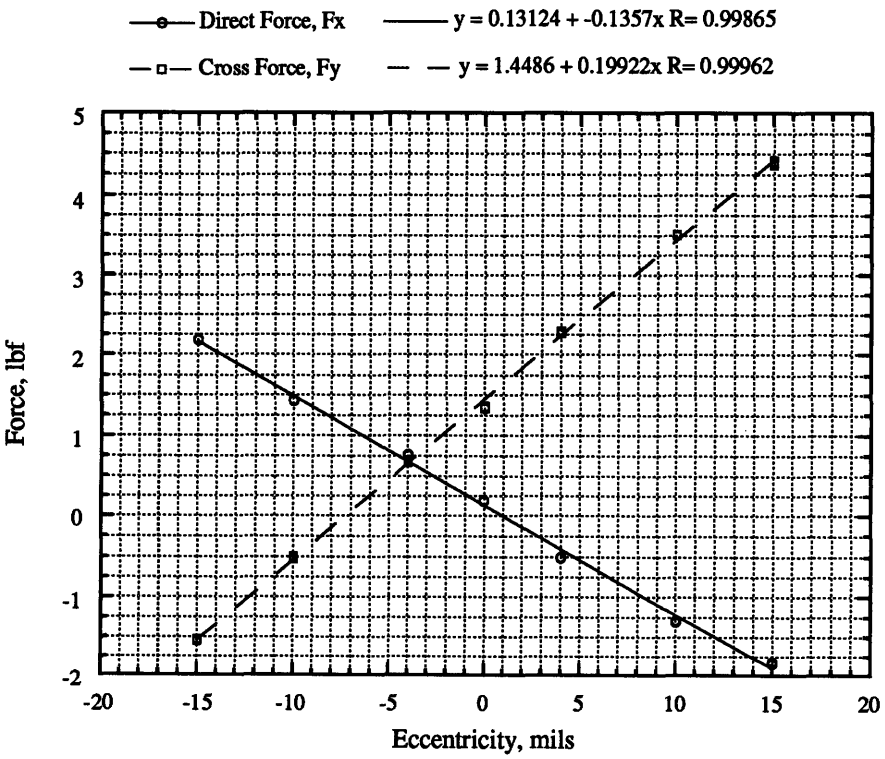

Figure 3.3: Test Series 3, P_0=2.21 atm. Off-design Speed at 2408 rpm ($\omega = 0.7\omega_D$).

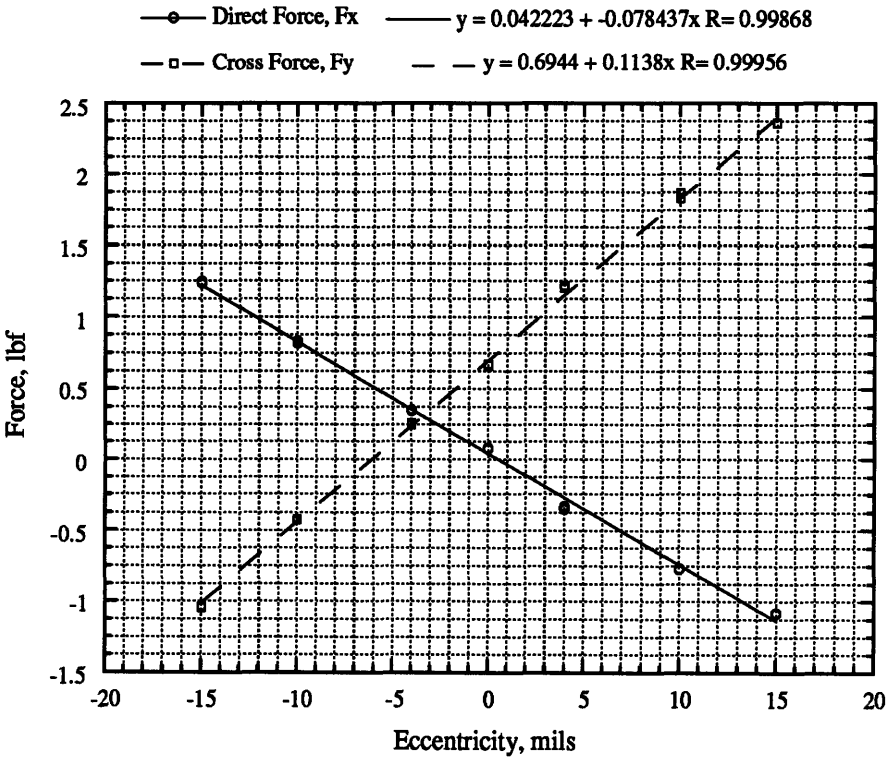

Figure 3.4: Test Series 2, P_0=1.25 atm. Off-design Speed at 2408 rpm ($\omega = 0.7\omega_D$).

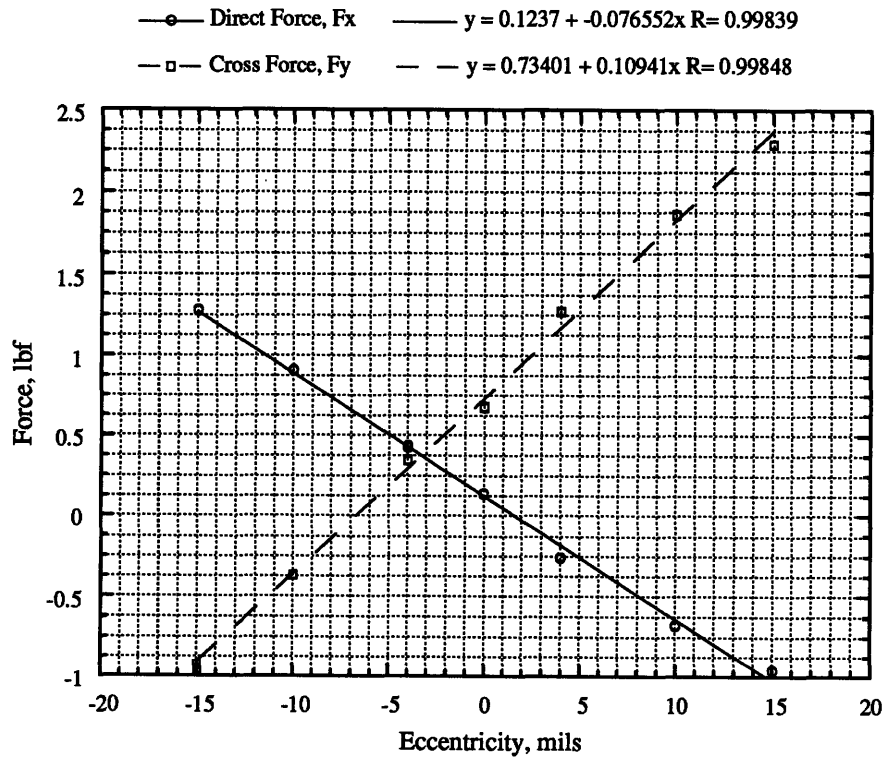

Figure 3.5: Test Series 4, P_0=1.24 atm. Off-design Speed at 2408 rpm ($\omega = 0.7\omega_D$).

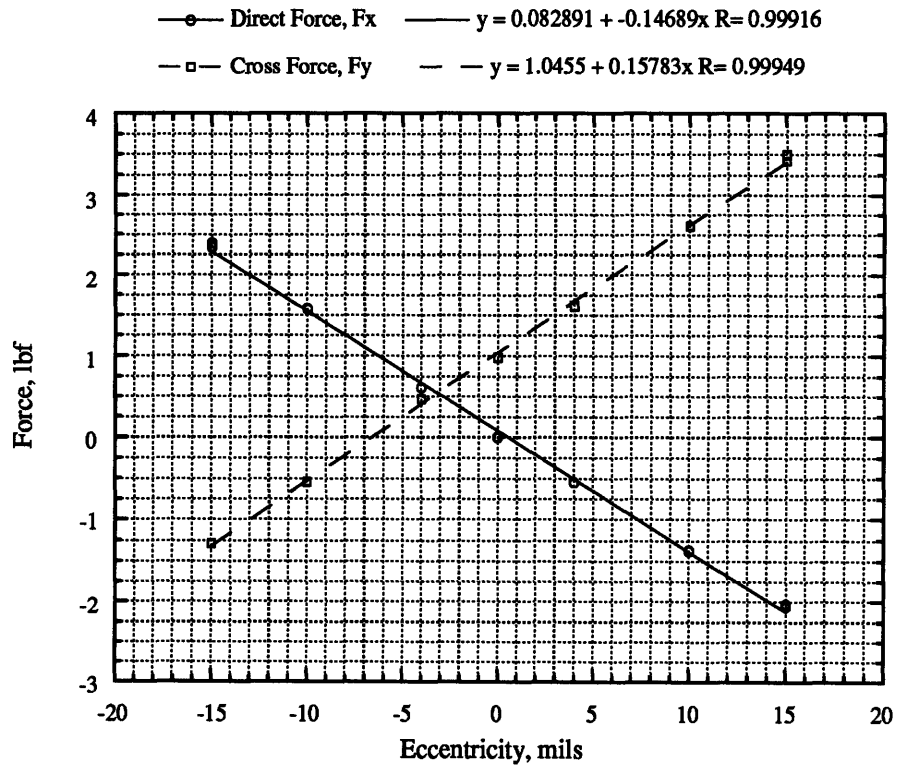

Figure 3.6: Test Series 1, P_0=2.21 atm. Design Speed at 3440 rpm ($\omega = 1.0\omega_D$).

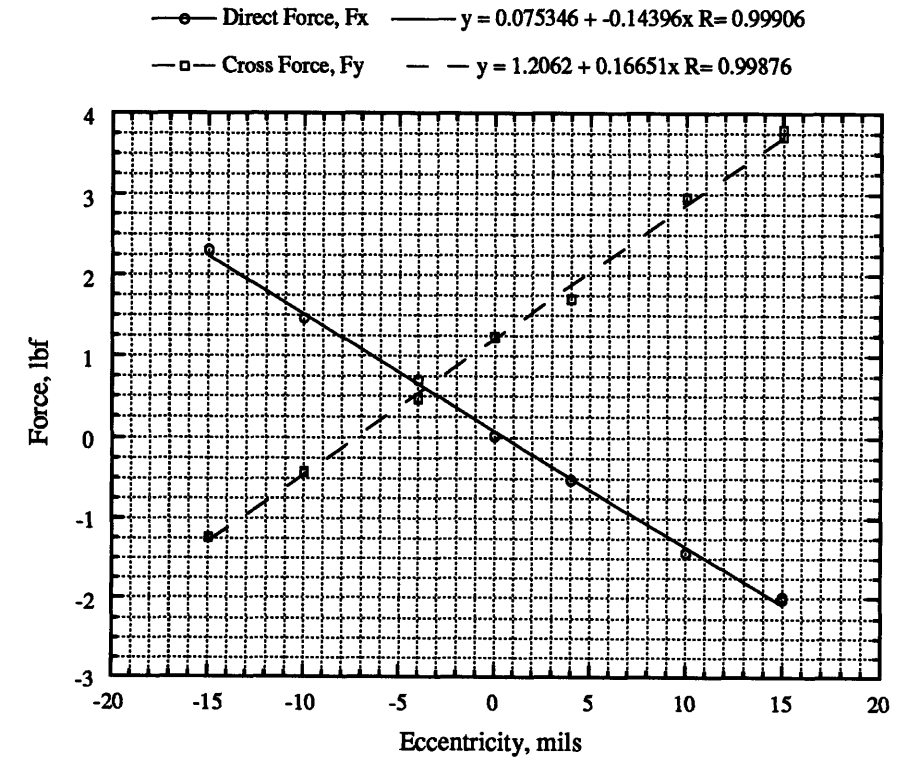

Figure 3.7: Test Series 3, P_0=2.21 atm. Design Speed at 3440 rpm ($\omega = 1.0\omega_D$).

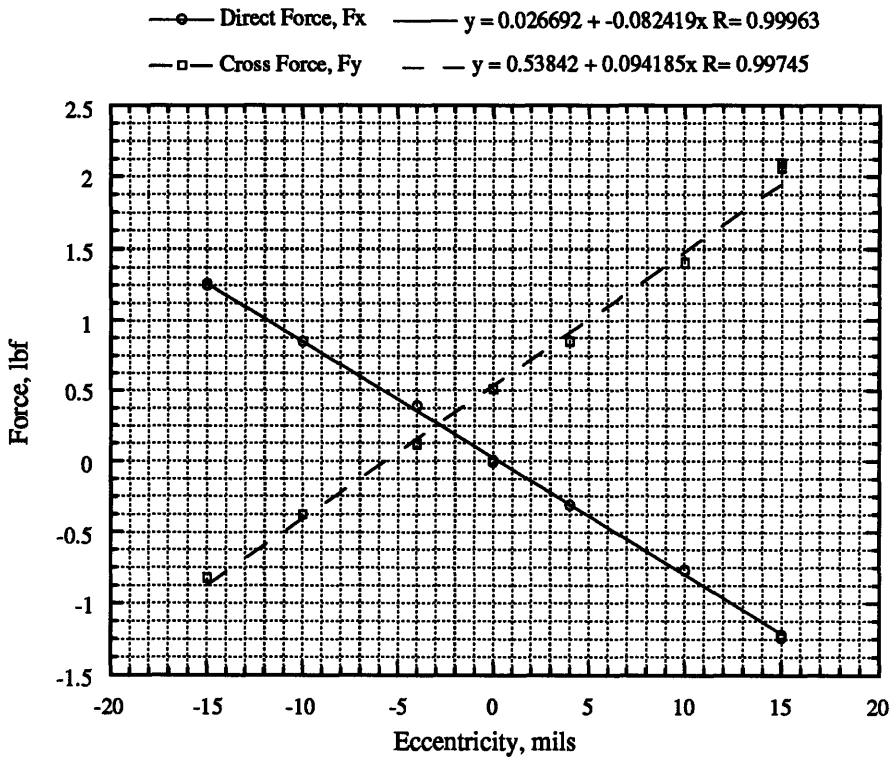

Figure 3.8: Test Series 2, P_0=1.24 atm. Design Speed at 3440 rpm ($\omega = 1.0\omega_D$).

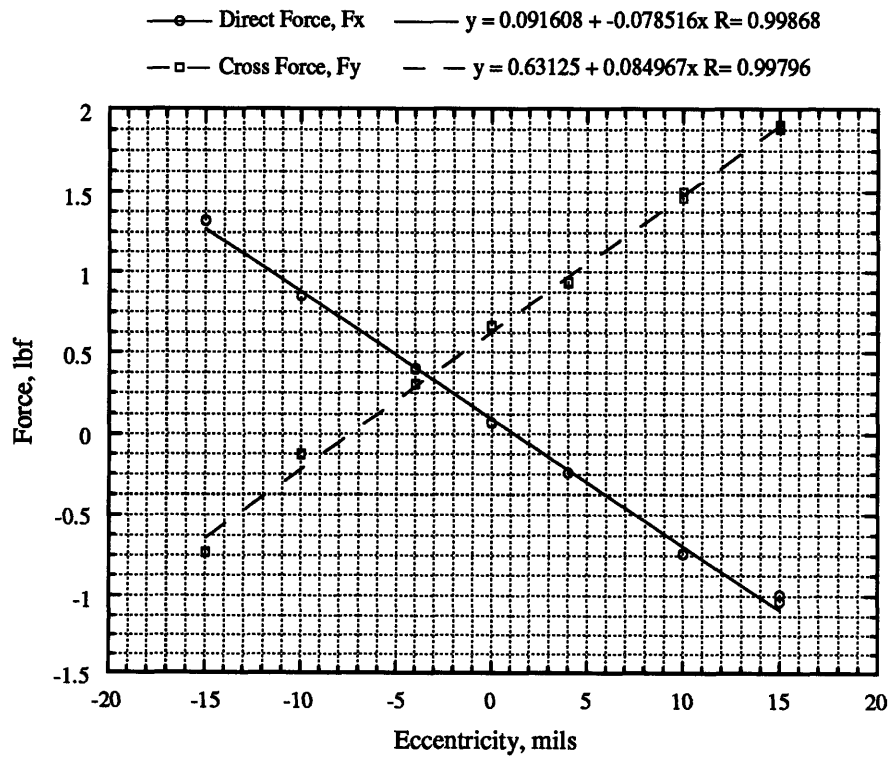

Figure 3.9: Test Series 4, P_0=1.24 atm. Design Speed at 3440 rpm ($\omega = 1.0\omega_D$).

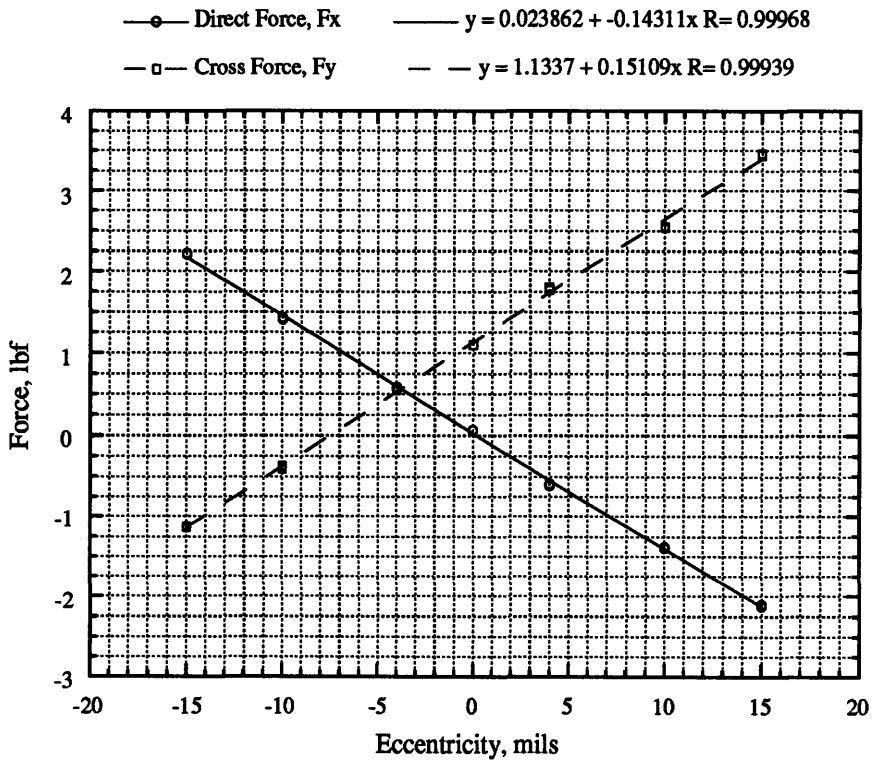

Figure 3.10: Test Series 1, P_0=2.21 atm. Off-Design Speed at 3784 rpm ($\omega = 1.1\omega_D$).

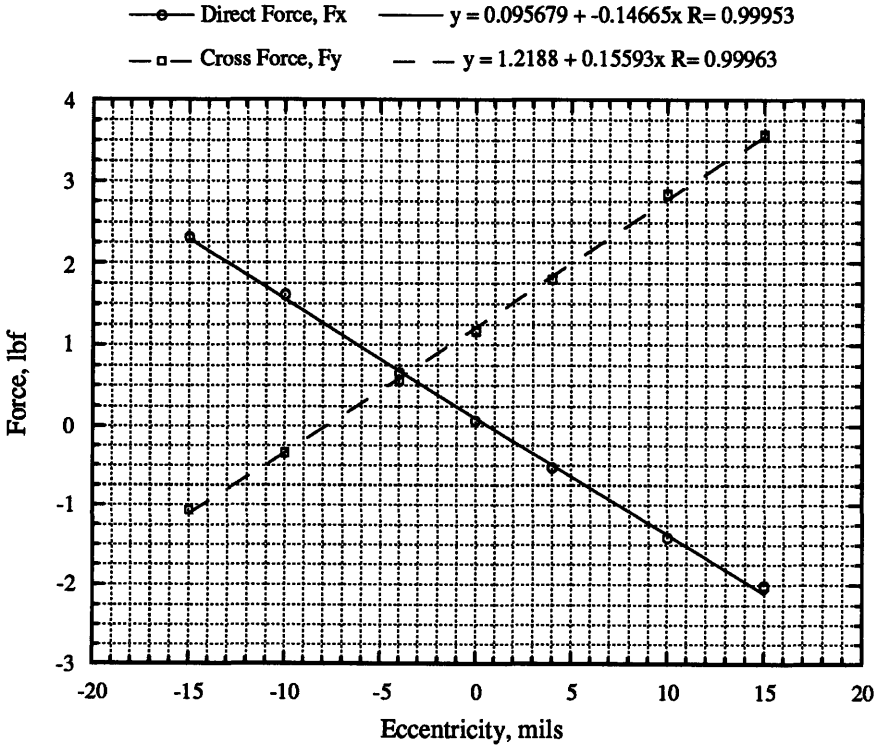

Figure 3.11: Test Series 3, P_0=2.21 atm. Off-Design Speed at 3784 rpm ($\omega = 1.1\omega_D$).

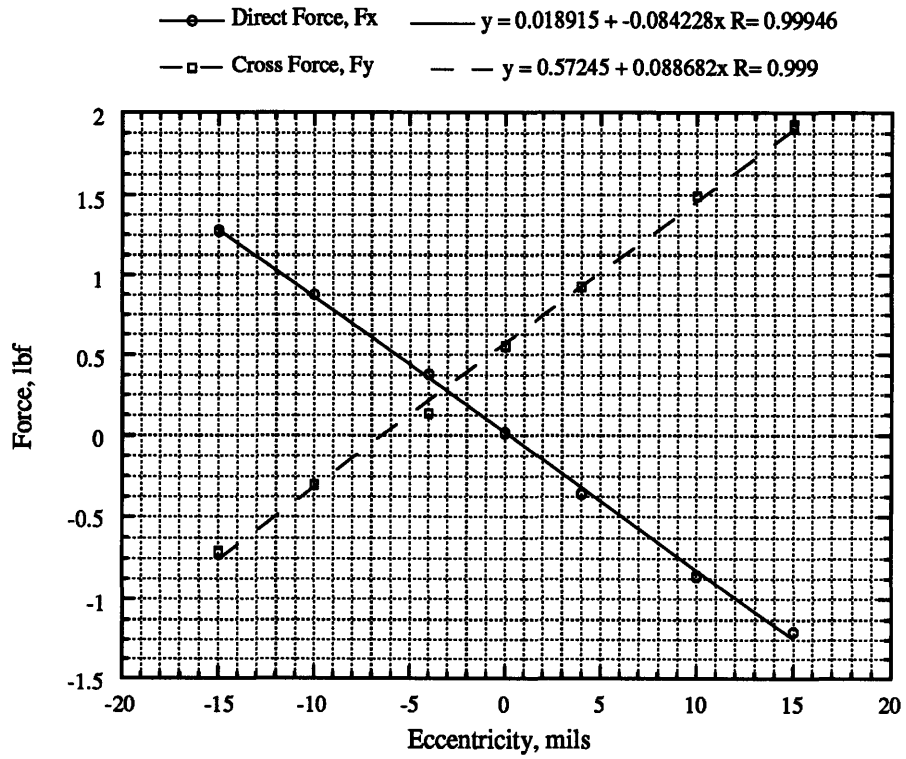

Figure 3.12: Test Series 2, P_0=1.24 atm. Off-Design Speed at 3784 rpm ($\omega = 1.1\omega_D$).

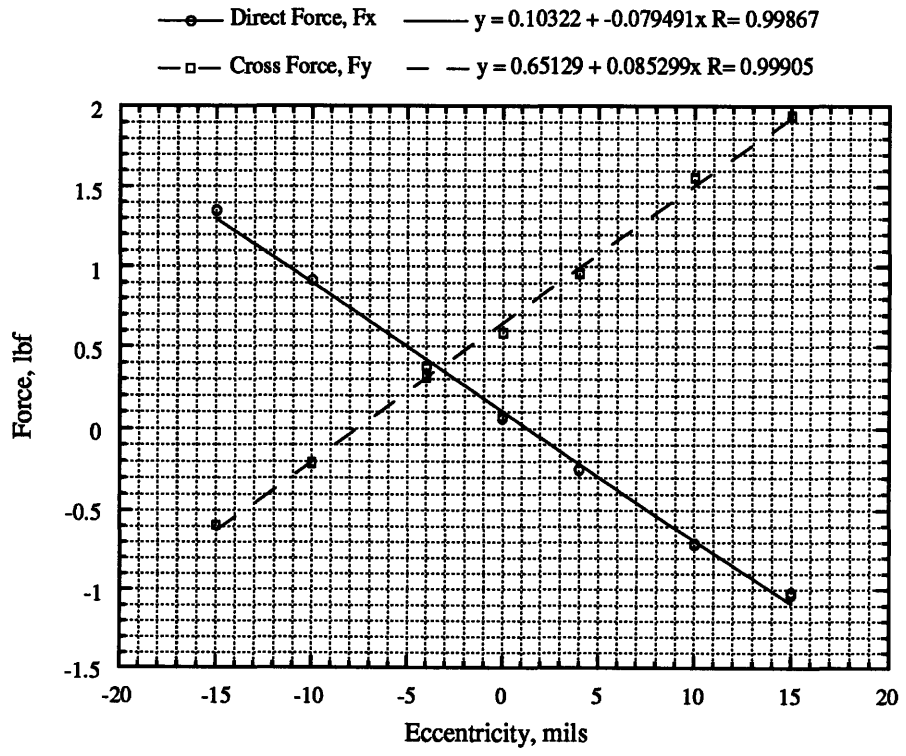

Figure 3.13: Test Series 4, P_0=1.24 atm. Off-Design Speed at 3784 rpm ($\omega = 1.1\omega_D$).

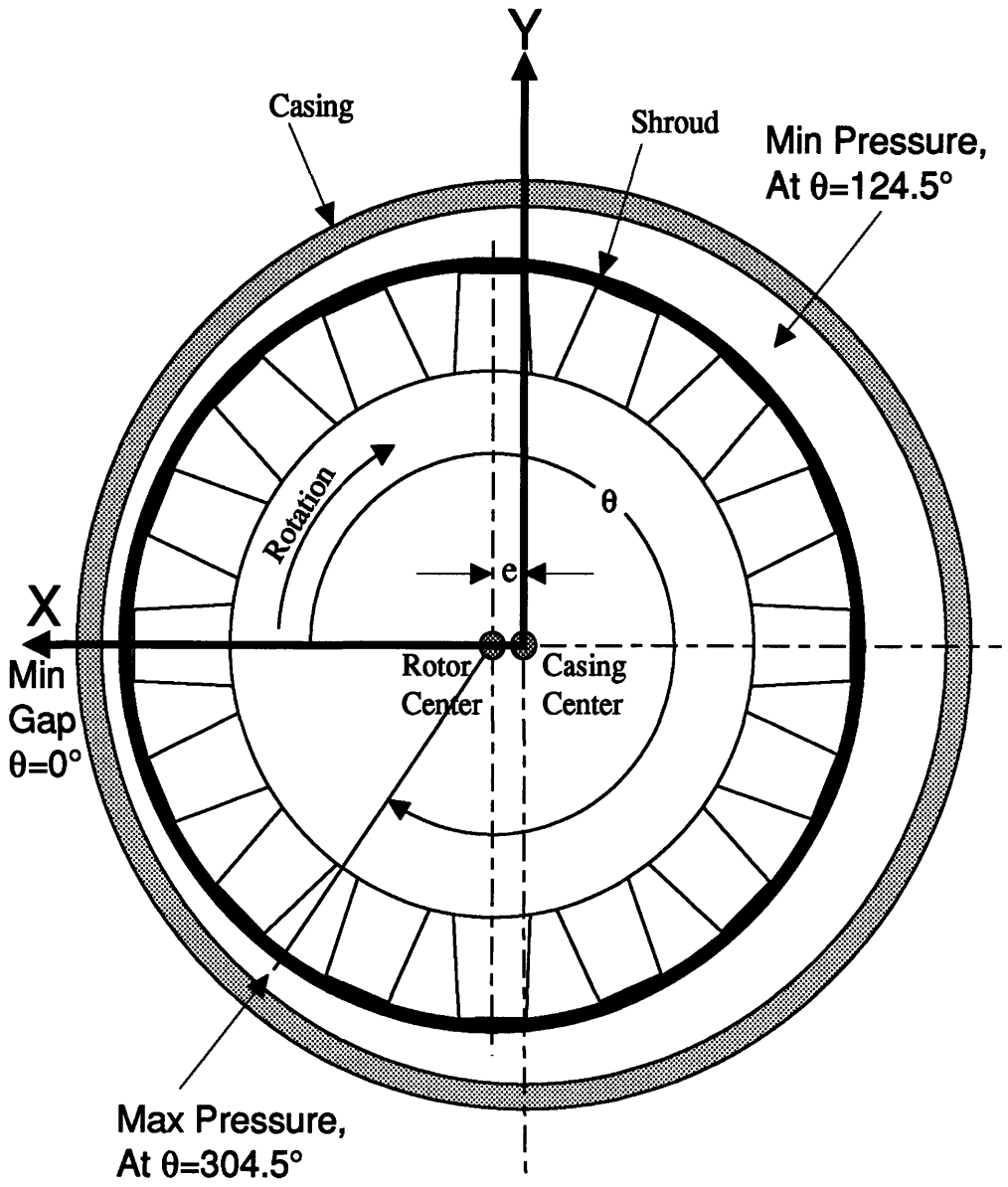

Figure 3.14: Angular Convention and Location of Minimum and Maximum Pressure as Measured at Station 6. (View from Upstream)

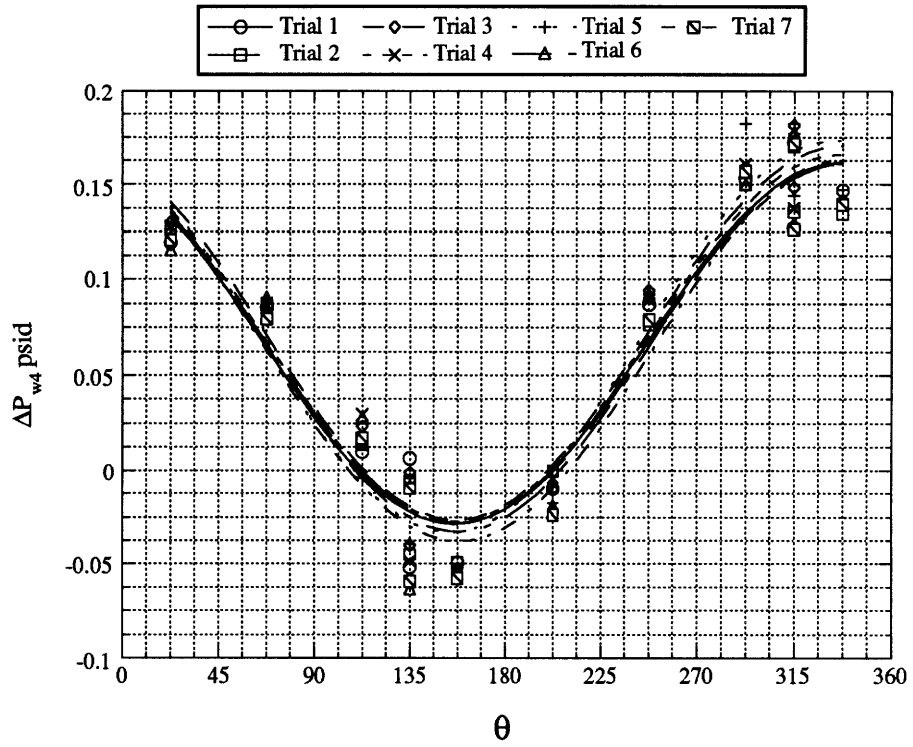

Figure 3.15: Test Series 1, Wall Tap Pressure Distribution at Station 4, Between Stator and Rotor at the Entrance to the Shroud. P=2.21 atm, Eccentricity = 18 mils = 0.46 mm.

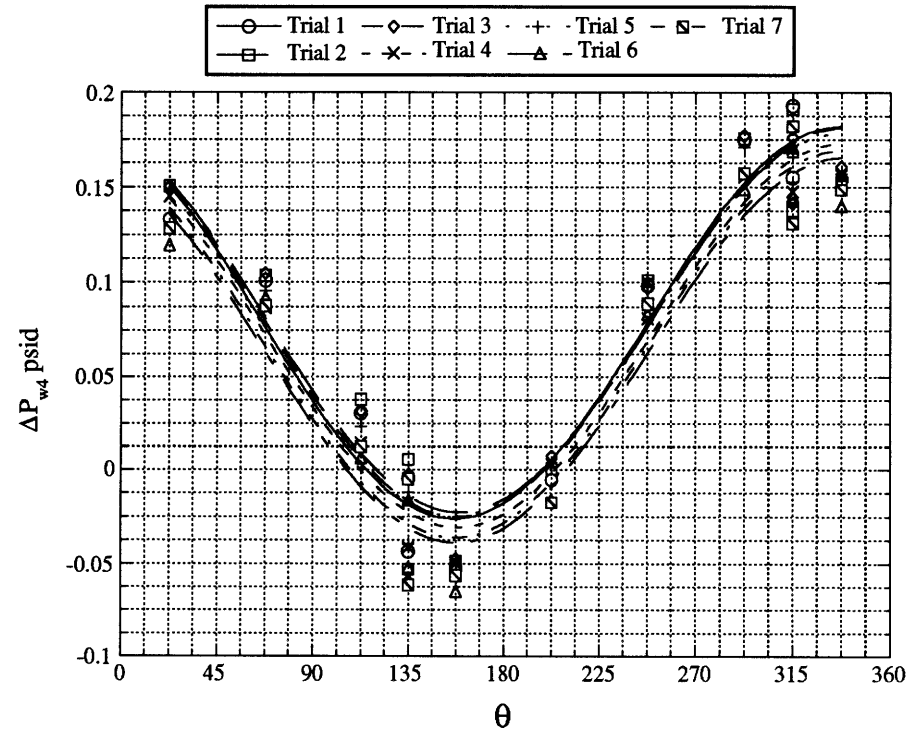

Figure 3.16: Test Series 2, Wall Tap Pressure Distribution at Station 4, Between Stator and Rotor, at the Entrance to the Shroud. P=2.21 atm, Eccentricity = 18 mils = 0.46 mm.

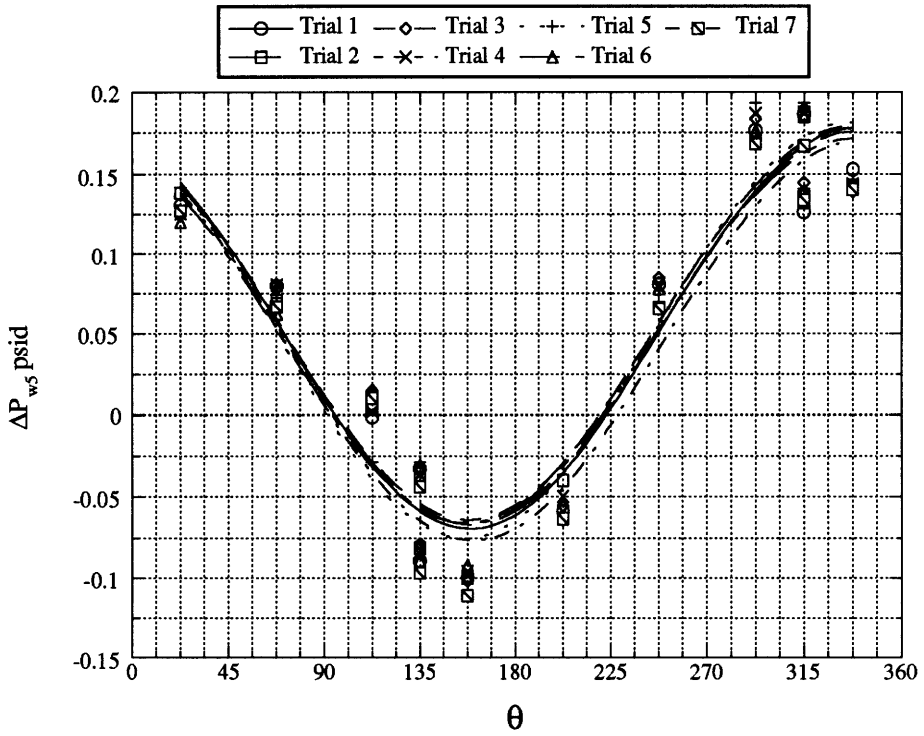

Figure 3.17: Test Series 1, Wall Tap Pressure Distribution at Station 5, Over the First Seal Knife. P=2.21 atm, Eccentricity = 18 mils = 0.46 mm.

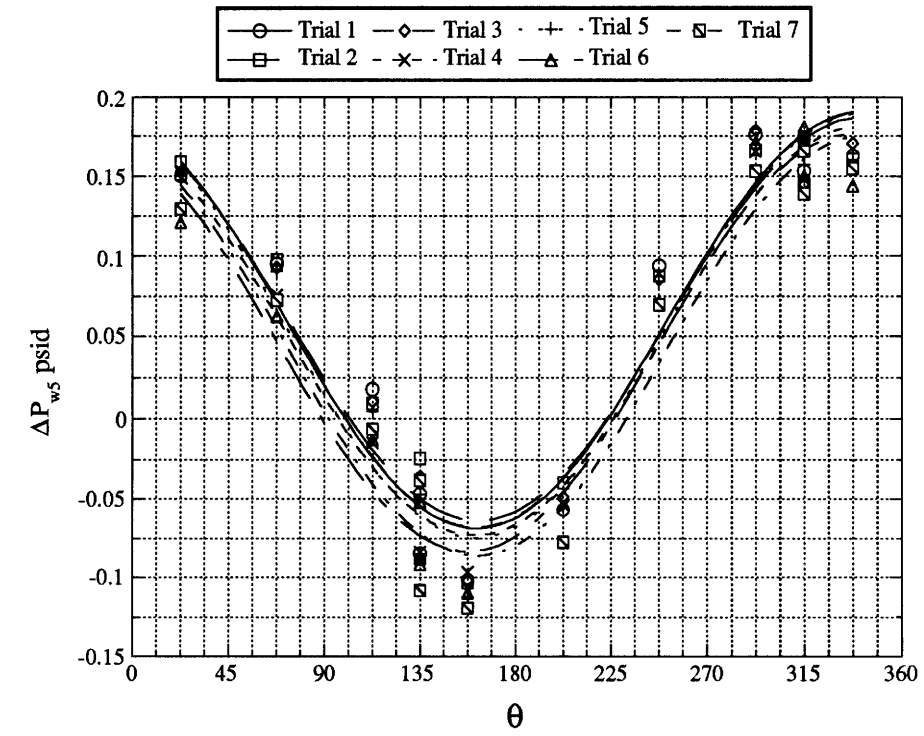

Figure 3.18: Test Series 2, Wall Tap Pressure Distribution at Station 5, Over the First Seal Knife. P=2.21 atm, Eccentricity = 18 mils = 0.46 mm.

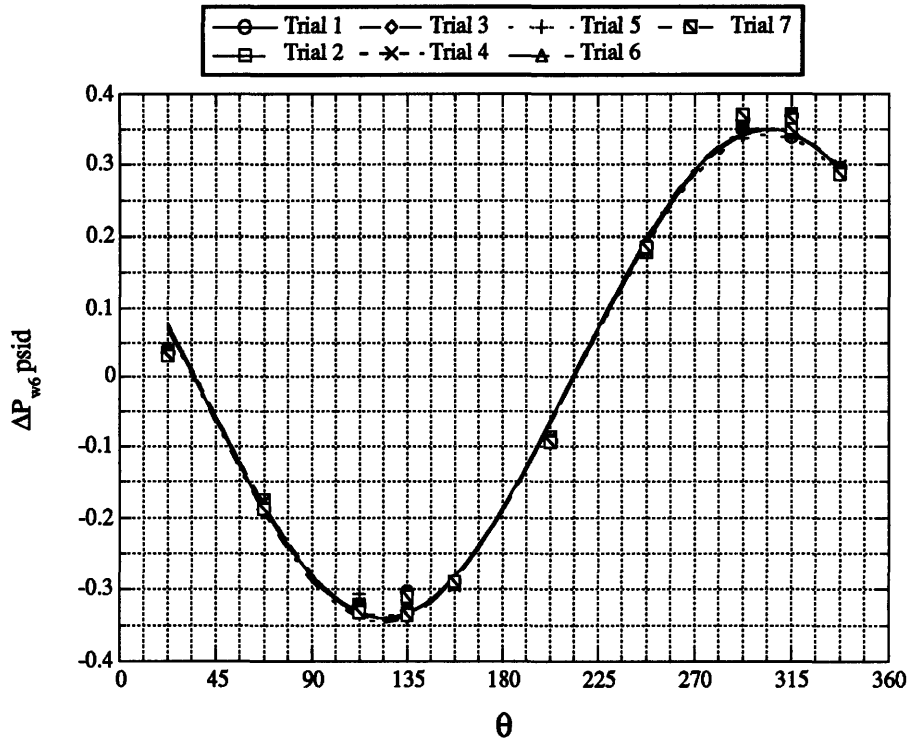

Figure 3.19: Test Series 1. Wall Tap Pressure Distribution in the Center of the Shroud Labyrinth Seal. Station 6, P=2.21 atm, Eccentricity = 18 mils = 0.46 mm.

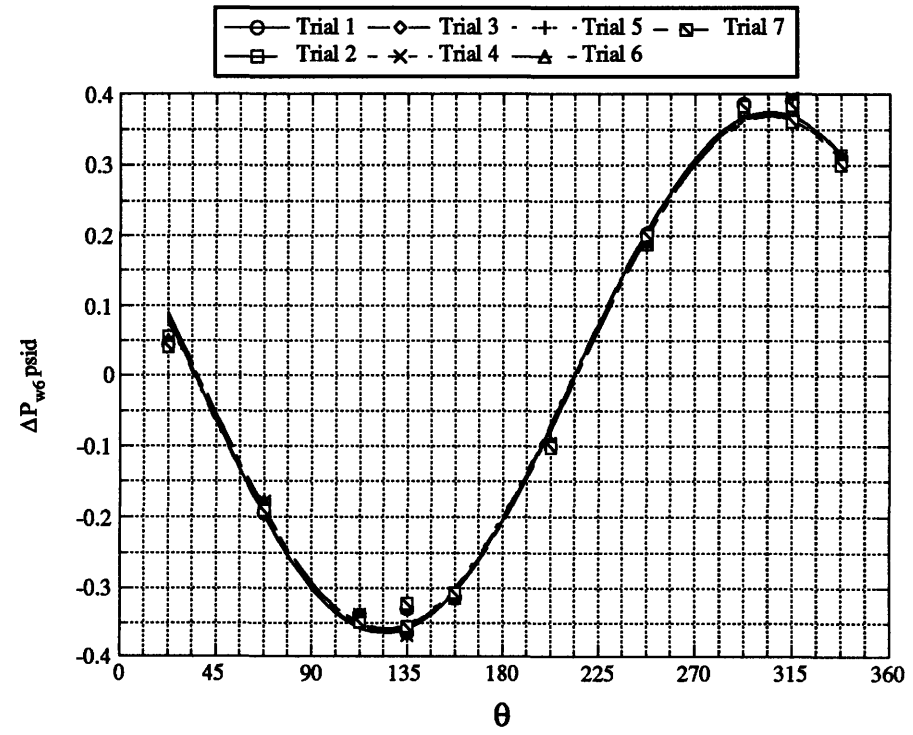

Figure 3.20: Test Series 2. Wall Tap Pressure Distribution in the Center of the Shroud Labyrinth Seal. Station 6, P=2.21 atm, Eccentricity = 18 mils = 0.46 mm.

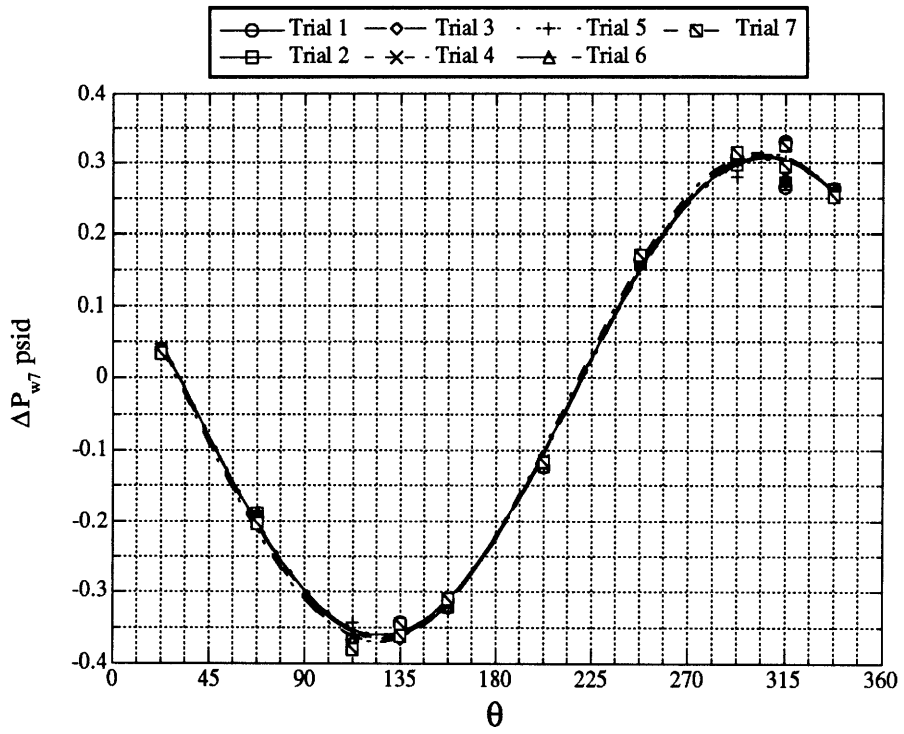

Figure 3.21: Test Series 1. Wall Tap Pressure Distribution at Station 7, Near the Exit of the Shroud Seal, However, Still Within the Shroud Cavity. P=2.21 atm, Eccentricity = 18 mils = 0.46 mm.

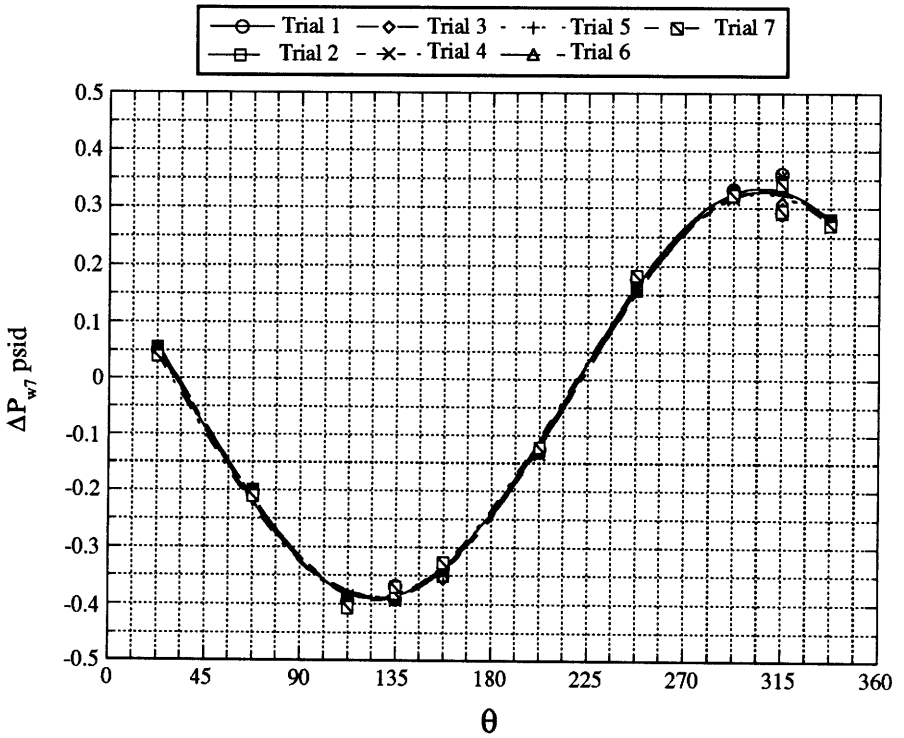

Figure 3.22: Test Series 2. Wall Tap Pressure Distribution at Station 7, Near the Exit of the Shroud Seal, However, Still Within the Shroud Cavity. P=2.21 atm, Eccentricity = 18 mils = 0.46 mm.

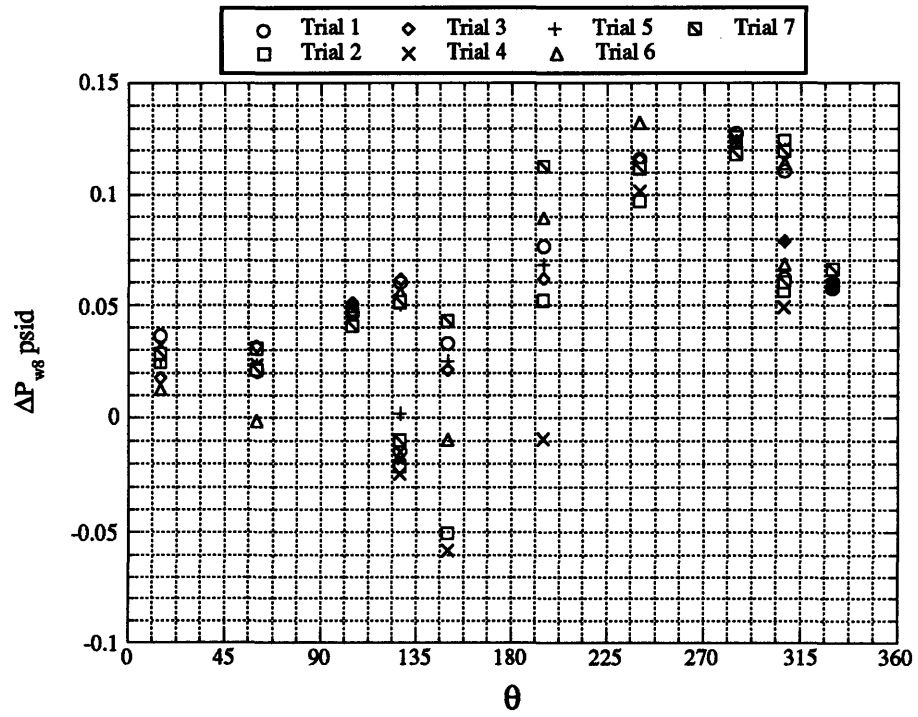

Figure 3.23: Test Series 1. Wall Tap Pressure Distribution at Station 8, at the Exit of the Shroud Seal (Past the Second Sealing Knife Downstream). P=2.21 atm, Eccentricity = 18 mils = 0.46 mm.

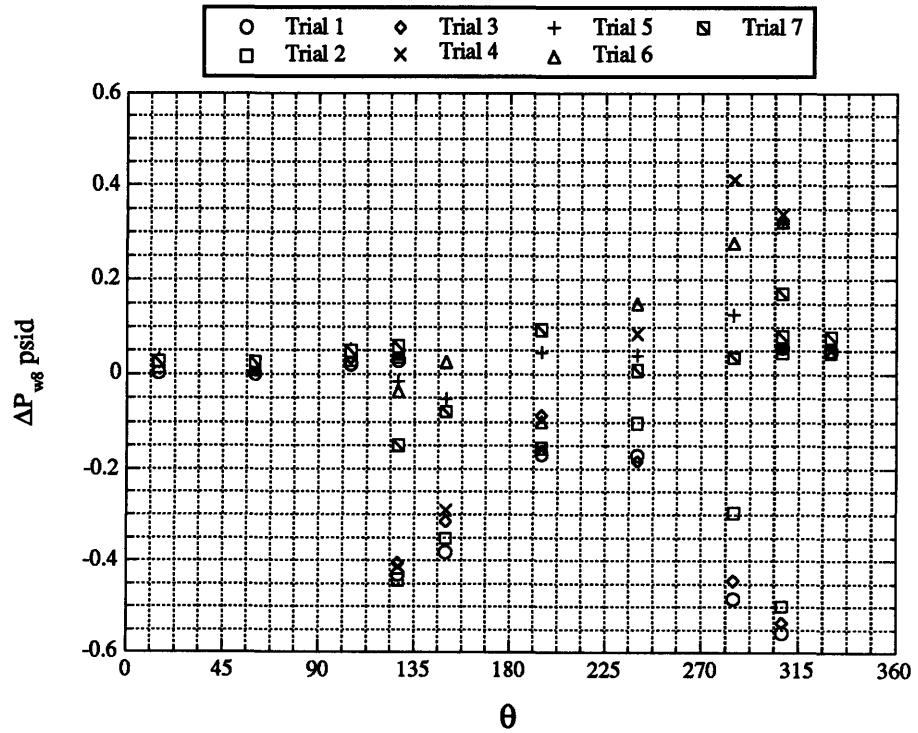

Figure 3.24: Test Series 2. Wall Tap Pressure Distribution at Station 8, at the Exit of the Shroud Seal (Past the Second Sealing Knife Downstream). P=2.21 atm, Eccentricity = 18 mils = 0.46 mm.

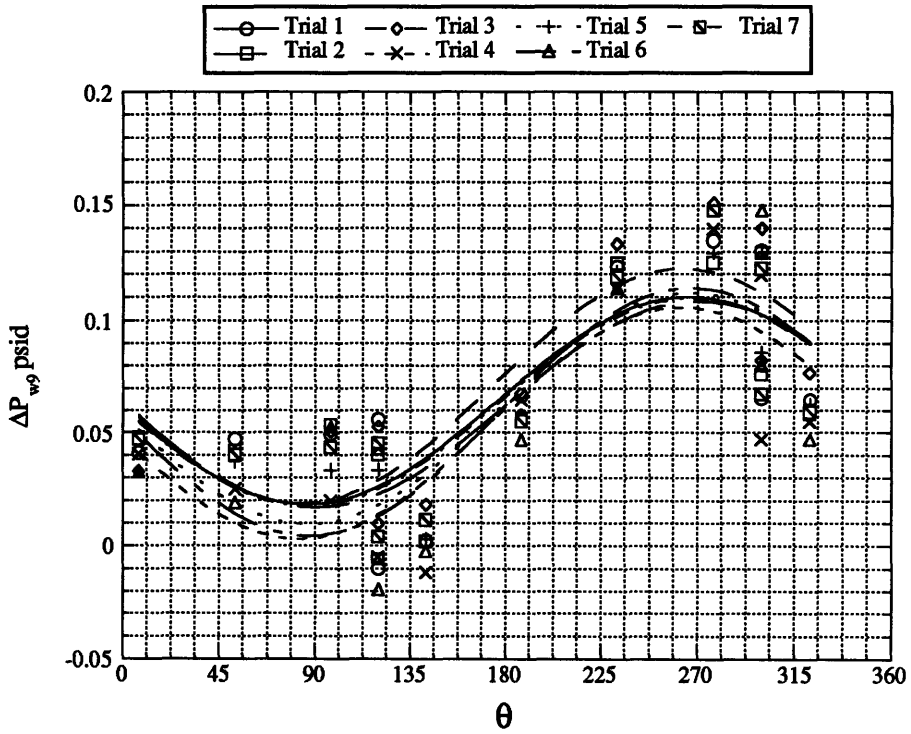

Figure 3.25: Test Series 1. Wall Tap Pressure Distribution at Station 9. Exit of the Shroud Seal and Past Station 8. (Past Second Sealing Knife Downstream). P=2.21 atm, Eccentricity = 18 mils = 0.46 mm.

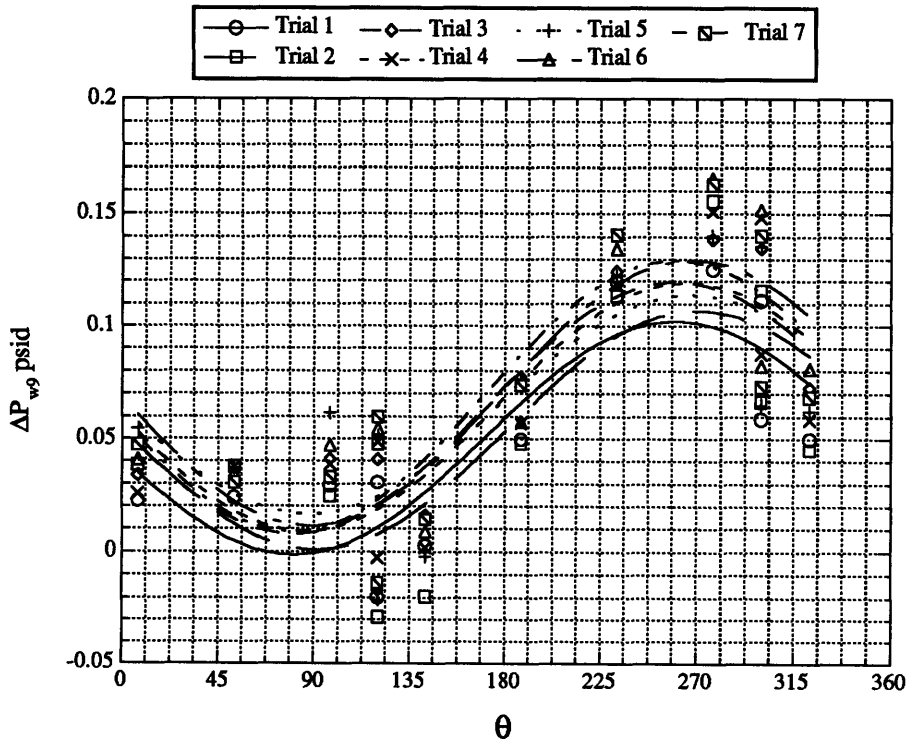

Figure 3.26: Test Series 2. Wall Tap Pressure Distribution at Station 9. Exit of the Shroud Seal and Past Station 8. (Past Second Sealing Knife Downstream). P=2.21 atm, Eccentricity = 18 mils = 0.46 mm.

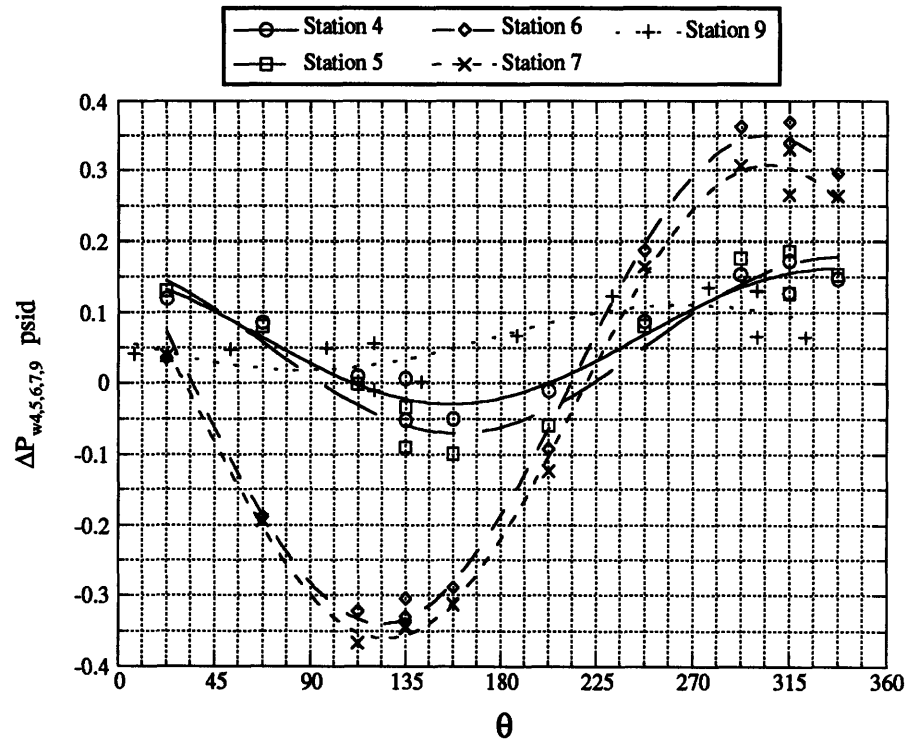

Figure 3.27: Test Series 1. Wall Tap Pressure Distribution at Stations 4,5,6,7 and 9. Trial 1 Data for the Five Stations Plotted for Cross Comparison. P=2.21 atm, Eccentricity = 18 mils = 0.46 mm.

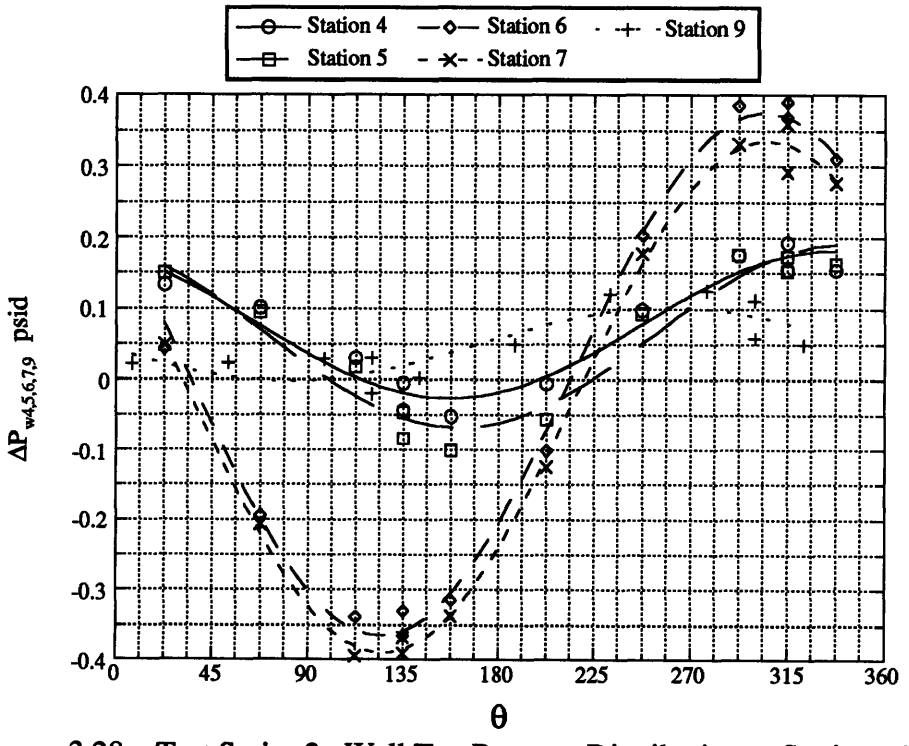

Figure 3.28: Test Series 2. Wall Tap Pressure Distribution at Stations 4,5,6,7 and 9. Trial 1 Data for the Five Stations Plotted for Cross Comparison. P=2.21 atm, Eccentricity = 18 mils = 0.46 mm.

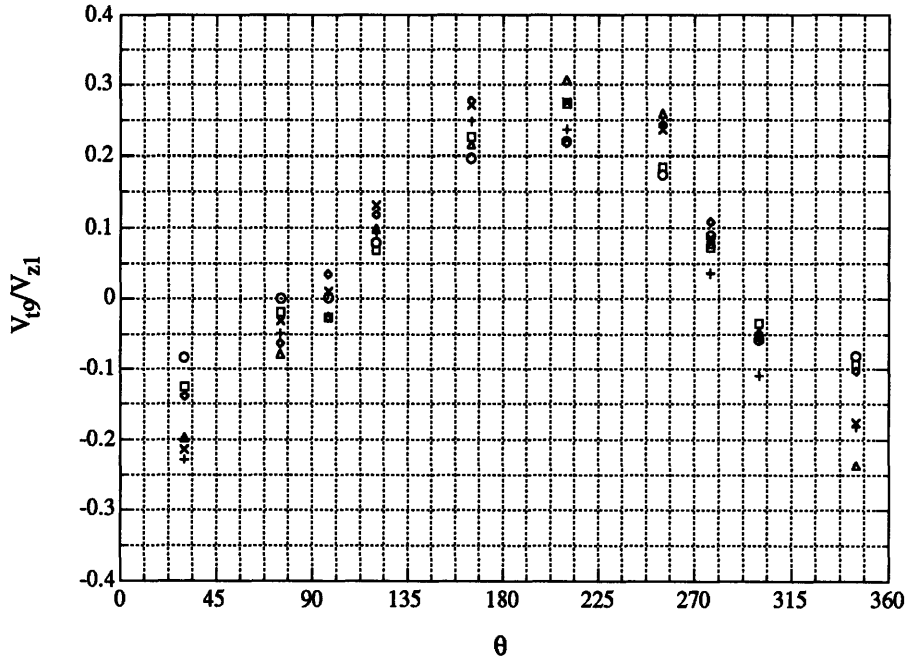

Figure 3.29: Tangential Velocities at Station 9. The Circle, Square and Diamond Data Points are all Nearest the Core at r/H=0.76. The X, Triangle and + are at Different Radial Locations Closest to the Wall in the Wake of the Shroud. Test Series 2.

Chapter 4

The Analytical Model

4.1 Kostyuk-Iwatsubo-Millsaps Model

To completely model the flow through a rotating, whirling shroud as accurately as possible the full Navier-Stokes equations should be used. However, a closed form analytical solution of these equations is impossible. A numerical solution would be extremely expensive since the model would be required to perform parametric studies. Therefore, in this chapter a simplified model is developed which incorporates the dominant flow conditions and pertinent geometric parameters. Through this simplified analytical model physical insight is easier obtained than through more comprehensive treatments. Note that this model assumes flow only through the shrouded region and the flow through the rotor is ignored. Therefore, this model predicts the pressure nonuniformity within the cavity of the shroud but says nothing about the Alford effect caused by the variation of blade forces around the circumference of the rotor blades. The results of this theoretical model are compared directly to the wall tap pressure results.

The model is based on the work of Kostyuk [12], Iwatsubo[9] and Millsaps [16,17]. Kostyuk's lumped parameter model simplifies the governing equations such that the flow in the axial direction is coupled to the one dimensional continuity and momentum equations in the circumferential direction. Since the fluid variations around the annular cavity is what gives rise to the asymmetric pressure distribution the state variables within the land of the shroud are a function of angle and time only and the average value of all state variables is used at each section. Iwatsubo's model took

Kostyuk's model one step further and generalized it for area variations within the land due to the shaft's whirling motion. Millsaps' model took Iwatsubo's model and expanded it to include a contraction coefficient and a "carry-over factor" to better explain the flow over the sealing knives. In Millsaps' Doctoral work, he also included upstream nonuniformity, which was calculated by an extension of the same type of modeling used in the gland. Since, Millsaps work deals only with a shroud without any rotor blading, he was able to solve for these upstream nonuniformities. However, the shroud in this work has different and more difficult inlet conditions to model due to the rotor. Therefore, instead of solving for the inlet nonuniformities these inlet (as well as outlet) conditions will be taken from experimental results. The expansion incorporated here, therefore, has the ability to accept input for the magnitude and phase of the pressure nonuniformity upstream and downstream of the shrouded rotor. It will be shown that the magnitude and phase of these pressure nonuniformities greatly affects the solution for the pressure nonuniformity within the shroud cavity. Please note that, Millsaps Ph.D thesis [17] was the foundation and guide used in presenting the expanded theoretical work located in this chapter.

4.2 Derivation of the Governing Equations

The governing equations for a shroud containing two sealing knives which surround a cavity (gland) are derived in this section. The assumptions presented in the previous section along with the following nine assumptions provide a foundation for building the set of governing equations. Most of these assumptions are the same as that presented by Millsaps [17] and those which are the same are written as he presents them.

1) The inlet total pressure, temperature and swirl velocity are prescribed along with the downstream pressure.

2) The working fluid is and ideal gas and is calorically perfect.

$$P = \rho RT$$

$$dh = C_p dT$$

3) The flow through the seal is adiabatic.

4) Small changes within the seal gland in the azimuthal direction are assumed to occur isentropically.

5) The seal moves as a rigid body. There is no elastic deformation.

6) The seal moves in a whirling motion parallel to the rotation axis of the machine. There is no tilting.

7) The acoustic resonant frequency of the seal cavity is much greater than the whirling frequency: $\Omega << \omega_a = \frac{\sqrt{\gamma RT}}{2\pi R_s}$

8) The viscous shear stresses exerted on the fluid inside the gland, by both rotor and stator, follow a Darcy friction law.

$$\tau = \tfrac{1}{8}\lambda\rho\bar{V}_{rel}^2$$

where τ is the shear stress, λ the friction factor, ρ the density and $\bar{V}_{rel}$ is the relative velocity between the average fluid core flow and the nearest solid surface.

9) The reduced frequency, based on seal pitch, axial through flow velocity and whirling frequency, is much less than one.

The next step in deriving the governing equations is to define the geometry and the variables that act within this geometry. Figure 4.1 is a cutaway section of the shroud and shows the cylindrical coordinate system used along with the pertinent flow quantities. The pressure and velocity upstream of the rotor is a function of circumference and time and is given by P_i and V_i respectively. Between the sealing knives one has the cavity or, as its been called in the previous chapters, the gland. In the gland the unknown pressure, P, density, ρ, and velocity, V, are functions of azimuth and time. The solution to the governing equations gives this pressure and velocity distribution. The nonuniform exit pressure is given by P_o and the temperature is assumed to be constant everywhere, therefore, it has no subscripts and is given by T.. The rotational frequency of the shaft is given by ω.

Figure 4.2 incorporates the flow conditions into the entire system, defines the geometry of the system and illustrates the motion of the shroud with respect to fixed coordinates. First, the side view of the shroud illustrates the mass flow rate per unit circumferential length into, q_1, and out of, q_2, the cavity of the shroud. The radius of the shroud from the center line to the tip of the sealing knives is given by R_s and the seal clearances into and of the shroud are given by δ_1 and δ_2 respectively. The axial view illustrates the kinematics of the system. Once again, the shaft frequency is given by ω while the whirl angular frequency is Ω. This whirling motion amplitude is described by r.

The mass influx into the seal chamber is derived first. The description of the flow rate is at the minimum area at the inlet which is over the first sealing knife. If one assumes constant density and velocity across this incoming jet equation (4.1) results:

$$\dot{m} = \rho_1 A_1 w_1 \tag{4.1}$$

The density, ρ_1, is taken to be the density at the first sealing knife contraction. In order to find this density in terms of the densities at the inlet and within the cavity of the shroud an average of these later two densities is taken. This method approximates the fully compressible relations and a maximum of a three percent error in the mass flow rate is incurred using this method. The axial velocity is given by w_1. Since this mass flow rate is described at the jet location the area A_1 is an effective area. This effective area is defined as the actual area multiplied by a contraction coefficient, C_c. The ratio of the minimum area of the jet to the area at the sealing knife is this contraction coefficient. Therefore, this mass flow rate over the inlet sealing knife may now be represented as a mass flow rate per unit circumferential area in the following form:

$$q_1 = \rho_1 \delta_1 C_c w_1 \tag{4.2}$$

The existence of C_c in equation (4.2) is a simplification from a more complicated expression of the axial mass flow rate into the cavity of the shroud. The contraction coefficient is replaced with the flow coefficient, μ, for the axial flow rate at the exit of the seal. This flow coefficient contains more information than the contraction coefficient in that it takes into account the magnitude of the impinging jet that is created by the first seal knife. The flow coefficient, μ is defined as the ratio of the actual flow through a seal divided by the ideal mass flow. The contraction coefficient multiplied by a kinetic energy carry-over factor, β, gives the flow coefficient as shown by the following equation.

$$\mu = C_c \beta \tag{4.3}$$

The first sealing knife has no carry over effect, therefore, the flow coefficient and the contraction coefficient are the same (or $\beta = 1$). The kinetic energy carry-over factor has a value other than one at the second sealing knife because of the impinging jet created by the first sealing knife. From experiment, it has been determined that the contraction coefficient has a value of 0.650. For further discussion of the contraction coefficient and its dependence on geometry please see Appendix B in Millsaps doctoral work [17].

The next step is to represent the axial flow rate and the average density in terms of the pressure at the inlet to the shroud, the pressure within the cavity of the shroud and the temperature of the system. To accomplish the first task one may apply Bernoulli's equation along a stream line from the inlet to the shroud into the cavity of the shroud. Using the stagnation pressure at the inlet, the static pressure in the cavity and then solving this equation for the axial velocity one obtains equation (4.4).

$$w_1 = \sqrt{\frac{2(P_i - P)}{\rho_1}} \tag{4.4}$$

The density of the fluid over the first sealing knife is taken as the average of the densities before the seal and within the cavity of the seal. Taking this average and applying the ideal gas equation (4.5) results.

$$\rho_1 = \frac{\rho_i + \rho}{2} = \frac{P_i + P}{2RT} \tag{4.5}$$

Equations (4.4) and (4.5) are substituted into equation (4.2) in order to derive the equation governing the influx of mass into the seal.

$$q_1 = \frac{\delta_1 \mu_1}{\sqrt{RT}} \left(P_i^2 - P^2\right)^{\frac{1}{2}} \tag{4.6}$$

Notice that the flow coefficient is used instead of the contraction coefficient and that q_1, δ_1, P_i and P are all function of angle and time. The mass efflux is derived in the same manner as the mass influx and is given by equation (4.7).

$$q_2 = \frac{\delta_2 \mu_2}{\sqrt{RT}} \left(P^2 - P_o^2\right)^{\frac{1}{2}} \tag{4.7}$$

In this case, q_2, δ_2, P and P_o are functions of angle and time. Also, the flow coefficient μ_2 is not constant as it was in the mass influx equation. As mentioned above there is a carry-over effect due to the jet produced by the first sealing knife. This jet could be dissipated if the distance between sealing knives, l, is large compared to the sealing clearance, δ. However, the seal used in the experiments in this work and in Millsaps work have a relatively small l, therefore, the flow coefficient is a function of the kinetic energy carry-over factor.

Since the flow coefficient depends on the carry-over factor, a means of determining this carry over factor is now shown. Millsaps [17] used an empirical relation created by Varmes in order to find this carry-over factor. This empirical relation is used here and is given by the following two equations.

$$\beta = \frac{1}{(1-\Phi)^{\frac{1}{2}}} \tag{4.8}$$

$$\Phi = \frac{8.52}{\frac{l_e}{\delta} + 7.23} \tag{4.9}$$

The effective pitch, l_e, is the distance the fluid must travel from one knife edge to the other, thus, this distance depends on the inlet swirl:

$$l_e = \frac{l}{\cos(\alpha_i)} \tag{4.10}$$

where α_i is the inlet swirl. From these expressions one notices that the carry-over factor, thus, the flow coefficient is at its minimum where the eccentric rotating shrouded rotor has its minimum gap. At the maximum gap the flow coefficient attains its maximum. This effect generates the direct force. Therefore, it is important to see how sensitive the carry-over factor is to an eccentric position of the shrouded rotor. This sensitivity is given by

$$\kappa = -C_c \left.\frac{\partial \beta}{\partial r}\right|_{r=0} \tag{4.11}$$

where r is the radial (eccentric) displacement. The seal clearance is simply a linear function of the radial displacement and equations (4.8), (4.9) and (4.10) are used in conjunction with (4.11) in order to obtain this sensitivity.

$$\kappa = -C_c \left.\frac{\partial \beta}{\partial r}\right|_{r=0} = \frac{8.52 C_c l}{2\delta^{*2}} \left[1 - \frac{8.52}{\frac{l}{\delta^*} + 7.23}\right]^{-\frac{3}{2}} \left[\frac{l}{\delta^*} + 7.23\right]^{-2} \tag{4.12}$$

Note that the asterisk denotes the concentric rotation of the rotor where the clearance is uniform around the circumference. This sensitivity multiplied by the radial displacement (magnitude of eccentricity) gives the change in the flow coefficient.

Therefore, the flow coefficient at the second knife is approximated by the centered value of the flow coefficient minus the change in the flow coefficient.

$$\mu_2 = \mu_2^* - \kappa r \tag{4.13}$$

Since small perturbations are investigated this approximation is sufficient.

This concludes the introduction to the equations describing the flow in the axial direction, now the continuity and momentum equations in the circumferential direction are presented and coupled to this axial flow. A control volume showing a differential location with all the pertinent mass fluxes is shown in Figure 4.3. The increase in mass within this control volume is balanced with the net mass inflow and the convection along the seal. Equation (4.14) gives this continuity equation.

$$\frac{\partial\left[\rho l(h+\delta_1)\right]}{\partial t} + \frac{1}{R_s}\frac{\partial\left[\rho V l(h+\delta_1)\right]}{\partial \theta} + q_2 - q_1 = 0 \tag{4.14}$$

Figure 4.4 shows the differential control volume which represents all the forces considered. Applying Newton's second law to these forces the momentum equation in the circumferential direction coupled to the momentum equation in the axial direction is derived.

$$\frac{\partial\left[\rho V l(h+\delta_1)\right]}{\partial t} + \frac{1}{R_s}\frac{\partial\left[\rho V^2 l(h+\delta_1)\right]}{\partial \theta} + q_2 V - q_1 V_i + \tau_s l - \tau_r(l+2h) + \frac{lh}{R_s}\frac{\partial P}{\partial \theta} = 0 \tag{4.15}$$

The Darcy friction law is used to relate the shear stresses to the tangential velocity, V, of the fluid within the cavity. The shear at the casing is denoted with a subscript "s" while the shear at the rotor is denoted with a subscript "r". The casing sees a fluid velocity of V while the rotor sees a fluid velocity of $(V - \omega R_s)$, therefore, the equations for these shear stresses are given by the following two equations.

$$\tau_s = \tfrac{1}{8}\rho\lambda_s V|V| = \tfrac{1}{8}\rho\lambda_s V^2 sgn(V) \tag{4.16}$$

$$\tau_r = \tfrac{1}{8}\rho\lambda_r(V-\omega R_s)|V-\omega R_s| = \tfrac{1}{8}\rho\lambda_r(V-\omega R_s)^2 sgn(\omega R_s - V) \tag{4.17}$$

Blasius' formula for a one dimensional flow in a hydrodynamically smooth duct is used to calculate the friction factors, λ_s and λ_r.

$$\lambda_s = 0.3164 Re_s^{*-0.25} \tag{4.18}$$

$$\lambda_r = 0.3164 Re_r^{*-0.25} \tag{4.19}$$

In order to determine the friction factors the Reynolds numbers must be determined. These Reynolds numbers are given by the following two equations.

$$Re_s^* = \left|\frac{VD_h}{\nu}\right| \tag{4.20}$$

$$Re_r^* = \left|\frac{(\omega R_s - V)D_h}{\nu}\right| \tag{4.21}$$

Notice that the diameter is the hydraulic diameter, D_h, which is given by four times the cross sectional area divided by the wetted perimeter:

$$D_h = \frac{4l(h+\delta_1)}{2l+2(h+\delta_1)} \tag{4.22}$$

The final set of equations presented, before a solution technique is shown, are the equations which describe the orbiting motion of the shrouded rotor. From Figure 4.2 one notices that there are two seal clearances, (δ_1 and δ_2), and their magnitude varies around the circumference of the shroud. For a rotor which is exhibiting an eccentric amplitude r with a circular whirl at a whirl angular velocity of Ω the following two equations completely describe its motion.

$$\delta_1 = \delta_1^* - \hat{r}\cos(\theta - \Omega t) \tag{4.23}$$

$$\delta_2 = \delta_2^* - \hat{r}\cos(\theta - \Omega t) \tag{4.24}$$

Variables with asterisks will always denote the concentric (non whirling) conditions.

4.3 Solution to the Governing Equations

The following section describes a linear perturbation technique to solve the system of equations derived above. Such a technique is used because one is interested in the effect a small amplitude eccentric rotation has on the stability of such a system. More comprehensive and, therefore, complicated nonlinear techniques may be used to solve these equations, however, the nonlinear terms (products of perturbations) are small and also limit cycle behavior is not of interest in this work. The linear perturbation technique gives complete results since it is capable of describing how the flow and geometric parameters interact to produce a nonuniform pressure perturbation around the circumference of the shroud. Ultimately these results are compared to those obtained from the wall tap pressure readings presented in chapter 3.

The linear perturbation solution to the above derived equations are divided into three parts. The solution begins with a zeroth order solution, that is, solving the equations with the rotor centered (concentric position). The second part involves perturbing the variables from their unperturbed concentric positions with small amplitude perturbations. The nonlinear terms are then discarded. The last part involves assuming harmonic solutions for the perturbations. This results in two algebraic equations with two unknowns, the pressure nonuniformity and the velocity nonuniformity around the circumference of the shroud. From the pressure nonuniformity the normal and tangential forces are obtained.

4.3.1 Zeroth Order Solution

As mentioned above, the zeroth order solution gives the rotor centered solution to the derived equations. All the variables are independent of time and space, therefore,

all spatial and temporal derivatives are dropped. These variable are denoted with an asterisk *. To begin with the continuity equation (4.14) becomes

$$q_2^* - q_1^* = 0 \tag{4.25}$$

The shear equations (4.16) and (4.17) are substituted into the momentum equation (4.15) and then the zeroth order simplification is undertaken which results in equation (4.26).

$$\frac{\rho^*}{8}\left[\lambda_s l V^{*2} - \lambda_r (l+2h)\left(V^* - \omega R_s\right)^2\right] + q_2^* V^* - q_1^* V_i^* = 0 \tag{4.26}$$

The steady state flow rate, q^*, is found from equations (4.6) and (4.7) and is given by

$$q^* = q_1^* = q_2^* = \frac{\delta_1^* \mu_1^*}{\sqrt{RT}}\left[P_i^{*2} - P^{*2}\right]^{\frac{1}{2}} = \frac{\delta_2^* \mu_2^*}{\sqrt{RT}}\left[P^{*2} - P_o^{*2}\right]^{\frac{1}{2}} \tag{4.27}$$

Equation (4.27) is then used in conjunction with equation (4.25) in order to obtain the zeroth order pressure in the cavity of the shroud. Solving for P^* one obtains the following equation:

$$P^* = \left[\frac{\delta_1^{*2}\mu_1^{*2}P_i^{*2} + \delta_2^{*2}\mu_2^{*2}P_o^{*2}}{\delta_1^{*2}\mu_1^{*2} + \delta_2^{*2}\mu_2^{*2}}\right]^{\frac{1}{2}} \tag{4.28}$$

The zeroth order density within the cavity is simply:

$$\rho^* = \frac{P^*}{RT} \tag{4.29}$$

The final step in this subsection is to calculate V^*. The momentum equation along with an iteration procedure is used to find this velocity. An iteration procedure is used because the shear terms within the momentum equation depend on V^* in a non elementary manner. The known inlet swirl velocity, V_i^*, is used as an initial guess.

Then ,λ_s and λ_r are calculated from equations (4.18) through (4.21). The momentum equation, equation (4.26), is then rearranged into a quadratic in V^*.

$$\frac{\rho^*}{8}[\lambda_s l - \lambda_r(l+2h)]V^{*2} + \left[q^* + \frac{\rho^*\lambda_r}{4}(l+2h)\omega R_s\right]V^* - \left[q^* V_i^* + \frac{\rho^*\lambda_r}{8}(l+2h)\omega^2 R_s^2\right] = 0 \tag{4.30}$$

At this point all the variables in equation (4.30) are known and, therefore, one is able to solve for V^*. The value calculated is compared to the original guess and if the following test holds then V^* is determined.

$$\left|V_{n+1}^* - V_n^*\right| < \varepsilon \tag{4.31}$$

Using this iteration procedure, the code took approximately 5 iterations to converge to 4 decimal points.

4.3.2 Linear Perturbation Approximation

A perturbation expansion about the centered rotor solution is shown in this section. The state variables are expressed as the zeroth order solution plus a small amplitude perturbation, as follows:

$$P = P^* + \tilde{P} \tag{4.32}$$

The small amplitude perturbation is given by $\tilde{P}$ where this perturbation is also written as a relative perturbation times the steady state solution.

$$P = P(\theta,t) = P^* + \tilde{P} = P^*\left(1 + \xi(\theta,t)\right) = P^* + \xi P^* \tag{4.33}$$

The relative perturbation, ξ, is dependent on the zeroth order quantities. Similarly, the above procedure may be applied to all other zeroth order variables discussed in the previous section.

$$P_i = P_i^* + \tilde{P}_i = P_i^*(1+\xi_i) \tag{4.34}$$

$$V_i = V_i^* + \tilde{V}_i = V_i^*(1+\eta_i) \tag{4.35}$$

$$V = V^* + \tilde{V} = V^*(1+\eta) \tag{4.36}$$

$$P_o = P_o^* + \tilde{P}_o = P_o^*(1+\xi_o) \tag{4.37}$$

$$q_1 = q_1^* + \tilde{q}_1 = q_1^*(1+\zeta_1) \tag{4.38}$$

$$q_2 = q_2^* + \tilde{q}_2 = q_2^*(1+\zeta_2) \tag{4.39}$$

$$\rho = \rho^* + \tilde{\rho} = \rho^*(1+\varsigma) \tag{4.40}$$

Notice that the inlet pressure and velocity and the exit pressure are taken to be nonuniform. This nonuniformity is found in the experimental results as described and illustrated in chapter 3. In the next chapter, where the results of this theory are presented, the nonuniformity measured by experiment at the inlet and the outlet of the shroud is used as inputs for the theoretical solution. The nonuniformity within the cavity, $P(\theta,t)$, can then be found.

The next step is to express the axial mass flow rates, q_1 and q_2 as functions of steady state flow and pressure terms along with perturbations in pressure only. This is accomplished by dividing equations (4.6) and (4.7) by (4.27) and then performing a Taylor series expansion in ξ_i and ξ for the first equation and then performing another Taylor series expansion in ξ and ξ_o for the second equation. By taking only the zeroth and first terms and eliminating all higher order terms one is able to simplify the mass flow rate equations to

$$q_1 = q^* \frac{\delta_1}{\delta_1^*}\left[1 - \xi \frac{P^{*2}}{P_i^{*2} - P^{*2}} + \xi_i \frac{P_i^{*2}}{P_i^{*2} - P^{*2}}\right] \tag{4.41}$$

$$q_2 = q^* \frac{\delta_2 \mu_2}{\delta_2^* \mu_2^*}\left[1+\xi\frac{P^{*2}}{P^{*2}-P_o^{*2}}-\xi_o\frac{P_o^{*2}}{P^{*2}-P_o^{*2}}\right] \tag{4.42}$$

The density within the shroud cavity can be expressed as the steady state density and the pressure perturbation by using the adiabatic isentropic relationship.

$$\rho = \rho^*\left(1+\frac{\xi}{\gamma}\right) \tag{4.43}$$

In order to obtain the linearized continuity equation, equations (4.33) through (4.43) are substituted into the complete continuity equation presented above (equation (4.14)). The higher order terms which are products of perturbations are eliminated because they are much smaller than the first order terms. The result of this manipulation give the linearized continuity equation.

$$\begin{aligned}
&\rho^* l\frac{\partial \delta_1}{\partial t}+\frac{\rho^* lh}{\gamma}\frac{\partial \xi}{\partial t}+\frac{1}{R_s}\left[\rho^* V^* l\frac{\partial \delta_1}{\partial \theta}+\rho^* V^* lh\frac{\partial \eta}{\partial \theta}+\frac{\rho^* V^* lh}{\gamma}\frac{\partial \xi}{\partial \theta}\right] \\
&+q^*\left(\frac{1}{\delta_1^*}-\frac{1}{\delta_2^*}-\frac{\kappa}{\mu_2^*}\right)r+q^*\left[\frac{P^{*2}}{P^{*2}-P_o^{*2}}+\frac{P^{*2}}{P_i^{*2}-P^{*2}}\right]\xi \\
&-q^*\left[\xi_i\frac{P_i^{*2}}{P_i^{*2}-P^{*2}}+\xi_o\frac{P_o^{*2}}{P^{*2}-P_o^{*2}}\right]=0
\end{aligned} \tag{4.44}$$

The linearized momentum equation is obtained in the same fashion. The perturbation equations are substituted into the momentum equation (equation (4.15)) and all higher order terms are eliminated. The zeroth order momentum equation (equation (4.26)) is also called upon to further simplify the resulting linearized momentum equation:

$$\rho^* V^* lh\frac{\partial \eta}{\partial t}+\rho^* V^* l\frac{\partial \delta_1}{\partial t}+\frac{\rho^* V^* lh}{\gamma}\frac{\partial \xi}{\partial t}+\frac{\rho^* RTl(h+\delta_1)}{R_s}\frac{\partial \xi}{\partial \theta}$$

$$+\frac{1}{R_s}\left[2\rho^*V^{*2}lh\frac{\partial\eta}{\partial\theta}+\rho^*V^{*2}l\frac{\partial\delta_1}{\partial\theta}+\rho^*V^*lh\frac{\partial\eta}{\partial\theta}+\frac{\rho^*V^{*2}lh}{\gamma}\frac{\partial\xi}{\partial\theta}\right]$$

$$+q^*\left[\frac{V^*P^{*2}}{P^{*2}-P_o^{*2}}+\frac{V_i^*P^{*2}}{P_i^{*2}-P^{*2}}\right]\xi-q^*\left[\xi_i\frac{V_i^*P_i^{*2}}{P_i^{*2}-P^{*2}}+\xi_o\frac{V^*P_o^{*2}}{P^{*2}-P_o^{*2}}\right] \qquad (4.45)$$

$$+\frac{\rho^*}{8\gamma}\left[\lambda_s lV^{*2}-\lambda_r(l+2h)\left(V^*-\omega R_s\right)^2\right]\xi+q^*V^*\eta-q^*V_i^*\eta_i$$

$$\frac{\rho^*V^*}{4}\left[\lambda_s lV^*-\lambda_r(l+2h)\left(V^*-\omega R_s\right)\right]\eta+q^*\left(\frac{V_i^*}{\delta_1^*}-\frac{V^*}{\delta_2^*}-\frac{V^*\kappa}{\mu_2^*}\right)r=0$$

The result is a linear system of partial differential equations in both pressure, P, and velocity, V, with periodic boundary conditions. The following section will describe a technique to reduce equations (4.44) and (4.45) to a system of complex linear algebraic equations.

4.3.3 Harmonic Solutions

The variation in gap, r, is the non-homogeneous term in the continuity and momentum equations and is assumed to consist of a first harmonic of the azimuth angle measured from a whirling reference, $\psi=\theta-\Omega t$. The perturbation in pressure at the inlet, ξ_i, within the cavity, ξ and at the exit, ξ_o, of the shroud and the perturbation in velocity at the inlet, η_i, and within the cavity, η, are assumed to follow the same functional dependence as the variation in gap and consist solely of a first harmonic. As mentioned above, the magnitude and phase of the inlet and exit terms are obtained from experimental results while the pressure and velocity non-uniformities within the cavity are the two unknowns in these two equations. Complex exponential notation is used to express these harmonic solutions (real parts being understood to be extracted). The variation in gap is expressed as

$$r=\hat{r}e^{i(\theta-\Omega t)} \qquad (4.46)$$

the perturbation in pressure at the inlet within the cavity and at the exit are given by

$$\xi_i = \hat{\xi}_i e^{i(\theta-\Omega t)} \tag{4.47}$$

$$\xi = \hat{\xi} e^{i(\theta-\Omega t)} \tag{4.48}$$

$$\xi_o = \hat{\xi}_o e^{i(\theta-\Omega t)} \tag{4.49}$$

and the perturbation in velocity at the inlet and within the cavity are respectively,

$$\eta_i = \hat{\eta}_i e^{i(\theta-\Omega t)} \tag{4.50}$$

$$\eta = \hat{\eta} e^{i(\theta-\Omega t)} \tag{4.51}$$

The partial derivatives of equations (4.23), (4.47) through (4.49) and (4.51) with respect to angle and time are

$$\frac{\partial \delta_1}{\partial \theta} = -i\hat{r} e^{i(\theta-\Omega t)} \tag{4.52}$$

$$\frac{\partial \delta_1}{\partial t} = i\Omega \hat{r} e^{i(\theta-\Omega t)} \tag{4.53}$$

$$\frac{\partial \xi_i}{\partial \theta} = i\hat{\xi}_i e^{i(\theta-\Omega t)} \tag{4.54}$$

$$\frac{\partial \xi_i}{\partial t} = -i\Omega \hat{\xi}_i e^{i(\theta-\Omega t)} \tag{4.55}$$

$$\frac{\partial \xi}{\partial \theta} = i\hat{\xi} e^{i(\theta-\Omega t)} \tag{4.56}$$

$$\frac{\partial \xi}{\partial t} = -i\Omega \hat{\xi} e^{i(\theta-\Omega t)} \tag{4.57}$$

$$\frac{\partial \xi_o}{\partial \theta} = i\hat{\xi}_o e^{i(\theta-\Omega t)} \tag{4.58}$$

$$\frac{\partial \xi_o}{\partial t} = -i\Omega \hat{\xi}_o e^{i(\theta-\Omega t)} \tag{4.59}$$

$$\frac{\partial \eta}{\partial \theta} = i\hat{\eta} e^{i(\theta-\Omega t)} \tag{4.60}$$

$$\frac{\partial \eta}{\partial t} = -i\Omega \hat{\eta} e^{i(\theta-\Omega t)} \tag{4.61}$$

All the pertinent equations are then substituted into the linearized continuity and momentum equations (equations (4.44) and (4.45)) and the complex exponential (phasor) is eliminated. After rearranging and placing the unknown terms, $\hat{\xi}$ and $\hat{\eta}$ on

the left side of the equation and the forcing terms, $\hat{\xi}_i$, $\hat{\xi}_o$, $\hat{\eta}_i$ and $\hat{r}$, on the right side of the equation one obtains the following from the continuity equation:

$$\left\{q^*\left[\frac{P^{*2}}{P_i^{*2}-P^{*2}}+\frac{P^{*2}}{P^{*2}-P_o^{*2}}\right]+\frac{\rho^* lh}{\gamma}\left(\frac{V^*}{R_s}-\Omega\right)i\right\}\hat{\xi}+\left\{\frac{\rho^* V^* lh}{R_s}i\right\}\hat{\eta}=$$

$$\left\{\frac{q^*\kappa}{\mu_2^*}+q^*\left(\frac{1}{\delta_2^*}-\frac{1}{\delta_1^*}\right)+\rho^* l\left(\frac{V^*}{R_s}-\Omega\right)i\right\}\hat{r}+\left\{q^*\left[\frac{P_i^{*2}}{P_i^{*2}-P^{*2}}\hat{\xi}_i+\frac{P_o^{*2}}{P^{*2}-P_o^{*2}}\hat{\xi}_o\right]\right\} \tag{4.62}$$

and the momentum equation becomes:

$$\left\{q^*\left[\frac{V_i^* P^{*2}}{P_i^{*2}-P^{*2}}+\frac{V^* P^{*2}}{P^{*2}-P_o^{*2}}\right]+\frac{\rho^*}{8\gamma}\left[\lambda_s lV^{*2}-\lambda_r(l+2h)\left(\omega R_s-V^*\right)^2\right]\right\}\hat{\xi}$$

$$+\left\{\left[\frac{\rho^* V^* lh}{\gamma}\left(\frac{V^*}{R_s}-\Omega\right)+\frac{\rho^* RTl\left(h+\delta^*\right)}{R_s}\right]i\right\}\hat{\xi}$$

$$+\left\{q^* V^*+\frac{\rho^* V^*}{4}\left[\lambda_s lV^*-\lambda_r(l+2h)\left(V^*-\omega R_s\right)\right]+\rho^* V^* lh\left[\frac{2V^*}{R_s}-\Omega\right]i\right\}\hat{\eta} \tag{4.63}$$

$$=\left\{\frac{q^* V^*\kappa}{\mu_2^*}+q^*\left(\frac{V^*}{\delta_2^*}-\frac{V_i^*}{\delta_1^*}\right)+\rho^* V^* l\left(\frac{V^*}{R_s}-\Omega\right)i\right\}\hat{r}$$

$$+\left\{q^*\left[V_i^*\hat{\eta}_i+\frac{V_i^* P_i^{*2}}{P_i^{*2}-P^{*2}}\hat{\xi}_i+\frac{V^* P_o^{*2}}{P^{*2}-P_o^{*2}}\hat{\xi}_o\right]\right\}$$

The above equations can be represented in matrix form.

$$\begin{bmatrix} A_{1,1}+iB_{1,1} & A_{1,2}+iB_{1,2} \\ A_{2,1}+iB_{2,1} & A_{2,2}+iB_{2,2} \end{bmatrix}\begin{bmatrix}\hat{\xi}\\ \hat{\eta}\end{bmatrix}=\begin{bmatrix} C_1+iD_1 \\ C_2+iD_2 \end{bmatrix}\hat{r}+\begin{bmatrix} E_1 \\ E_2 \end{bmatrix} \tag{4.64}$$

The solution to (4.64) gives the magnitude and phase of the pressure and velocity perturbation within the cavity of the shroud. However, before this theoretical model is used, equations (4.62) and (4.63) are nondimensionalized.

4.4 Nondimensionalization

Greater physical insight is gained from nondimensionalizing equations (4.62) and (4.63). Millsaps [17] has done an extensive parametric study on the effects of varying these nondimensional coefficients, therefore, in the interest of completeness the nondimensionalization is presented in this work. Also, the work which is presented in chapter 5 is an extension of Millsaps work. The extension includes a study on the effect the pressure and velocity nonuniformities upstream and the pressure nonuniformity downstream have on the theoretical predictions of the pressure and velocity perturbations within the cavity of the shroud. Also, the next chapter contains the results of this theory using the geometry and flow conditions present in the experimental facility[1]. First, however, the nondimensional equations are presented in this section.

4.4.1 Scaling Quantities

The steady flow rate, q^*, is the logical parameter to use in order to normalize the continuity equation. It is a little harder to find an optimum parameter that can be used to normalize velocities. The are many choices such as ωR_s, w_1, V_i, and V^*. The problem with ωR_s is that it leads to a singularity when the shaft speed is zero. When all is said and done, it appears that V^* is the best choice for scaling forces over the widest range of conditions. Also, the least set of redundant nondimensional parameters is given by V^*.

4.4.2 Nondimensional Parameters

The continuity equation when nondimensionalized by q^* and the momentum equation when nondimensionalized by V^* yields three categories of nondimensional parameters. The first category contains the geometrical ratios, the second category

[1]As described in Chapters 2 and 3.

contains the velocity ratios while the last category are the ratios of dynamic quantities.

The geometric ratios are defined as follows:

$$\varepsilon_1 = \frac{\hat{r}}{\delta_1^*} \quad \alpha = \frac{\delta_2^*}{\delta_1^*} \quad D = \frac{\delta_1^*}{h} \quad H = \frac{h}{R_s} \quad K = \frac{\kappa \delta_1^*}{\mu_2^*} \quad L = \frac{l}{R_s} \tag{4.65}$$

The first parameter of equation (4.65) is ε_1 and is simply the normalized eccentricity. The convergence or divergence of the seal is given by α. When α=1 this condition states that the gaps over the seal knives are equal as in the case of the shroud that is used in the experiments as presented in chapters 2 and 3. The following parameter, D, normalizes the mean gap by the seal depth and, therefore, describes the ratio of the change in the local sealing gap to the shrouded rotor cross sectional area. The height of the sealing strip normalized by the radius of the seal is given by H. The next nondimensional parameter is K and it is analogous to α when α<1 and basically behaves as $K \sim \frac{1}{\alpha} - 1$. If the gap is smaller at the exit of the shroud this parameter describes the reduction in mass efflux from the shroud. The last parameter is L and it is simply the ratio of the seal width to the seal radius. Both H and L are basic geometric ratios, however, they play an important part in that they contribute to the frictional shear forces within the shroud.

There are two kinematic parameters to discuss, the nondimensional shaft speed and the nondimensional whirling speed. They are both given in equation (4.66).

$$S = \frac{\omega R_s}{V^*} \qquad W = \frac{\Omega R_s}{V^*} \tag{4.66}$$

The spin rate of the shaft and the whirl rate of the shaft are compared to the swirling velocity of the fluid via the above equations. Values of S less than one indicate that the fluid in the cavity is swirling at a greater speed than the shaft is rotating, therefore, the shroud tends to slow the fluid. The dominant parameter for discussing dynamic destabilizing forces is W. Even though the experimental facility is static, dynamic

terms are still discussed from the theoretical viewpoint. Once the dynamic theoretical model is derived it can always be simplified to predict the static case as in the experimental facility. These type of simplifications are discussed further within this chapter and the following chapter. Once the nondimensional equations are presented in section 4.4.3 one may notice that the group $V_i(1-W)$ is found within these equations. This term indicates the relative gland swirl seen by an observer rotating in the whirling frame of the rotor at a frequency of Ω. This quantity describes whether the swirling fluid in the cavity overtakes or is overtaken by the traveling waves. If W=1 there is no relative gland swirl and from symmetry there is no cross force[2].

The final category of parameters to discuss involves the dynamic ratios. These ratios are given in equation (4.67).

$$\Delta = \frac{q^*}{\mu_1^* \delta_1^* \rho^* \sqrt{RT}} \qquad \sigma = \frac{\rho^* V^* \delta_1^*}{q^*} \qquad \Gamma = 1 - \frac{V_i^*}{V^*} \tag{4.67}$$

The nondimensional flow rate is given by Δ and by using equations (4.27) and (4.29) one is able to rewrite Δ in the following form:

$$\Delta = \frac{q^*}{\mu_1^* \delta_1^* \rho^* \sqrt{RT}} = \left[\left(\frac{P_i^*}{P^*} \right)^2 - 1 \right]^{\frac{1}{2}} \tag{4.68}$$

By substituting equation (4.28) into equation (4.68) and simplifying, one may now show that Δ is actually a measure of the axial pressure gradient from inlet to exit.

$$\Delta = \left[\frac{\pi_s^2 - 1}{\left(\frac{\pi_s \mu_1^*}{\alpha \mu_2^*} \right)^2 + 1} \right]^{\frac{1}{2}} \tag{4.69}$$

The ratio of the inlet pressure to the exit pressure is given by π_s.

[2]This is only true in the absence of frictional effects. See Millsaps [17] chapter 3 for further discussion on these effects.

The next parameter, σ, is called the swirl parameter and it basically compares the circumferential velocity to the axial velocity. The final dynamic parameter is Γ which compares the inlet velocity to the velocity that exists in the shroud cavity. The degree to which viscous shear forces alter the swirl velocity as the fluid travels from the inlet into the cavity is conveyed by this parameter. For the inviscid case, shear forces are absent, therefore, Γ should equal zero.

4.4.3 Nondimensional Equations

Nondimensionalizing the continuity and momentum equations by q^* and q^*V^* respectively and grouping terms as described above one obtains the nondimensional continuity equation (4.70),

$$\begin{aligned}&\left\{\left[\left(\frac{\alpha\mu_2^*}{\Delta\mu_1^*}\right)^2+\left(\frac{1}{\Delta}\right)^2\right]+\left[\frac{\sigma L}{D\gamma}(1-W)\right]i\right\}\hat{\xi}+\left\{\frac{\sigma L}{D}i\right\}\hat{\eta}\\&=\left\{\left[K+\left(\frac{1}{\alpha}-1\right)\right]+[\sigma L(1-W)]i\right\}\varepsilon_1+\left\{\left[1+\left(\frac{1}{\Delta}\right)^2\right]\hat{\xi}_i+\left[\left(\frac{\alpha\mu_2^*}{\Delta\mu_1^*}\right)^2-1\right]\hat{\xi}_o\right\}\end{aligned}\tag{4.70}$$

and the nondimensional momentum equation (4.71).

$$\begin{aligned}&\left\{\left(\frac{\alpha\mu_2^*}{\Delta\mu_1^*}\right)^2+\left(\frac{1-\Gamma}{\Delta^2}\right)+\frac{\sigma L}{8\gamma DH}\left[\lambda_s-\lambda_r\left(1+\frac{2H}{L}\right)(S-1)^2\right]+\left[\frac{\sigma L}{D\gamma}(1-W)+\frac{L}{\Delta^2\sigma\mu_1^{*2}D}\right]i\right\}\hat{\xi}\\&+\left\{1+\frac{\sigma L}{4DH}\left[\lambda_s-\lambda_r\left(1+\frac{2H}{L}\right)(1-S)\right]+\frac{\sigma L}{D}[2-W]i\right\}\hat{\eta}\\&=\left\{\left[K+\left(\frac{1}{\alpha}-1\right)\right]+\Gamma+[\sigma L(1-W)]i\right\}\varepsilon_1\\&+\left\{[1-\Gamma]\hat{\eta}_i+\left[(1-\Gamma)\left(1+\left(\frac{1}{\Delta}\right)^2\right)\right]\hat{\xi}_i+\left[\left(\frac{\alpha\mu_2^*}{\Delta\mu_1^*}\right)^2-1\right]\hat{\xi}_o\right\}\end{aligned}\tag{4.71}$$

In order to obtain the more compact convective form of the momentum equation (4.72), the continuity equation (4.70) is subtracted from the momentum equation (4.71).

$$\left\{\frac{-\Gamma}{\Delta^2}+\frac{\sigma L}{8\gamma DH}\left[\lambda_s-\lambda_r\left(1+\frac{2H}{L}\right)(S-1)^2\right]+\left[\frac{L}{\Delta^2\sigma\mu_1^{*2}D}\right]i\right\}\hat{\xi}$$

$$+\left\{1+\frac{\sigma L}{4DH}\left[\lambda_s-\lambda_r\left(1+\frac{2H}{L}\right)(1-S)\right]+\frac{\sigma L}{D}[1-W]i\right\}\hat{\eta} \qquad (4.72)$$

$$=\Gamma\varepsilon_1+\left\{[1-\Gamma]\hat{\eta}_i-\left[\Gamma\left(1+\left(\frac{1}{\Delta}\right)^2\right)\right]\hat{\xi}_i\right\}$$

Equations (4.70) and (4.72) form the system of equations used to determine the pressure and velocity perturbations within the cavity of the shroud. Chapter 5 explains the computer code that solves this system of equations and the studies that were performed using this code.

4.5 Interpretation of Solutions

Once again, the solution to equations (4.70) and (4. 72) give the pressure, $\hat{\xi}$, and velocity, $\hat{\eta}$, perturbations within the cavity of the shroud. These perturbations are complex constants and contain both magnitude and phase information. They are represented in the complex plane and this is illustrated by referring to Figure 4.5 and to equations (4.73) and (4.74) for the pressure and velocity representation respectively.

$$\hat{\xi}=\hat{\xi}_{\Re}+i\hat{\xi}_{Im} \qquad (4.73)$$

$$\hat{\eta}=\hat{\eta}_{\Re}+i\hat{\eta}_{Im} \qquad (4.74)$$

Amplitude of the pressure and velocity is simply given by

$$\left|\hat{\xi}\right|=\left[\hat{\xi}_{\Re}^2+\hat{\xi}_{Im}^2\right]^{\frac{1}{2}} \qquad (4.75)$$

$$\left|\hat{\eta}\right|=\left[\hat{\eta}_{\Re}^2+\hat{\eta}_{Im}^2\right]^{\frac{1}{2}} \qquad (4.76)$$

The phase angles ψ_ξ and ψ_η shown in Figure 4.5 respectively give the angular location ahead of the minimum gap where the maximum value of pressure and velocity occur.

$$\psi_\xi = Tan^{-1}\left[\frac{\hat{\xi}_{Im}}{\hat{\xi}_{\Re}}\right] \tag{4.77}$$

$$\psi_\eta = Tan^{-1}\left[\frac{\hat{\eta}_{Im}}{\hat{\eta}_{\Re}}\right] \tag{4.78}$$

As one might expect the above phase angles are defined over an interval from $-\pi$ to π where Tan^{-1} is multi-valued. Therefore, the sign of these phase angles are chosen as follows:

$$\hat{\xi}_{Im}, \hat{\eta}_{Im} > 0 \Rightarrow \psi_\xi, \psi_\eta > 0 \tag{4.79}$$

$$\hat{\xi}_{Im}, \hat{\eta}_{Im} < 0 \Rightarrow \psi_\xi, \psi_\eta < 0 \tag{4.80}$$

The sign of the phase angles can be used to tell whether the calculated distribution of both pressure and velocity nonuniformity tend to destabilize a whirling rotor. However, as is seen in the previous chapters, nonuniformity in the pressure distribution is not the only mechanism that can trigger rotordynamic instability. Another mechanism, as was mentioned previously, is the Alford effect. Therefore, rather than having to deal with the incomplete stability information provided by the pressure and velocity perturbations, the rotordynamic forces due to these perturbations are determined. A method of calculating the rotordynamic forces from the determined perturbations is shown in the next section. These forces then may be combined with the forces determined from the other mechanisms to ultimately determine a systems stability.

4.6 Rotordynamic Forces

The rotordynamic forces are found by integrating all stresses over the shroud's land. This calculation is similar to the integration shown by equations (1.11) and (1.12) when calculating normal and tangential forces from the pressure nonuniformity around the circumference of the shrouded rotor. The first item to note is that only the first harmonic perturbations contributes to the net rotordynamic forces because of orthogonality. Second, as one might expect, the forces are due to two types of stresses, the normal stress due to pressure and the shear stress due to friction. The normal stress is calculated via the pressure perturbation while the shear stress is calculated via the velocity perturbation and the forces resulting from these two stresses are calculated via equations (4.81) and (4.82) respectively.

$$F_{Pressure} = \int \hat{\xi} P^* dA \tag{4.81}$$

$$F_{Shear} = \int 2\lambda\hat{\eta}\frac{\rho^*}{8}V^{*2}dA \tag{4.82}$$

Millsaps [17] has shown that the force due to the shear stress is much smaller than the force due to the normal stress, therefore, only the pressure forces will be calculated. As is shown in chapter 1, the force due to the pressure perturbation is decomposed into normal and tangential components. Once again the normal force, F_N, is the component of force acting in the direction of instantaneous minimum gap (positive is destabilizing) and the tangential force, F_T, is the component of force acting perpendicular to that minimum gap (positive in the forward whirling direction). Note that the system is allowed to whirl, therefore, as described in chapter 1, the normal and tangential forces are functions of whirl frequency, Ω. Equations (4.83) and (4.84) gives these normal and tangential forces and show that they can be expressed in terms of the amplitude and phase information determined from the theoretical solution.

$$F_N = F_N(\Omega) = -R_s l\int_0^{2\pi} P(\psi)Cos\psi d\psi = -R_s l\int_0^{2\pi} \left|\hat{\xi}\right| P^* Cos(\psi - \psi_\xi)d\psi \tag{4.83}$$

$$= -\pi R_s l \left|\hat{\xi}\right| P^* Cos\psi_\xi = -\pi R_s l P^* \Re(\hat{\xi})$$

Equation (4.84) is derived in a similar fashion.

$$F_T = -\pi R_s l \left|\hat{\xi}\right| P^* Sin\psi_\xi = -\pi R_s l P^* Im(\hat{\xi}) \tag{4.84}$$

In order to compare the forces obtained from the theoretical solution to that of the experiment the whirl frequency is set to zero. This gives a static displacement and the normal and tangential forces that result from the calculations are static and may be termed the direct and cross force. The computer code that performs the above theoretical calculations and the values of each of the pertinent inputs to this code are described in the chapter 5. The direct and cross force theoretical results for the geometry of the experimental shrouded turbine are also given in following chapter. Chapter 5 also contains a study on the sensitivity of the analytical model to the inlet and exit pressure and velocity perturbations. Chapter 6 compares the results of the theoretical model predictions to those experimentally determined.

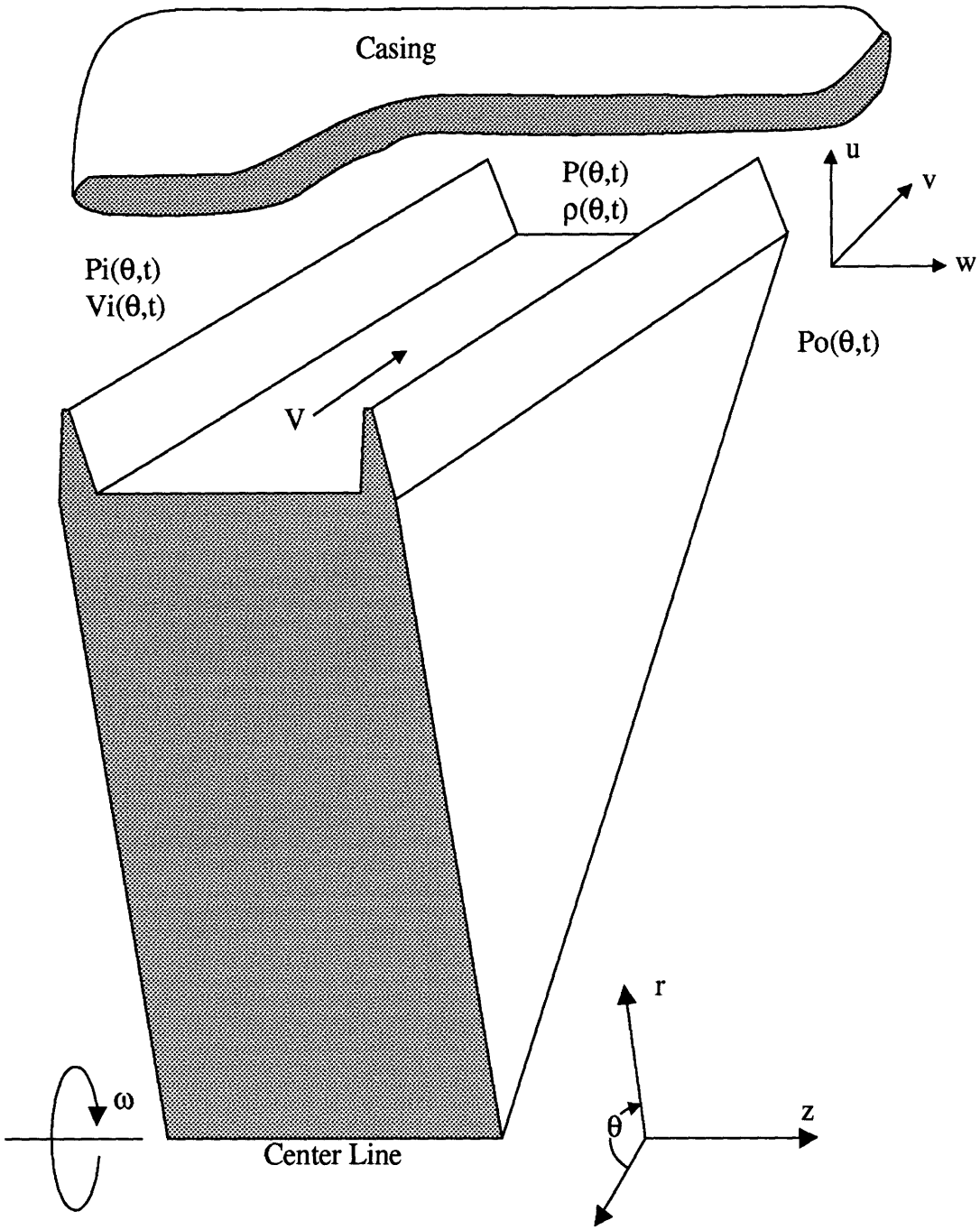

Figure 4.1: Section View of the Shroud Illustrating the Coordinates and Flow Parameters. [16,17]

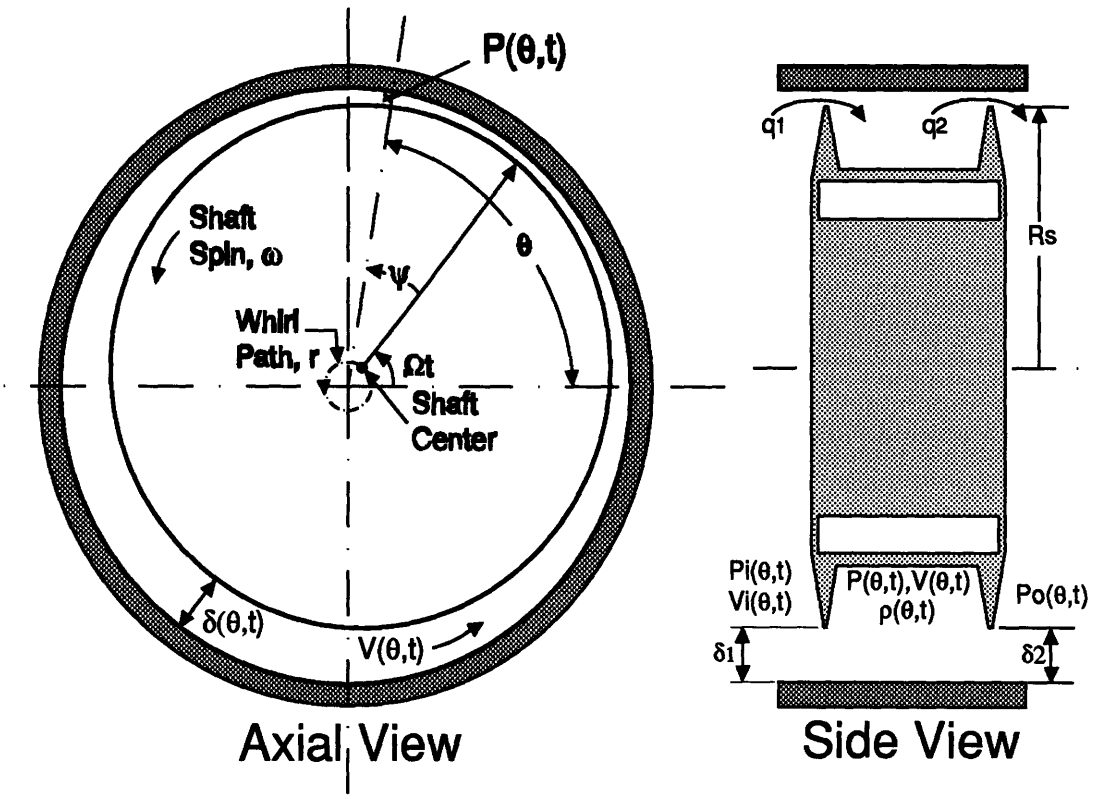

Figure 4.2: Axial View and Side View of the Shrouded Turbine Illustrating the Kinematic, Geometric and Flow Parameters Used in the Theoretical Model. [16,17]

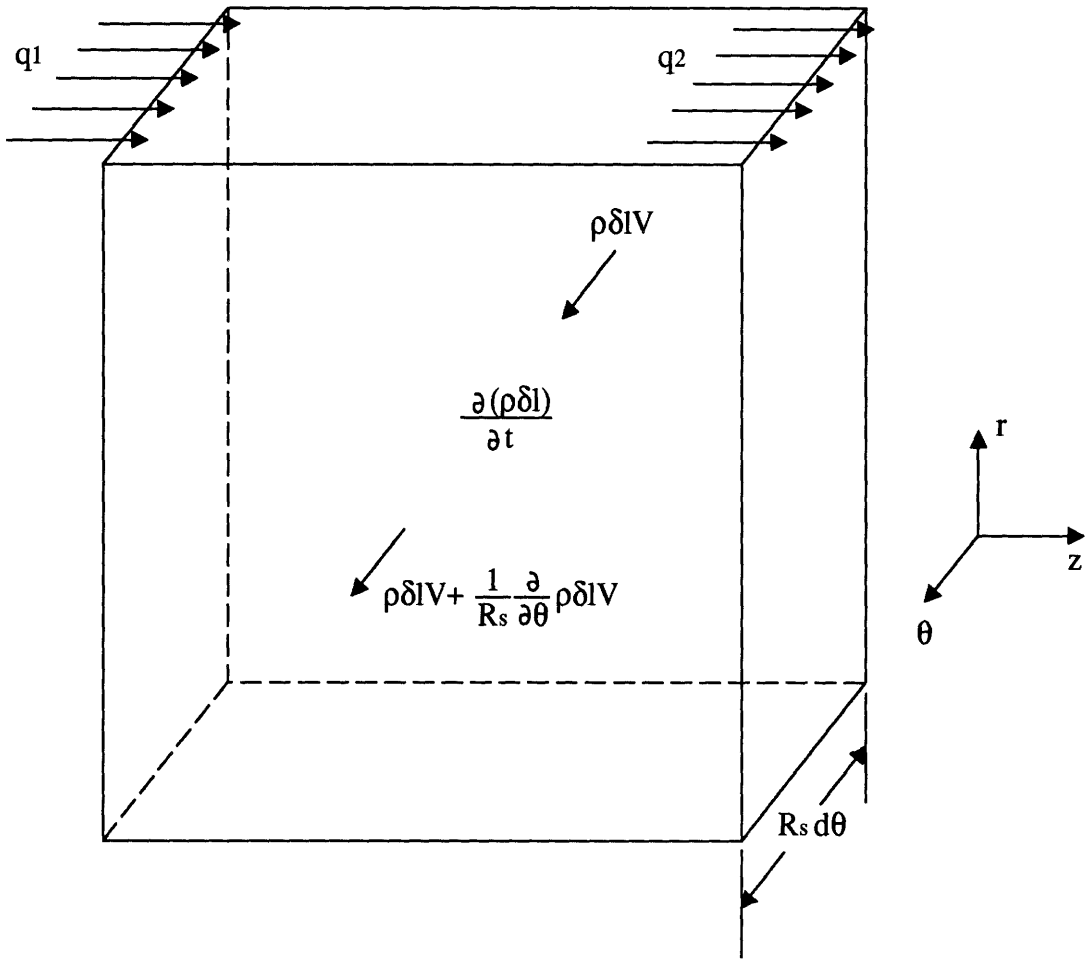

Figure 4.3: Control Volume for the Derivation of the Continuity Equation. [16,17]

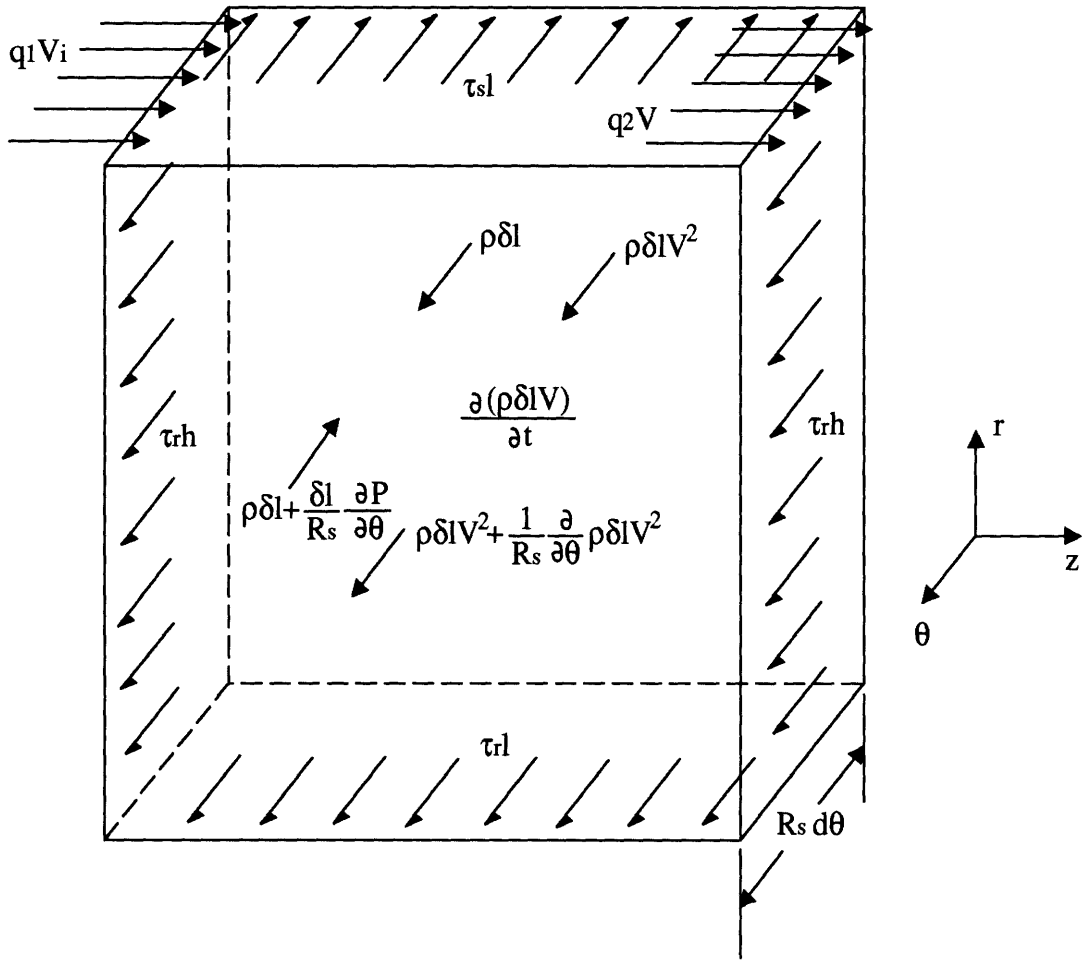

Figure 4.4: Control Volume for the Derivation of the Momentum Equation. [16,17]

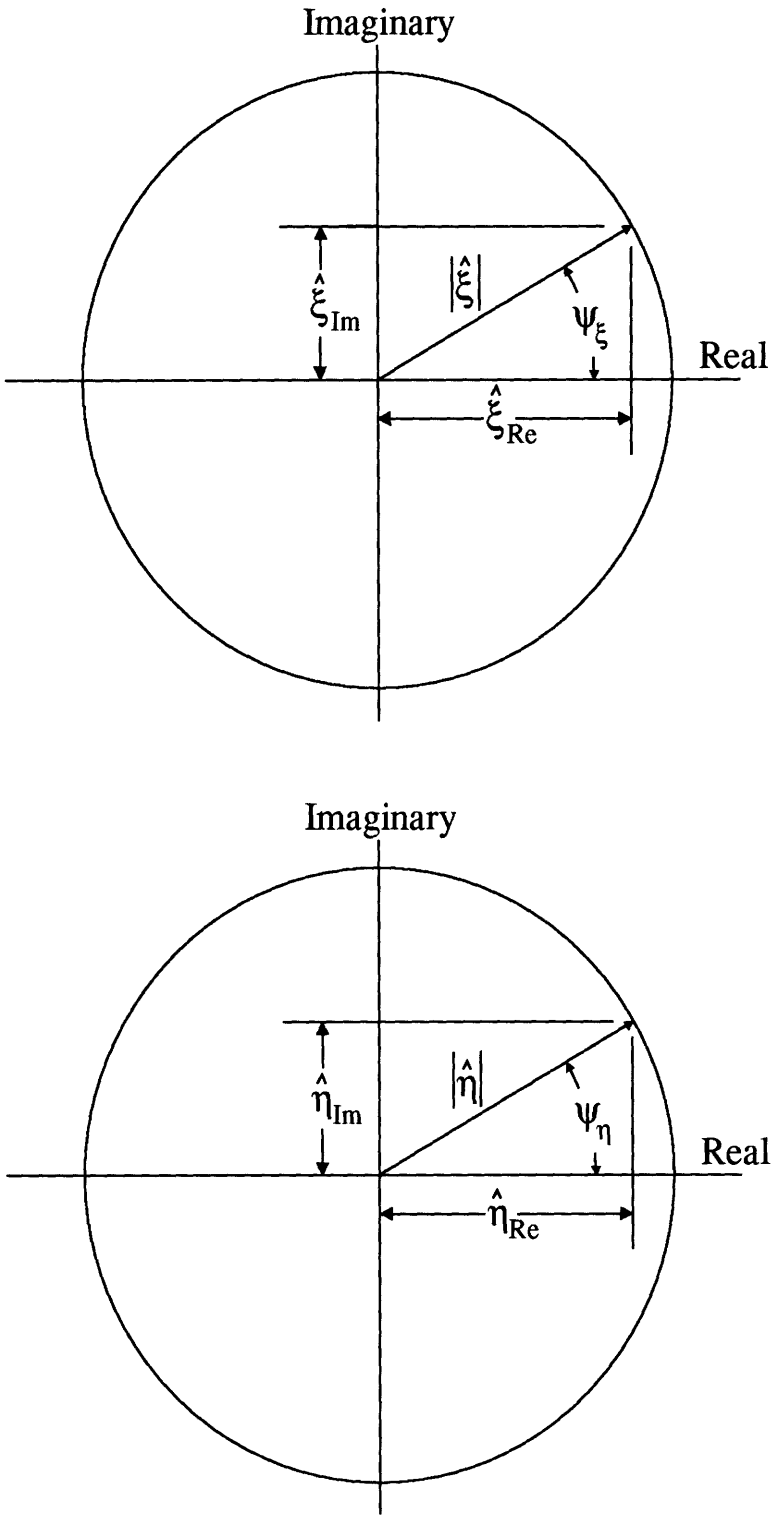

Figure 4.5: Complex Plane Representation of the Complex Amplitude of the Pressure and Velocity Perturbations. [16,17]

Chapter 5

Application of the Analytical Model

5.1 Model Parameters and Their Values

The perturbation in pressure within the cavity of the shroud is obtained by the solution of the two by two system of linear equations which are derived in chapter 4. As mentioned previously, these equations require certain flow and geometric quantities to be known along with certain inlet and exit perturbations. Sections 5.1.1. and 5.1.2 explain the values given to the flow and geometric variables respectively. These values are such that the shroud depicted by this analytical model is similar to the shroud which exists in the experimental facility. Section 5.1.3 describes the computer code used to solve the system of equations which are derived in the previous chapter. Studies of the effect the inlet and exit conditions have on the theoretically predicted direct and cross forces are illustrated in section 5.2. This chapter ends with the results of applying the model to the test conditions that exist in the experimental facility. Chapter 6 compares the results of the experimental study with the theoretical results.

5.1.1 Flow Conditions

To calculate the pressure perturbation within the shroud's cavity the following input flow parameters are determined: the inlet and exit pressures along with their perturbations, the temperature, and the inlet tangential flow velocity along with its perturbation. The experimental facility design flow conditions are used for these values, however, not all the inputs are direct measurements from the facility since the facility does not contain means to measure certain properties. Therefore, certain

calculations are performed. The shroud's inlet pressure is basically the pressure after the stator. However, a modification is made to account for the stagnation of the axial momentum component against the first sealing strip, *i.e.*, adding to the static pressure the dynamic head $\frac{1}{2}\rho_i \vec{u}_i^2$. Since the tangential component $\frac{1}{2}\rho_i (V_i)^2$ is preserved, the correction is relatively small. It is, however, noticeable because the rotor pressure drop in this low reaction turbine is itself small. The next step is to understand how to obtain the inlet tangential velocity, which is found by first determining the axial velocity, U_{es}, at the exit of the stator. The axial velocity used here is determined theoretically taking into account the blockage caused by the shroud band. First, as mentioned above, the axial velocity component of the fluid exiting the stator stagnates at the sealing strip, however, the tangential component, V_i, is preserved and has the same value as at the exit of the stator. The axial velocity component, U_{es}, at the exit of the stator is determined in order to calculate this tangential velocity component. The axial velocity is first found as if there is no blockage and then the blockage is taken into account.

In order to model this blockage it is found that the flow in the cross plane is de-coupled from the axial flow. This allows one to model the flow within the test section as a flow within a channel. Upstream the channel has a width of H_s (representing the height of the stator blades) and downstream the channel has a height of B_H (representing the height of the rotor blades). The change in height is accomplished through a step (representing the blockage by the seal). At the corner of the step is a sink (representing the leakage through the seal). One can assume that the channel has a very slight taper such that infinitely upstream the channel converges (the width, H_s, goes to zero, $H_s \to 0$, far upstream). Also, the same is said for the downstream channel width, where infinitely downstream the channel converges (the width, B_H, goes to zero, $B_H \to 0$, far downstream). This procedure gives a closed polygon which is then mapped to a half-plane via the Schwarz-Christoffel formula. Applying the transformation along with the flow conditions that exist in this type of channel one

obtains equation (5.1) which is the ratio of the axial velocity at the exit of the stator with blockage to the axial velocity at the exit of the stator without blockage.

$$\frac{U_{es}}{U_{0es}} = \frac{1}{p}\left(1+\mu\frac{a}{u-a}\right) \tag{5.1}$$

where,

$$p = \sqrt{\frac{u-1}{u-a}} \tag{5.2}$$

and

$$a = \left(\frac{H_s}{B_H}\right)^2 \tag{5.3}$$

The axial velocity without blockage is given by U_{0es} while the axial velocity with blockage is given by U_{es}. The variable μ is the fraction of the entire mass flow which escapes over the knives of the shroud (sink) and a is simply the ratio squared of the channel widths. The variable u is the stator trailing edge velocity near the upper wall in the half-plane and p is defined by equation (5.2). Both u and p can not be found without the aid of an additional equation. Equation (5.4) gives the value of p.

$$\frac{d}{H_s} = \frac{2}{\pi}\left[Tanh^{-1}\left(\frac{1}{p}\right) - \frac{1}{\sqrt{a}}Tanh^{-1}\left(\frac{1}{p\sqrt{a}}\right)\right] \tag{5.4}$$

Equation (5.4) comes from the derivation of the above equations. The distance from the trailing edge of the stator to the mean radius of the leading edge of the rotor is given by d. All the values of the variables are known in equation (5.4) except for p. An iteration scheme is used to solve for p and once p is found then the ratio of the axial velocities can be determined. Equation (5.2) then can be used to find u if one desires.

The geometry found in this shrouded turbine test facility is as follows:

$$d = 7.493 \text{ mm} = 0.295 \text{ in}$$

$$H_s = 23.48 \text{ mm} = 0.9245 \text{ in}$$

$$B_H = 16.6 \text{ mm} = 0.654 \text{ in}$$

Therefore, the value of a is 2.061 and from iterating equation (5.4) one obtains 1.421 for the value of p. Assuming that the mass flow rate into the sink (over the knives of the shroud) is very small compared to the mass flow rate through the channel *i.e.*, $\mu << 1$, one obtains 0.7039 for the ratio of the axial velocity with blockage to the axial velocity without blockage.

$$\frac{U_{es}}{U_{0es}} = 0.7039$$

The exit pressure is found using the pressure drop across the stage as measured by the wall tap pressure ports. After performing the steps outlined above one obtains the following for the input flow conditions:

$$P_i^* = 223.9 \text{ kPa} = 32.46 \text{ psi}$$

$$P_o^* = 201.0 \text{ kPa} = 29.16 \text{ psi}$$

$$T = 291 \text{ °K} = 64 \text{ °F}$$

$$V_i^* = 29.7 \text{ m/s} = 97.4 \text{ ft/s}$$

The values used for the magnitude and phase of the inlet velocity and pressure perturbations and the magnitude and phase of the exit pressure perturbation are discussed in section 5.2. This later section describes the model's behavior to these perturbations. Therefore, presenting the inlet and exit perturbations used to calculate the final value of the direct and cross forces is left until a better understanding of these perturbations is obtained in section 5.2.

5.1.2 Geometric Inputs

The model needs certain geometric properties of the shroud. The first of these properties needed for input is the radius of the shroud. The radius is taken from the centerline to the flat outer area of the shroud (the land region). The length of this land region is the second input. The vertical height of the sealing knives is also specified.

The next two inputs are the nominal gaps at the entrance and at the exit of the shroud. These gaps are the distance between the tips of the knives to the inner casing of the facility. The eccentricity of the rotor is the next input followed by the frequency of the shaft rotation. The whirl rate is the last input. The whirl is set to zero for all the analytical tests because this theory is attempting to model the static experimental facility that is described in chapters 2 and 3.[1] The values given to the above geometric quantities are exactly those which exist in the experimental facility and are listed below.

$$R_s = 0.1345 \text{ m} = 5.296 \text{ in}$$

$$l = 0.01363 \text{ m} = 0.537 \text{ in}$$

$$h = 0.00549 \text{ m} = 0.216 \text{ in}$$

$$\delta_1^* = \delta_2^* = 0.000737 \text{ m} = 0.029 \text{ in}$$

$$\vec{r} = e = 0.000457 \text{ m} = 0.018 \text{ in}$$

$$\omega = 360 \text{ rad/s}$$

$$\Omega = 0.0 \text{ rad/s}$$

5.1.3 The Computer Code

The solution to the model's system of equations is done via a FORTRAN code. This code is located in Appendix B and when used to simulate Millsaps tests it is capable of reproducing his results exactly.[17] First, the code reads in all of the flow and geometric properties from an input file. The magnitude and phase of the inlet and exit pressure and velocity perturbations are specified in the code. The phase of the inlet velocity perturbation is taken at the location of the minimum value of the inlet pressure or 180° out of phase with the phase of the inlet pressure perturbation. From Bernoulli's equation

$$\tfrac{1}{2}\rho_i V_i^{*2} + P_i^* = \tfrac{1}{2}\rho_i\left[V_i^*\left(1+\hat{\eta}_i\right)\right]^2 + P_i^*\left(1+\hat{\xi}_i\right) \tag{5.5}$$

[1]This theory is capable of dynamic results by simply inputting a whirl frequency other than zero.

it is found that the magnitude of the velocity perturbation is given by:

$$\left|\hat{\eta}_i\right| = \frac{-P_i^*}{\rho_i V_i^{*2}}\left|\hat{\xi}_i\right| \tag{5.6}$$

Substituting the values for P_i^*, ρ_i and V_i^* one finds that the magnitude of the velocity perturbation is -8.3975 times that of the pressure perturbation.

$$\hat{\eta}_i = -8.3975\hat{\xi}_i \tag{5.7}$$

The magnitude and phase of the inlet and exit pressure perturbations are found from the experimental data. A complete discussion of these perturbations is given in section 5.2. Zeroth order quantities are calculated next and then the iteration scheme to determine the unperturbed swirl velocity in the cavity is performed. The resulting quantities are nondimensionalized as described in section 4.4. These nondimensional quantities for the operation of the turbine at its design speed are

$\varepsilon_1 = 0.6201$	$\alpha = 1.0000$	$D = 0.1342$
$H = 0.04081$	$L = 0.1013$	$K = 0.2020$
$S = 1.641$	$W = 0.0$	$\Delta = 0.3408$
$\sigma = 0.9425$	$\Gamma = -0.005498$	

The code then sets the coefficients for the nondimensional equations (4.70) and (4.72) and then Cramer's rule is used to solve these equations for the pressure and velocity perturbations within the shroud's cavity. The normal and tangential forces are calculated via equations (4.83) and (4.84). Since the whirl is zero, these forces are referred to as the direct and cross forces. Repeat loops ("DO" loops) are set such as to repeat the code for various inlet and exit velocity and pressure perturbations in order to gain an understanding of how these perturbations affect the final solution.

5.2 Study of the Model's Sensitivity to Inlet & Exit Perturbations

In section 5.2.1, the effect the magnitude and phase of the inlet and exit perturbations have on the model's solution is presented. Section 5.2.2 calls upon what is learned in section 5.2.1 and what is shown in section 3.2 in order to set the correct inlet and exit perturbations such as to model the conditions that exist in the experimental facility. The values of the direct force and cross force at the design condition are then predicted by this theory.

5.2.1 The Study

The code is set to output the direct and cross forces to two respective output files for the extent of the study. The repeat loops in the code are set such as to begin calculations with zero magnitude for both the inlet and exit perturbations. There are three nested loops. The outermost loop simply controls whether the inlet perturbation or exit perturbation is investigated. If the effect of the magnitude and phase of the inlet perturbation is under investigation then the magnitude of the exit perturbation is set to zero and *vice versa*. The middle loop varies the magnitude of the perturbation which is under investigation. Magnitudes are varied from 0.0 to 0.005 in 0.001 increments. The innermost loop increments the phase through sixteen angles from zero degrees to 360 degrees in 22.5 degree increments (0°, 22.5°, 45°,...,360°). For magnitudes of zero a change in phase does not effect the final results. This study shows how the direct force and cross force are affected by inlet and exit perturbations for any phase and for a wide range of magnitudes.

The results of this study are plotted in Figures 5.1 through 5.4. Each figure is a plot of either the direct or cross force versus the phase and contains six curves for each of the six magnitudes mentioned previously. As one might expect, the phase of a particular perturbation which has the largest effect on the direct force gives no effect on

the cross force (*i.e.* for the inlet nonuniformity this occurs at 26° & 206° and for the exit nonuniformity this occurs at 9° & 189°) and *vice versa.*

Figures 5.1 and 5.2 show the effect the inlet pressure and velocity perturbations have on the direct and cross forces. Note that in these two figures the exit perturbation is set to zero so that the effect of the inlet nonuniformities may be analyzed without any other effects occurring at the same time. The phase of the inlet pressure perturbation as determined from experiment is found in Figures 3.15 and 3.16. The experimental work shows a phase of 337.5° whose location on the theoretical graphs is illustrated by the vertical line in both Figures 5.1 and 5.2. The magnitudes of the direct force ($F_x = -7.987\text{N}$) and the cross force ($F_y = 11.642\text{N}$) obtained via the pressure effect experimental work is illustrated by a horizontal line in the respective figures. It is seen from these two figures that the existence of the pressure nonuniformity at the inlet of the shrouded turbine at a phase of 337.5° acts to increase the direct force in the negative direction (restoring) and acts to increase the cross force in the positive direction (destabilizing). This is an extremely important result because previous theoretical calculations, which under-predicted experimental results by 200%, ignored inlet and exit nonuniformities. The inclusion of these nonuniformities improves predictions.

The nonuniformity at the exit of the shroud also plays a very large role in altering the prediction of the direct and cross forces. Figures 5.3 and 5.4 are a graph of the direct and cross force vs. phase for six magnitudes of the exit pressure perturbation. As in the case of the inlet nonuniformity, when analyzing the exit perturbations and there effect on the forces the inlet perturbation is set to zero. Finding the actual phase of the exit perturbation as it exists in the experimental facility is a little more difficult than in the previous case. The wall tap pressure readings at station 8 (Figures 3.23 and 3.24), which is at the exit of the shroud, are not repeatable. The wake region behind the shroud is probably responsible for this scatter since experimentation at station 8 with the unshrouded turbine show repeatable results and the nonuniformity pattern present at

the other five stations are clearly visible at this station.[15] Experimentally the phase at station 4 is shown to be 337.5°, the phase at station 7 is shown to be 304.5° and the phase at station 9 is shown to be 267.2°. Figures 3.27 and 3.28 show this progression and indicate that as the flow travels from the inlet of the shroud to the exit of the shroud the phase of the pressure and velocity nonuniformity rotates. Therefore, station 8, which is at the immediate exit of the shroud, should have a phase somewhere in between that of station 7's phase and station's 9 phase. Figure 5.3 and 5.4 indicate this region with a bold box. Basically, as is seen in Figure 5.3, the direct force is very sensitive to the value of the phase within this region. However, the cross force (Figure 5.4) is near the maximum effect, therefore, the sensitivity to a change in phase is very small.

The above explanation along with the four figures show that the model must incorporate inlet and exit perturbations as they have a large effect on the model's prediction of both the direct and cross forces.

5.2.2 Simulating the Experimental Facility

The flow and geometric conditions used in the study above are those that exist in the experimental facility. However, the exact values for the inlet and exit perturbations have yet to be defined. One may already understand what values are used for these parameters, however, they are formally defined in this section.

The inlet phase for the pressure perturbation is 337.5° as is mentioned in section 5.2.2. The magnitude of this perturbation is found from Figures 3.15 and 3.16 (which gives $P_i - P_i^* = 0.1$ psid) and the absolute concentric pressure at station 4 (which gives $P_i^* = 30.67$ psi). Equation (5.2) illustrates how this magnitude is calculated.

$$\left|\hat{\xi}_i\right| = \frac{P_i - P_i^*}{P_i^*} \tag{5.2}$$

The value of this magnitude is $\left|\hat{\xi}_i\right| = 0.003260$.

An interpolation is used to find the exit conditions. It is mentioned in section 5.2.1 that the phase of the exit pressure perturbation is somewhere between 304.5° and 267.2°. The distance between station 7 and station 8 is 0.75 inches and the distance between station 8 and station 9 is 1.275 inches. Using a linear interpolation one can obtain a reasonable phase for that which may exist at station 8. From this calculation, a phase of 290.7° is taken for the pressure perturbation at station 8, the exit of the shroud. The same reasoning is applied to finding the magnitude of this nonuniformity. The value of $P - P^*$ at station 7 is 0.3425 psid and the value of $P - P^*$ at station 9 is 0.06 psid. The average value of the absolute concentric pressure is $P_o^* = 28.16$ psi. Applying the interpolation scheme and equation (5.3),

$$\left|\hat{\xi}_o\right| = \frac{P_o - P_o^*}{P_o^*} \tag{5.3}$$

one obtains $\left|\hat{\xi}_o\right| = 0.008251$ for the magnitude of the exit pressure perturbation. Figures 5.5 and 5.6 illustrate this probable phase region at the exit of the shroud. These figures are similar to the previous four figures that were used in the study, however, the new figures concentrate on the phase region between 265° and 305° and for exit perturbation magnitudes of 0.002131 (Station 9) to 0.012164 (Station 7). There is one other important change in Figures 5.5 and 5.6. The inlet pressure and velocity perturbations are **not** zero. These nonuniformities are set to the actual inlet conditions that exist in the experimental facility and which are defined in the previous paragraph. These figures are meant to illustrate the extent to which the exit perturbations may alter the results. With wall tap pressure experimental results having values of $F_x = -7.987$N for the direct force and $F_y = 11.642$N for the cross force these figures show that the model has potential in almost exactly predicting the direct and cross forces. However, as previously mentioned the actual exit magnitude is taken as $\left|\hat{\xi}_o\right| = 0.008251$ and the actual phase is taken to be 290.7°. These values cause the model's results to fall short of the wall tap pressure results as is illustrated in chapter 6.

The following summarizes the inlet and exit nonuniformity conditions.

$$\psi_{\xi_i}=337.5° \qquad \left|\hat{\xi}_i\right|=0.003260$$

$$\psi_{\xi_o}=290.7° \qquad \left|\hat{\xi}_o\right|=0.008251$$

These numbers are used in a modified version of the previously explained computer code to arrive at a final value for the direct and cross forces for both the design and off-design conditions. These results are compared in chapter 6 to the experimentally determined results of chapter 3.

5.3 Theoretical Results

The experimental work determines the input parameters to the model. These values for the design condition are listed in the previous sections of this chapter. The model is also tested for the off design conditions, $0.7\omega_D$ and $1.1\omega_D$. The off design dynamometer tests provide the flow information for these tests, however, the values for the inlet and exit perturbations are taken from the design results, since certain off design flow conditions are not available. The flow conditions are listed in Table 5.1; notice that the design values are identical to those presented in section 5.1.1.

Table 5.1: Flow Conditions for the Three Cases

$\frac{\omega}{\omega_D}$	P_i^* kPa (psi)	P_o^* kPa (psi)	T °K (°F)	V_i^* m/s (ft/s)
0.7	224.0 (32.49)	201.1 (29.17)	291 (64)	29.9 (98.0)
1.0	223.9 (32.47)	201.0 (29.16)	291 (64)	29.7 (97.4)
1.1	223.9 (32.47)	201.1 (29.17)	292 (66)	29.9 (98.0)

Table 5.2 lists the results from applying the analytical model via the FORTRAN code with all the above flow, geometric and nonuniformity information.

Table 5.2: Direct and Cross Forces Determined by the Model

$\frac{\omega}{\omega_D}$	F_x N (lbf)	F_y N (lbf)
0.7	-7.383 (-1.660)	8.836 (1.986)
1.0	-7.372 (-1.657)	8.486 (1.908)
1.1	-7.380 (-1.659)	8.390 (1.886)

These forces are nondimensionalized by equations (1.17) and (1.18). Once again, the mean radius is R_m = 125 mm (4.932 in) and the blade height is B_H = 16.6 mm (0.652 in). The eccentricity has been set to e = 0.457 mm (18 mils). The torque values are listed in Table 5.3 and next to these torque values are the results of the nondimensionalization.

Table 5.3: Model's Torque and Direct & Cross Coefficients

$\frac{\omega}{\omega_D}$	T_Q N·m (lbf·in)	β_x	β_y
0.7	23.52 (208.2)	-2.75	3.41
1.0	18.35 (162.4)	-3.65	4.20
1.1	17.11 (151.4)	-3.78	4.45

Chapter 6 compares all the results presented in this chapter with those presented in Chapter 3.

5.4 Final Notes

It is interesting to understand how the direct force, F_x, comes about. For the case in which the inlet and outlet seal effective gaps, δ_1^* & δ_2^*, are identical (as are the geometrical gaps in our seal) and in the absence of a carryover effect one would predict nearly zero direct force. It is only the allowance for variations of the carryover coefficient that introduces direct forces of the correct order of magnitude, as shown in Tables 5.2 and 5.3.

Regarding the cross-force F_y, the usual Alford mechanism must be still active, although in reduced form, in this shrouded turbine. Indeed, as long as a fraction of the surviving flow can escape through the seal gap without doing work, the Alford mechanism remains in place. Once again, this can be explained by the fact that there will be less work lost in the regions where the gap is reduced by the offset, and *vice versa*

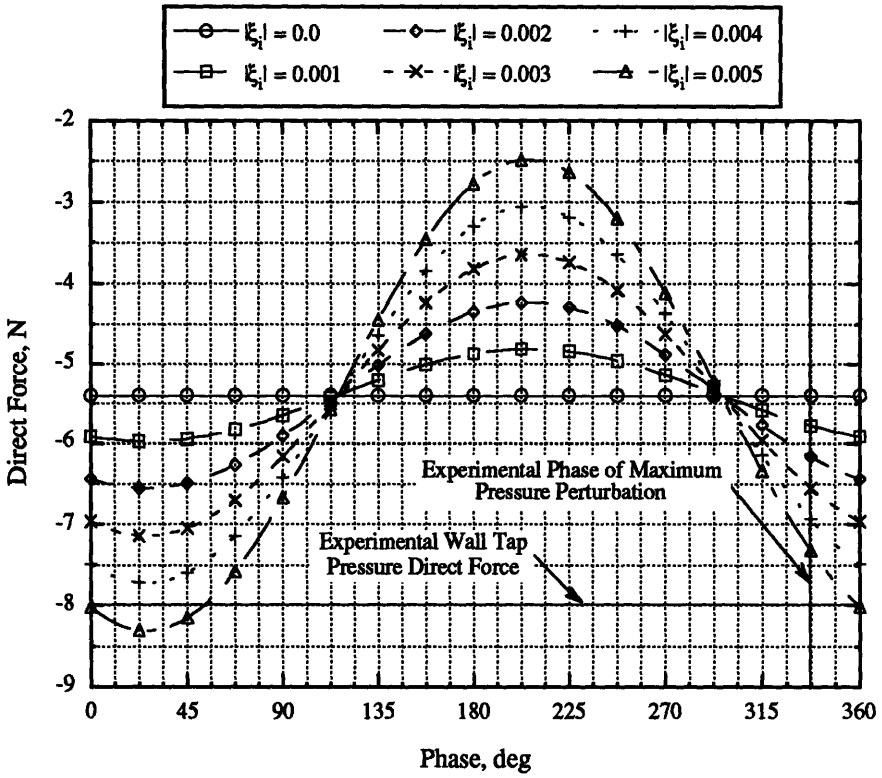

Figure 5.1: Value of the Direct Force for a Given Phase and Magnitude of the Inlet Pressure Perturbation. Exit Magnitude is Set to Zero.

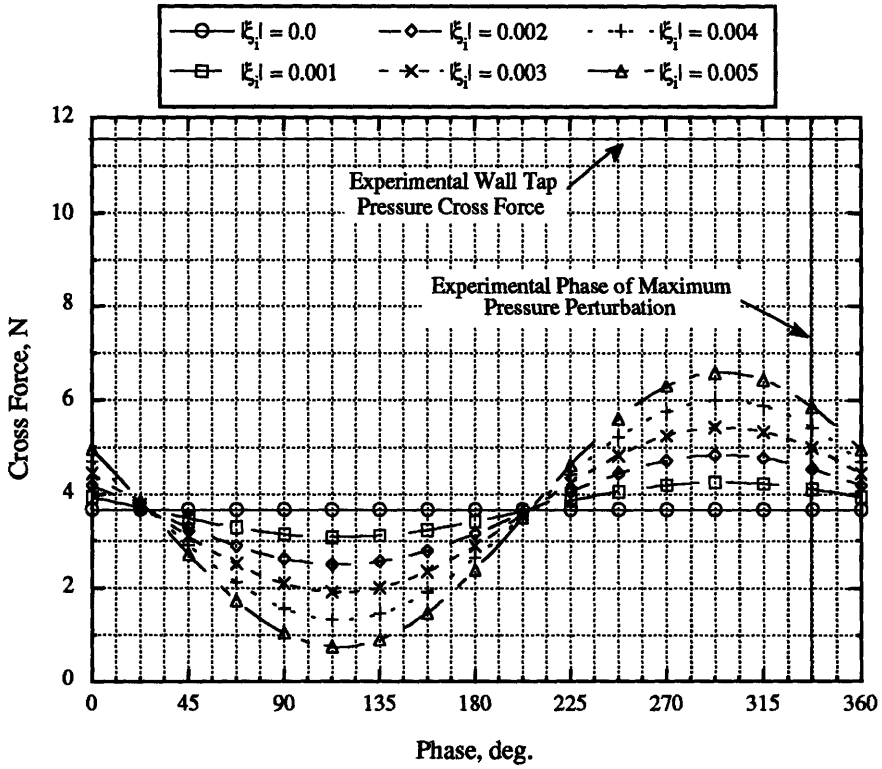

Figure 5.2: Value of the Cross Force for a Given Phase and Magnitude of the Inlet Pressure Perturbation. Exit Magnitude is Set to Zero.

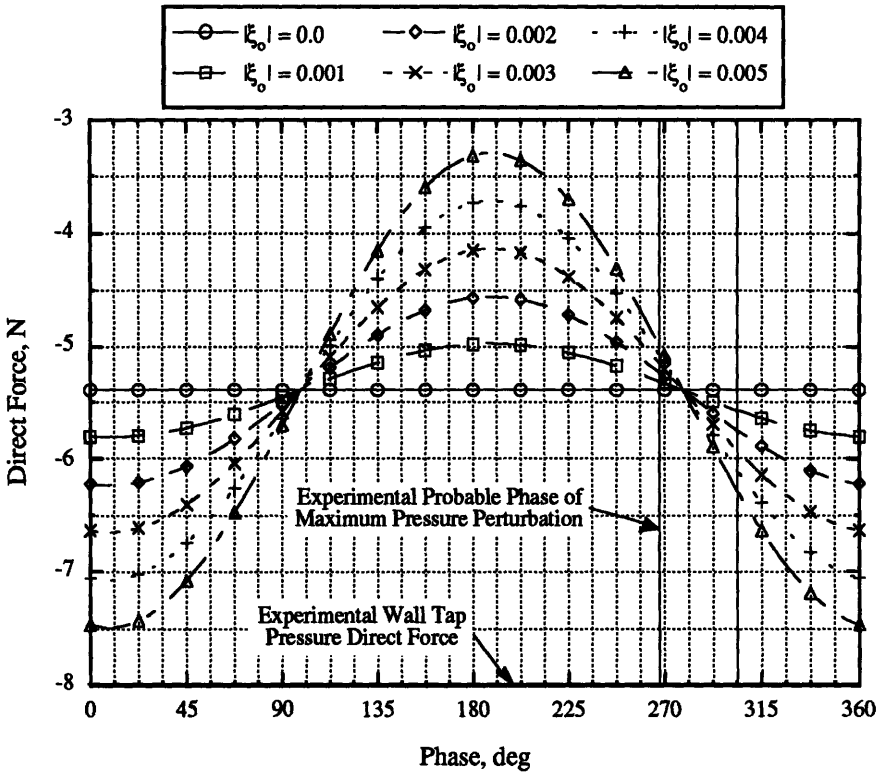

Figure 5.3: Value of the Direct Force for a Given Phase and Magnitude of the Exit Pressure Perturbation. Inlet Magnitude is Set to Zero.

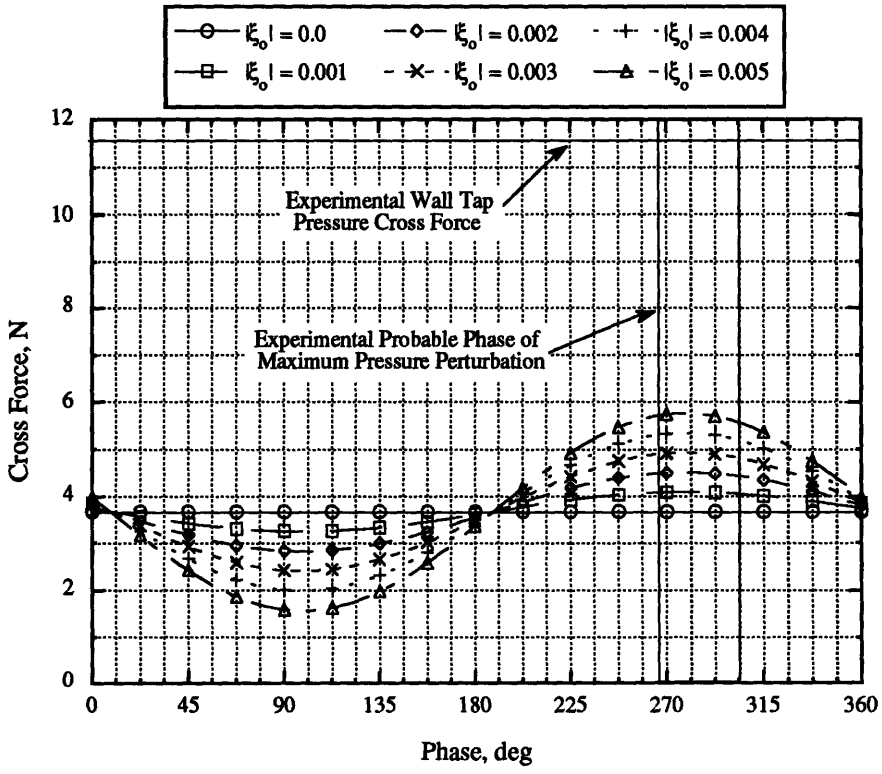

Figure 5.4: Value of the Cross Force for a Given Phase and Magnitude of the Exit Pressure Perturbation. Inlet Magnitude is Set to Zero.

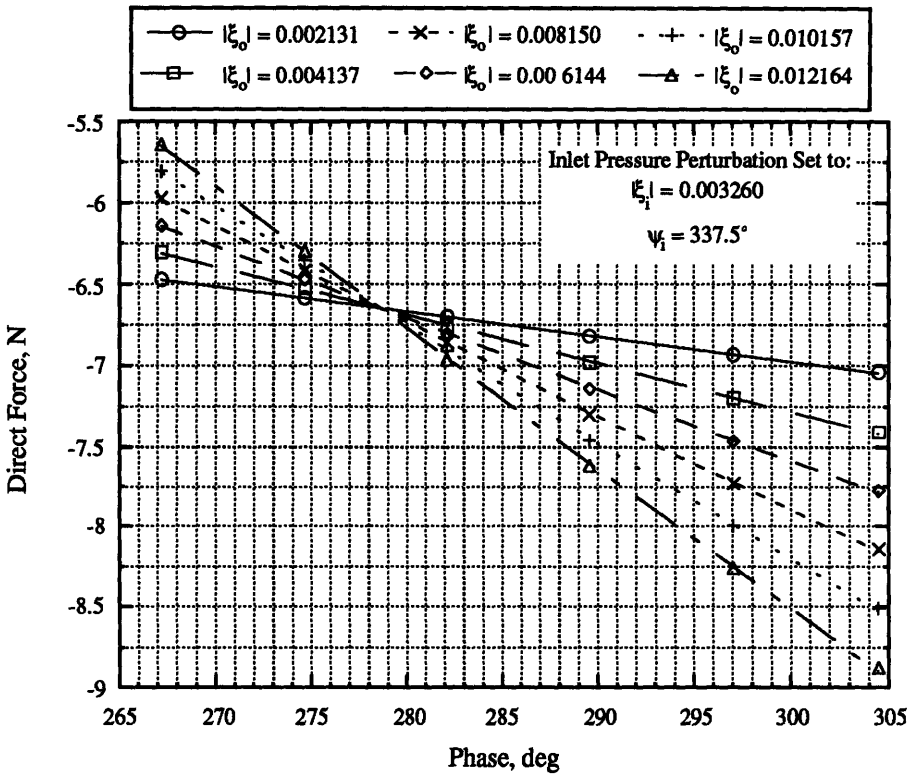

Figure 5.5: Value of the Direct Force for the Probable Phase Locations and Possible Magnitudes of the Exit Pressure Perturbation.

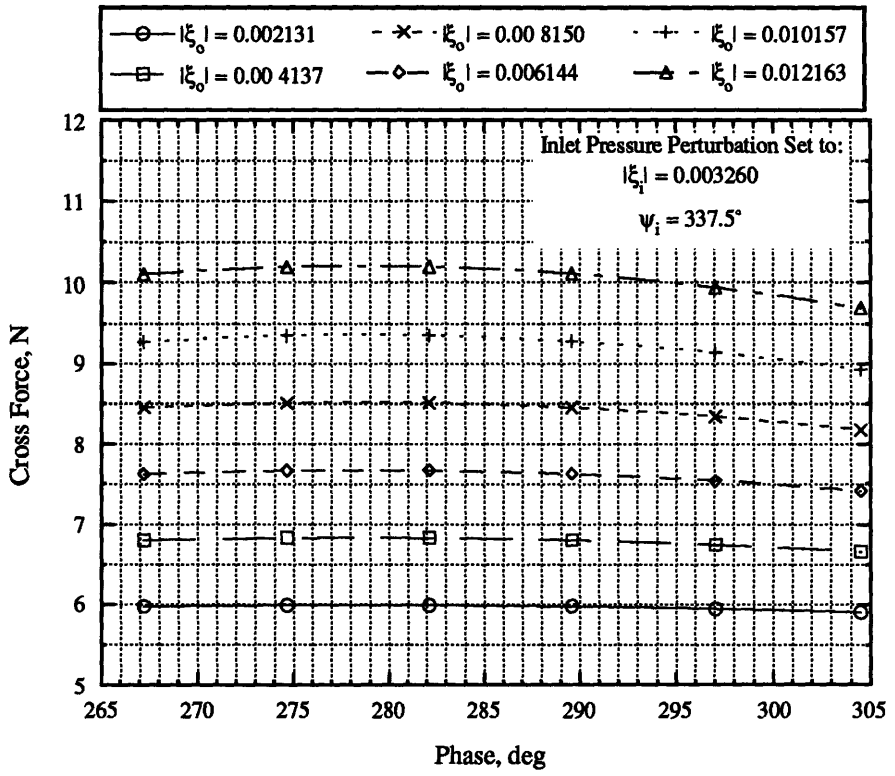

Figure 5.6: Value of the Cross Force for the Probable Phase Locations and Possible Magnitudes of the Exit Pressure Perturbation.

Chapter 6

Comparison of Results

6.1 Dynamometer, Wall Tap Pressure & Analytical Results

In Table 6.1 and 6.2 the average experimental results from Tables 3.3 (dynamometer results), Table 3.6 (wall tap pressure results) and the theoretical results are compared. Table 6.1 compares the direct force coefficients while Table 6.2 compares the cross force coefficients. The first column of each table lists the speed, the second column lists the dynamometer results, the third column contains the wall tap pressure results and the last column presents the results from the analytical model.

Table 6.1: Direct Force Coefficients Compared

$\frac{\omega}{\omega_D}$	β_x Dynamometer	β_x W.T.P.	β_x Theory
0.7	-4.06	-	-2.75
1.0	-5.63	-3.95	-3.65
1.1	-6.00	-	-3.78

Table 6.2: Cross Force Coefficients Compared

$\frac{\omega}{\omega_D}$	β_y Dynamometer	β_y W.T.P.	β_y Theory
0.7	5.94	-	3.41
1.0	6.28	5.75	4.20
1.1	6.37	-	4.45

The agreement between the dynamometer measured direct force and the wall tap pressure determined direct force is not good. Also, it is believed that the absence of the Alford effect in the wall tap pressure measurements is not the cause of this discrepancy. Song has successfully measured the aerodynamic forces (The Alford Effect) in the facility for the unshrouded turbine and has found that the direct force contribution by these forces is very small.[21] The theoretical models developed by Martinez and Yoo to explain the Alford effect show no contribution to the direct force.[15] However, the agreement between the wall tap pressure results and the analytical model is very good. There is, however, one other item which one should note. Millsaps found that the direct force is sensitive to many parameters and a slight change in one of those parameters can alter the direct force dramatically.[17] The sensitivity of the direct force to certain parameters is also shown in chapter 5 of this work. Figure 5.3 shows that for the magnitudes investigated an error in the knowledge of the phase of 10° at the exit of the shroud can alter the predicted direct force up to 0.6 N.

It is fortunate, however, that the direct force is not the result which is of most importance in this work. The cross force is the destabilizing force and from its measurement one may obtain the stiffness terms responsible for instability as is shown in equation (1.10). Once again, Table 6.2 compares the cross force coefficients. It is seen in this table that the cross force determined from the wall tap pressure measurements slightly under predicts the cross force as measured by the dynamometer. However, one expects the wall tap pressure results to under predict the cross force because the aerodynamic forces (The Alford Effect) are not taken into account in these wall tap pressure results. Similarly, the Alford effect is not taken into account in the theory. This analytical model simply predicts the pressure perturbation within the cavity of the shroud and says nothing about the aerodynamic forces. At this point the only discrepancy worth noting, is that the theoretical cross force result should match

wall tap pressure results exactly. The error may be do to a wrong choice of the exit phase and magnitude when specifying the input parameters for the theoretical results. It is shown in Figure 5.6 that the cross force may have magnitudes of up to 10.25 N which gives a cross force coefficient of $\beta_y = 5.07$. This may be compared to the wall tap pressure result of $\beta_y = 5.75$. Therefore, the refinement of the theory shown in this work has strong potential of being a good predictor of the pressure perturbation within the cavity of a shroud.

Before anything else is said, the effect of the aerodynamic forces (The Alford Effect) are added to the wall tap pressure results and the theoretical results in the following section.

6.2 Adjustment of Results for Work Loss

Work loss specifies the amount of work the machine foregoes due to leakage over the tips of the blades. This is the Alford effect. As mentioned in section 1.4.2, the Alford effect is minimal in a shrouded turbine compared to an unshrouded turbine because tip leakage is reduced by the shroud. A theory has been developed by Martinez and Yoo to estimate these Alford forces.[15] Only the results of this theory are presented in this work and one should refer to reference [15] for a complete explanation.

In reference [15] chapter 9, the simplest version of the theory is applicable for this shrouded turbine. In this theory [ref. 15, Section 9.2] the fluid which escapes through the gap at the blade tips is taken to do no work at all. This is inappropriate for unshrouded blades, and is corrected in Sec. 9.3 of reference [15], but it fits exactly the condition in a turbine with a shroud of the type that is in this work. The only modification is the inclusion of a factor $\frac{1}{\sqrt{2}}$ in the final β_y result, to account for the fact that the flow rate through a 2-strip seal is $\frac{1}{\sqrt{2}}$ of that through a single gap with the same pressure differential.

The results of applying this scheme to the cross force results are shown in Table 6.3. Note, as mentioned above, that this simple form of the work loss theory predicts zero direct force.

Table 6.3: Comparison of the Cross Force Coefficients with the Inclusion of the Work Loss Terms in the W.T.P. and Theory Results

$\frac{\omega}{\omega_D}$	β_y Work Loss	β_y Dynamometer	β_y W.T.P. +Work Loss	β_y Theory +Work Loss
0.7	0.76	5.94	-	4.17
1.0	0.85	6.28	6.60	5.05
1.1	0.92	6.37	-	5.37

The agreement between the dynamometer measured cross force and the modified wall tap pressure results is excellent. The theoretical results have been brought closer to the measured dynamometer results and if a larger magnitude of the exit pressure perturbation exists than is actually assumed, the agreement between the theory and the dynamometer results become even better.

6.3 Magnitude of Nonlinear Terms in the Analytical Model

As is seen in the previous two sections there is a discrepancy between the analytical model results and the experiment results. In this section the nonlinear system of governing differential equations (equations (4.14) and (4.15)) are first reorganized and then solved numerically to see whether the exclusion of the nonlinear terms in the analytical model affects the results.

First, since the static case is of interest, the terms in the governing differential equations containing temporal derivatives are dropped. This results in the following system of ordinary differential equations:

$$\frac{1}{R_s}\frac{\partial\left[\rho V l(h+\delta)\right]}{\partial\theta}+q_2-q_1=0 \tag{6.1}$$

$$\frac{1}{R_s}\frac{\partial\left[\rho V^2 l(h+\delta)\right]}{\partial\theta}+q_2V-q_1V_i+\tau_s l-\tau_r(l+2h)+\frac{l(h+\delta)}{R_s}\frac{\partial P}{\partial\theta}=0 \tag{6.2}$$

The density gradient is given by:

$$\frac{\partial\rho}{\partial\theta}=\frac{1}{a_s^2}\frac{\partial P}{\partial\theta} \tag{6.3}$$

Equation (6.3) is then substituted into equations (6.1) and (6.2). The convective form of the momentum equation is then obtained by taking equation (6.2) and subtracting V times equation (6.1). The resulting equations can be neatly expressed in matrix form as is shown in equation (6.4).

$$\frac{l(h+\delta)}{R_s}\begin{bmatrix}\frac{V}{a^2} & \rho\\ 1 & \rho V\end{bmatrix}\begin{bmatrix}\frac{dP}{d\theta}\\ \frac{dV}{d\theta}\end{bmatrix}=\begin{bmatrix}-\frac{l}{R_s}\rho V\frac{d\delta}{d\theta}-q_2+q_1\\ -q_1(V-V_i)-\tau_s l+\tau_r(l+2h)\end{bmatrix} \tag{6.4}$$

Solving this system for both $\frac{dP}{d\theta}$ and $\frac{dV}{d\theta}$ via Cramer's rule one obtains the following two equations.

$$\frac{dP}{d\theta}=\frac{V\left[-\frac{l}{R_s}\rho V\frac{d\delta}{d\theta}-q_2+q_1\right]-\left[-q_1(V-V_i)-\tau_s l+\tau_r(l+2h)\right]}{\frac{l(h+\delta)}{R_s}\left[\frac{V^2}{a_s^2}-1\right]} \tag{6.5}$$

$$\frac{dV}{d\theta}=\frac{\frac{V}{a_s^2}\left[-q_1(V-V_i)-\tau_s l+\tau_r(l+2h)\right]-\left[-\frac{l}{R_s}\rho V\frac{d\delta}{d\theta}-q_2+q_1\right]}{\rho\frac{l(h+\delta)}{R_s}\left[\frac{V^2}{a_s^2}-1\right]} \tag{6.6}$$

The above two ordinary differential equations are required to satisfy the following periodic boundary conditions.

$$P(\theta)=P(\theta+2\pi) \tag{6.7}$$

$$V(\theta) = V(\theta + 2\pi) \tag{6.8}$$

In general boundary value problems are harder to solve numerically than initial value problems. In order to solve this system of ordinary differential equations with the periodic boundary conditions a shooting method is desired. A "pure" shooting technique (section 16.1 in reference [19]) was attempted, however, this technique proved to be unstable for these equations and their respective periodic boundary conditions. Therefore, a routine is used which assumes thousands of combinations of guesses for the velocity and pressure boundary conditions. The velocity guesses range from 27.0 m/s to 32.0 m/s in 0.1 m/s intervals and the pressure guesses range from 212438 Pa to 217438 Pa in 1 Pa intervals. These guesses are used to solve the ordinary differential equations via a fourth order Runge-Kutta initial value integration routine for one hundred points around the circumference. Once again, the technique proves to be unstable and very sensitive to the guesses for both the velocity and pressure at the boundaries. However, with a lot of patience and much manipulation it is found that the swirl velocity at the boundary ($\theta = 0, 2\pi$) is approximately 29.0 m/s and the pressure at the boundary ($\theta = 0, 2\pi$) is approximately 212570 Pa. Equations (6.7) and (6.8) are not satisfied perfectly with these values for the boundary conditions, however, the boundary value at $\theta = 0$ compared to the boundary value at $\theta = 2\pi$ are within 1% of each other.

The result of this code predicts a maximum value of pressure at 287° with a maximum pressure perturbation of 950 Pa (0.138 psi). This is the case for a zero perturbation in pressure and velocity at the inlet and at the exit ($\xi_i = 0, \eta_i = 0, \xi_o = 0$) of the shroud. This case is easier to solve and provides the information needed to see whether nonlinear effects are present. The nonlinear results, with zero inlet and exit perturbations, can be compared to the linearized model with the same inlet and exit conditions. It is found that the nonlinear model under predicts the magnitude of the

pressure perturbation compared to the experimentally found pressure perturbation by 2.4 times. This is very close to the linearized model, which for zero inlet and exit nonuniformities, under predicts the magnitude of the pressure perturbation compared to the experimentally found pressure perturbation by 2.2 times. The small discrepancy between the linear and nonlinear models may be attributed to the small error in picking the appropriate boundary conditions in the nonlinear model and the model's sensitivity to these boundary conditions.

This small numerical experiment shows that the discrepancy between the theoretical model and the experimental results is not due to the exclusion of the nonlinear terms in the analytical model.

6.4 Final Comments

The dynamometer results are very repeatable for tests taken on the same day with repeatability getting slightly worse when dynamometer test results from different days are compared. However, the dynamometer results should be used as the standard for comparison between all other types of measurements and analytical calculations. The sensitive behavior of the direct force is shown in this work which reinforces the trends illustrated by the direct force in Millsaps [17] work. The wall tap pressure measurements give excellent cross force results and the theoretical model has once again been improved. This model showed that the direct force may be sensitive to the phase of the exit pressure perturbation. However, even with the improvements the model still under-predicts the experimental results and the exclusion of the nonlinear terms in the analytical model are not the cause of the discrepancy.

The final chapter lists the conclusions of this work and then gives a list of recommendations to aid in future research in this field and on the experimental facility.

Chapter 7

Conclusions and Recommendations

7.1 Conclusions

1) Forces measured in the shrouded turbine are larger than the forces measured in the unshrouded turbine by approximately a factor of two.

2) The nonuniformity in the pressure in the cavity of the shroud produces a direct and cross force which are both smaller in magnitude than those measured with the dynamometer. The discrepancy in the direct force can not be explained and is not due to the absence of the aerodynamic forces (The Alford Effect) in these measurements. The small discrepancy in the cross force is explained by the aerodynamic forces and once this Alford force is taken into account the agreement between the dynamometer cross force and the pressure and aerodynamic forces is very good.

3) The discrepancy between the dynamometer and wall tap pressure results prove the existence of the Alford force.

4) Compared to the unshrouded turbine in the shrouded turbine the Alford effect is smaller and the pressure effect is larger.

5) A nonuniformity in pressure and velocity exists at the inlet to the shroud.

6) A nonuniformity in pressure exist at the exit to the shroud.

7) The analytical model predicts that the inlet and exit nonuniformities have a large effect on the prediction of the magnitude of the pressure and velocity perturbation within the cavity of the shroud.

8) The direct force is sensitive to the phase of the exit pressure perturbation which may be one of the causes for erratic results when these direct forces are considered.

9) The discrepancy between the theoretical model and the experimental results is not due to the exclusion of the nonlinear terms in the analytical model.

7.2 Recommendations

This section contains recommended procedures in operating the facility, needed facility changes, further experimental work and further theoretical work.

1) To test whether density changes are responsible for the decrease in repeatability two test series at 2.21 atm should be repeated, however, making sure that the loop is completely (following the procedure explained in section 2.2.3) evacuated before pressurizing with freon.

2) Immediately following the use of the LeCroy, for sampling the forces via the dynamometer, one should obtain the pressure readings from the Scanivalve system. From the Scanivalve readings one may obtain all the absolute pressure levels in the test section. These pressure levels are useful for the reduction of the data.

3) A study of off the shelf velocity probes should be done such that a probe can be found which has its measuring ports at the tip. This would allow one to measure the rotor exit velocity at practically all radial locations in order to calculate the aerodynamic forces (The Alford Effect). The probes which are in the facility at this time contain measuring ports which are too far down the length of the probe, therefore,

a complete rotor exit velocity profile can not be taken. Thus, the Alford effect can not be measured.

4) Wall tap pressure experiments should be carried out at the off design conditions.

5) An extension of the analytical model should be developed which is able to predict the inlet and exit pressure and velocity nonuniformities, rather than having these nonuniformities as inputs and relying on the experimental results for these perturbations.

References

[1] Alford, J. S., "Protecting Turbomachinery From Self-Excited Rotor Whirl," Journal of Engineering for Power, Oct 1965, pp. 333-344.

[2] Beckwith, T. G., Buck, N. L., Marangoni, R. D., Mechanical Measurements, Third Edition, Addison Wesley Publishing Company, 1982.

[3] Celorio-Villasenor, A., "Analysis of Disturbing Aerodynamic Forces in Labyrinth Seals," Master of Science Thesis, Department of Aeronautics and Astronautics, Massachusetts Institute of Technology, September 1982.

[4] Childs, D., "Rotordynamic Characteristics of the HPOTP (High Pressure Oxygen Turbopump) of the SSME (Space Shuttle Main Engine)," Turbomachinery Laboratories Report under NASA contract NAS8-34505, Texas A&M University, Jan. 30, 1984.

[5] Den Hartog, J. P., Mechanical Vibrations, Dover Edition, Dover, 1985, pp. 282-334.

[6] Dixon, S. L., Thermodynamics of Turbomachinery, Third Edition, Pergamon Press, 1978.

[7] Dugundji, J., Buellesbach, M. M., Wright, M. A., "Some Observations of the Vibration of Slender Rotating Shafts," GT&PDL Report No. 163, March 1982.

[8] Ehrich, F., and Childs, S. D., "Self-Excited Vibrations in High-Performance Turbomachinery," Mechanical Engineering, May 1984, pp. 66-79.

[9] Iwatsubo, T., "Evaluation of Instability Forces of Labyrinth Seals in Turbines or Compressors", NASA C.P. 2133, 1980, pp. 139-169.

[10] Jery, B., "Experimental Study of Unsteady Hydrodynamic Force Matrices on Whirling Centrifugal Pump Impellers," Ph.D. Thesis, Division of Engineering and Applied Science, California Institute of Technology, 1985.

[11] Jery, B., Qiu, Y., Martinez-Sanchez, M., and Greitzer, E., "A Facility to Study Turbine Rotor and Seal Clearance Forces," NASA conference publication no. 2436, Advanced Earth-to-Orbit Propulsion Technology, Vol. 1, 1986.

[12] Kostyuk, A. G., "A Theoretical Analysis of the Aerodynamic Forces in the Labyrinth Glands of Turbomachines", Teploenergetica, 1972, Vol. 19, No. 11, pp. 29-33.

[13] Loose, D. H., "Experimental Investigation of Rotordynamic Instabilities Caused by Rotor Blade-Tip Excitation Forces," Master of Science Thesis, Department of Aeronautics and Astronautics, Massachusetts Institute of Technology, August 1989.

[14] Martinez-Sanchez, M., Jery, B., "Volume I - Technical Proposal: Investigation of Turbine Blade-Tip Forces," Proposal for Continuation of NAS8-35018, Department of Aeronautics and Astronautics, Massachusetts Institute of Technology, December 1987.

[15] Martinez-Sanchez, M., Jery, B., "Turbine Blade Tip and Seal Clearance Excitation Forces," Phase III Report on Contract Number NAS8-35018, Department of Aeronautics and Astronautics, Massachusetts Institute of Technology, May 1992.

[16] Millsaps Jr., K. T., "Analysis of Aero-Elastic Forces in Labyrinth Seal and the Design of an Experimental Facility to Measure Them," Master of Science Thesis, Department of Aeronautics and Astronautics, Massachusetts Institute of Technology, August 1987.

[17] Millsaps Jr., K. T., "The Impact of Unsteady Swirling Flow in a Single Gland Labyrinth Seal on Rotordynamic Stability: Theory and Experiment," Ph.D. Thesis, Department of Aeronautics and Astronautics, Massachusetts Institute of Technology, May 1992.

[18] Potter, M. C., Foss, J. F., Fluid Mechanics, First Edition, Great Lakes Press, 1982.

[19] Press, W. H., Flannery, B. P., Teukolsky, S. A., Vetterling, W., T., Numerical Recipes: The Art of Scientific Computing (FORTRAN Version), First Edition, Cambridge University Press, 1986.

[20] Qiu, Y. J., "An Investigation of Destabilizing Blade Tip Forces For Shrouded and Unshrouded Turbines," Master of Science Thesis, Department of Aeronautics and Astronautics, Massachusetts Institute of Technology, August 1985.

[21] Song, S. J., Personal Communication on July 22, 1992.

[22] White, F. M., Viscous Fluid Flow, First Edition, McGraw-Hill Publishing Company, 1974.

Appendix A

Wall Tap Pressure Curve Fit Equations

This appendix contains the sinusoidal curve fit parameters for the curve fit equations that are used in Figures 3.15, 3.16. 3.19 and 3.20. These figures are at stations 4 and 6 and include test series 1 and 2 along with the seven trials in each test series. The following page begins the list of the parameters.

Station 4 Test Series 1

RADIAL 1
y = m1 + m2*sin(m0)+m3*cos(m0)

	Value	Error
m1	0.066401500565	0.00677601
m2	-0.038259355726	0.010164
m3	0.086998041981	0.010164
Chisq	0.0049587413352	NA
R	0.96518015239	NA

RADIAL 2
y = m1 + m2*sin(m0)+m3*cos(m0)

	Value	Error
m1	0.066333667335	0.00579096
m2	-0.035934634083	0.00868644
m3	0.087263231679	0.00868644
Chisq	0.0036218075745	NA
R	0.97363441075	NA

RADIAL 3
y = m1 + m2*sin(m0)+m3*cos(m0)

	Value	Error
m1	0.071956750462	0.00655253
m2	-0.038645973786	0.00982879
m3	0.090545943507	0.00982879
Chisq	0.0046370483711	NA
R	0.96933540411	NA

RADIAL 4
y = m1 + m2*sin(m0)+m3*cos(m0)

	Value	Error
m1	0.069286999836	0.00686588
m2	-0.038322895104	0.0102988
m3	0.088737534213	0.0102988
Chisq	0.0050911542555	NA
R	0.96534583776	NA

RADIAL 5
y = m1 + m2*sin(m0)+m3*cos(m0)

	Value	Error
m1	0.070085584652	0.00696835
m2	-0.045219639481	0.0104525
m3	0.092768089917	0.0104525
Chisq	0.0052442476538	NA
R	0.96900442368	NA

RADIAL 6
y = m1 + m2*sin(m0)+m3*cos(m0)

	Value	Error
m1	0.065157417596	0.00803705
m2	-0.037340503527	0.0120556
m3	0.09044046313	0.0120556
Chisq	0.0069761656928	NA
R	0.95418997869	NA

RADIAL 7
y = m1 + m2*sin(m0)+m3*cos(m0)

	Value	Error
m1	0.061654252001	0.00708557
m2	-0.037260933432	0.0106284
m3	0.092276163351	0.0106284
Chisq	0.0054221769911	NA
R	0.96488918602	NA

Station 4 Test Series 2

RADIAL 1
y = m1 + m2*sin(m0)+m3*cos(m0)

	Value	Error
m1	0.077851415651	0.00723814
m2	-0.041022524091	0.0108572
m3	0.095611594626	0.0108572
Chisq	0.0056581925443	NA
R	0.96665968951	NA

RADIAL 2
y = m1 + m2*sin(m0)+m3*cos(m0)

	Value	Error
m1	0.079255834576	0.00850171
m2	-0.036732730586	0.0127526
m3	0.095085458404	0.0127526
Chisq	0.0078061386915	NA
R	0.95247191186	NA

RADIAL 3
y = m1 + m2*sin(m0)+m3*cos(m0)

	Value	Error
m1	0.07814916658	0.00770427
m2	-0.038245869532	0.0115564
m3	0.095953878957	0.0115564
Chisq	0.0064104254226	NA
R	0.96160279997	NA

RADIAL 4
y = m1 + m2*sin(m0)+m3*cos(m0)

	Value	Error
m1	0.071070500766	0.00438758
m2	-0.037763884014	0.00658138
m3	0.094838005356	0.00658138
Chisq	0.0020790959134	NA
R	0.98674110375	NA

RADIAL 5
y = m1 + m2*sin(m0)+m3*cos(m0)

	Value	Error
m1	0.076761583594	0.00583502
m2	-0.039862289999	0.00875254
m3	0.093387272987	0.00875254
Chisq	0.0036771312248	NA
R	0.97687301782	NA

RADIAL 6
y = m1 + m2*sin(m0)+m3*cos(m0)

	Value	Error
m1	0.063260833112	0.00632668
m2	-0.03882069933	0.00949002
m3	0.094443811718	0.00949002
Chisq	0.0043229034169	NA
R	0.97313399696	NA

RADIAL 7
y = m1 + m2*sin(m0)+m3*cos(m0)

	Value	Error
m1	0.066427583574	0.00725601
m2	-0.039345755693	0.010884
m3	0.094821005023	0.010884
Chisq	0.0056861630563	NA
R	0.96549555845	NA

Station 6 Test Series 1

RADIAL 1
y = m1 + m2*sin(m0)+m3*cos(m0)

	Value	Error
m1	0.0052439160655	0.00637628
m2	-0.28655615642	0.00956443
m3	0.19209718521	0.00956443
Chisq	0.0043909562225	NA
R	0.99765833905	NA

RADIAL 2
y = m1 + m2*sin(m0)+m3*cos(m0)

	Value	Error
m1	0.0049678326283	0.0061482
m2	-0.2832591349	0.0092223
m3	0.1947989452	0.0092223
Chisq	0.0040824390968	NA
R	0.99781189102	NA

RADIAL 3
y = m1 + m2*sin(m0)+m3*cos(m0)

	Value	Error
m1	0.0032215854163	0.00602702
m2	-0.28611418271	0.00904053
m3	0.19349100431	0.00904053
Chisq	0.003923096201	NA
R	0.99791365497	NA

RADIAL 4
y = m1 + m2*sin(m0)+m3*cos(m0)

	Value	Error
m1	0.0056012505676	0.00566726
m2	-0.2834479329	0.0085009
m3	0.19612647699	0.0085009
Chisq	0.003468731347	NA
R	0.99815063583	NA

RADIAL 5
y = m1 + m2*sin(m0)+m3*cos(m0)

	Value	Error
m1	0.0022679204121	0.00658226
m2	-0.28068144572	0.00987339
m3	0.19135147195	0.00987339
Chisq	0.0046792220602	NA
R	0.99743105375	NA

RADIAL 6
y = m1 + m2*sin(m0)+m3*cos(m0)

	Value	Error
m1	0.0046054190035	0.00535761
m2	-0.28333071003	0.00803642
m3	0.1948554208	0.00803642
Chisq	0.0031000343607	NA
R	0.99833801139	NA

RADIAL 7
y = m1 + m2*sin(m0)+m3*cos(m0)

	Value	Error
m1	0.0033339168885	0.00641963
m2	-0.29027940231	0.00962944
m3	0.19241950508	0.00962944
Chisq	0.0044508556836	NA
R	0.99766844662	NA

Station 6 Test Series 2

RADIAL 1
y = m1 + m2*sin(m0)+m3*cos(m0)

	Value	Error
m1	0.0048079170908	0.00638731
m2	-0.30494211417	0.00958096
m3	0.20886487587	0.00958096
Chisq	0.0044061497613	NA
R	0.99795586793	NA

RADIAL 2
y = m1 + m2*sin(m0)+m3*cos(m0)

	Value	Error
m1	0.0058634166305	0.00576125
m2	-0.29735488158	0.00864188
m3	0.21352802591	0.00864188
Chisq	0.0035847386041	NA
R	0.99831027644	NA

RADIAL 3
y = m1 + m2*sin(m0)+m3*cos(m0)

	Value	Error
m1	0.0059544174011	0.00607056
m2	-0.30407540192	0.00910584
m3	0.20738646881	0.00910584
Chisq	0.0039799810815	NA
R	0.99813680812	NA

RADIAL 4
y = m1 + m2*sin(m0)+m3*cos(m0)

	Value	Error
m1	0.0053289175655	0.00640483
m2	-0.29910308035	0.00960724
m3	0.2117697228	0.00960724
Chisq	0.0044303555008	NA
R	0.99791520516	NA

RADIAL 5
y = m1 + m2*sin(m0)+m3*cos(m0)

	Value	Error
m1	0.0049705831334	0.00651777
m2	-0.30163465344	0.00977665
m3	0.20264225504	0.00977665
Chisq	0.0045879773416	NA
R	0.99779470712	NA

RADIAL 6
y = m1 + m2*sin(m0)+m3*cos(m0)

	Value	Error
m1	0.0049149974569	0.00590507
m2	-0.29675641288	0.00885761
m3	0.20954916493	0.00885761
Chisq	0.0037659475505	NA
R	0.99819537436	NA

RADIAL 7
y = m1 + m2*sin(m0)+m3*cos(m0)

	Value	Error
m1	0.0036860803764	0.00642483
m2	-0.30264707492	0.00963725
m3	0.20399215644	0.00963725
Chisq	0.0044580773379	NA
R	0.99787617802	NA

Appendix B

Computer Code for the Analytical Model

The FORTRAN computer code used for the parametric study of the effect the inlet and exit perturbations have on the pressure perturbations within the cavity of the shroud and on the resulting direct and cross forces is listed in this appendix.

```
C       TARAS A. PALCZYNSKI JR.
C       DEVELOPED WITH THE HELP OF
C       KNOX T. MILLSAPS JR.
C
C       SHROUD THEORY FORTRAN CODE

        IMPLICIT REAL*4 (A-H)
        IMPLICIT REAL*4 (O-W)
        REAL*4 Y(20,20),YPHI(20,20),PI
        REAL*4 EIMAG(20),ETAIMAG(20),EOMAG(20)
        REAL*4 FN(20,20),FT(20,20),FNND(20,20),FTND(20,20)
        COMPLEX X(2,2),EHAT,ETAHAT,Z(2),IMG,IMGG,DET
        COMPLEX EO,EI,ETAI
        COMPLEX C1,C2,C3,C4,C5,C6
        OPEN(UNIT=10,FILE='GEOMETRY DATA',STATUS='OLD')
        OPEN(UNIT=11,FILE='FLOW DATA',STATUS='OLD')
        OPEN(UNIT=12,FILE='SEAL SOLUTION',STATUS='NEW')
        OPEN(UNIT=13,FILE='ETA PLOT',STATUS='NEW')
        OPEN(UNIT=14,FILE='ETA PHI PLOT',STATUS='NEW')
        OPEN(UNIT=15,FILE='FORCE NORMAL',STATUS='NEW')
        OPEN(UNIT=16,FILE='FORCE TANGENTIAL',STATUS='NEW')
        OPEN(UNIT=17,FILE='FT 3-D',STATUS='NEW')

        NCNT=17
        NCNV=6
        IMGG=CMPLX(0.0,1.0)
        PI = 4.0*ATAN(1.0)

        DO 25 K=1,2

        DO 35 L=1,NCNV
        EIMAG(L)=0.0
        ETAIMAG(L)=0.0
        EOMAG(L)=0.0
        DO 45 M=1,NCNT
        FN(M,L) = 0.0
        FT(M,L) = 0.0
45      CONTINUE
```

```
 35     CONTINUE

C       EIMAG(1)=0.00585
C       ETAIMAG(1)=0.046235
C       EOMAG(1)=0.0065

        DO 15 J=1,NCNV
        DO 5 I=1,NCNT

        RADD = 2.0*FLOAT(I-1)*PI/FLOAT(NCNT-1)

        IF(K.EQ.1) THEN
        EI = EIMAG(J)*COS(RADD)+EIMAG(J)*SIN(RADD)*IMGG
        ETAI = -ETAIMAG(J)*COS(RADD)-ETAIMAG(J)*SIN(RADD)*IMGG
        EO = (0.0,0.0)
        END IF

        IF(K.EQ.2) THEN
        EO = EOMAG(J)*COS(RADD)+EOMAG(J)*SIN(RADD)*IMGG
        EI = (0.0,0.0)
        ETAI = (0.0,0.0)
        END IF

        WRITE(9,*) "I =",I," J =",J," K =",K

C
C       SET ALL CONSTANTS
C
C       UNIVERSAL GAS CONSTANT & RATIO OF SPECIFIC HEATS FOR FREON
        RFREON = 68.7587
        GAMMA = 1.12
C       UNIVERSAL GAS CONSTANT & RATIO OF SPECIFIC HEATS FOR AIR
C       RFREON = 287.04
C       GAMMA = 1.4
        CALL SETGEOM(RS,RL,H,DELST1,DELST2,R,OMGS,OMGW)
        CALL SETFLOW(PIST,POST,TEMP,VIST)

        CALL SETREST(DELST1,RL,H,CC,DH,RNURO,RMU1ST,RMU2ST)
        CALL FINDK(DELST1,RL,RK)

C       ZEROTH ORDER SOLUTION
        A = DELST1*DELST1*RMU1ST*RMU1ST*PIST*PIST
        B = DELST2*DELST2*RMU2ST*RMU2ST*POST*POST
        C = DELST1*DELST1*RMU1ST*RMU1ST
        D = DELST2*DELST2*RMU2ST*RMU2ST
        PST = SQRT((A+B)/(C+D))
        ROST = PST/(RFREON*TEMP)
        Q1ST = DELST1*RMU1ST*SQRT(PIST*PIST-PST*PST)/SQRT(RFREON*TEMP)
        Q2ST = DELST2*RMU2ST*SQRT(PST*PST-POST*POST)/SQRT(RFREON*TEMP)
        QST = Q1ST
        RNU = RNURO/ROST

        WRITE(12,*) "THE DIMENSIONAL VARIABLES"
        WRITE(12,*) 'RS=',RS,' RL=',RL,' H=',H,' DH=',DH
        WRITE(12,*) 'DELST1=',DELST1,' DELST2=',DELST2
        WRITE(12,*) 'RMU1ST=',RMU1ST,'RMU2ST=',RMU2ST
        WRITE(12,*) 'R=',R,' OMGS=',OMGS,' OMGW=',OMGW
        WRITE(12,*) 'PIST=',PIST,' POST=',POST,' VIST=',VIST
        WRITE(12,*) 'PST=',PST,' ROST=',ROST,' Q1ST=',Q1ST,' Q2ST=',Q2ST
        WRITE(12,*) 'RNURO=',RNURO,' RNU=',RNU

C       ITERATE TO FIND SWIRL IN GLAND
        VST = VIST
 10     CONTINUE
```

```
      CALL LAMDAS(VST,DH,RNU,RLAMS)
      CALL LAMDAR(VST,DH,RNU,OMGS,RS,RLAMR)
      VSTI = VST
      A = (ROST/8.0)*(RLAMS*RL-RLAMR*(RL+2.0*H))
      B = (QST+ROST*RLAMR*OMGS*RS*(RL+2.0*H)/4.0)
      C = -(QST*VIST+ROST*RLAMR*OMGS*OMGS*RS*RS*(RL+2.0*H)/8.0)
      VST = (SQRT(B**2-4.0*A*C)-B)/(2.0*A)
      ERROR = ABS(VST-VSTI)
C     WRITE(9,*) 'VST=',VST,'  ERROR=',ERROR
      IF(ERROR.LT.0.0001) GOTO 20
      GOTO 10
 20   CONTINUE

      WRITE(12,*)
      WRITE(12,*) 'A=',A,'  B=',B,'  C=',C
      WRITE(12,*) 'VST=',VST,' ERROR=',ERROR
      WRITE(12,*)

C     SET ALL NON-DIMENSIONAL PARAMETERS
      EPS1 = R/DELST1
      ALPHA = DELST2/DELST1
      CAPD = DELST1/H
      CAPH = H/RS
      CAPL = RL/RS
      CAPK = RK*DELST1/RMU2ST
      CAPS = OMGS*RS/VST
      CAPW = OMGW*RS/VST
      DELQ = QST/(DELST1*RMU1ST*ROST*SQRT(RFREON*TEMP))
      SIG = ROST*VST*DELST1/QST
      CGAM = 1.0 - (VIST/VST)

      WRITE(12,*)
      WRITE(12,*) "THE NON-DIMENSIONAL VARIABLES"
      WRITE(12,*) "EPS1=",EPS1," ALPHA=",ALPHA," CAPD=",CAPD
      WRITE(12,*) "CAPH=",CAPH," CAPL=",CAPL," CAPK=",CAPK
      WRITE(12,*) "CAPS=",CAPS," CAPW=",CAPW," DELQ=",DELQ
      WRITE(12,*) "SIG=",SIG," CGAM=",CGAM
      WRITE(12,*)

C     SET MATRIX COEFFICIENTS FOR SOLUTION
      IMG=CMPLX(0.0,-1.0)
      X(1,1)=((ALPHA*RMU2ST)/(DELQ*RMU1ST))**2+(1.0/DELQ)**2+
     &  ((SIG*CAPL)/(CAPD*GAMMA))*(1.0-CAPW)*IMG
      X(1,2)=SIG*CAPL*IMG/CAPD
      X(2,1)=((SIG*CAPL)/(8.0*GAMMA*CAPD*CAPH))*(RLAMS-RLAMR*(1.0+
     &  2.0*CAPH/CAPL)*(CAPS-1.0)*(CAPS-1.0))+(CAPL*IMG)/(DELQ*DELQ*
     &  SIG*RMU1ST*RMU1ST*CAPD)-(CGAM/(DELQ*DELQ))
      X(2,2)=1.0+(SIG*CAPL/(4.0*CAPD*CAPH))*(RLAMS-RLAMR*(1.0+2.0*
     &  CAPH/CAPL)*(1.0-CAPS))+(SIG*CAPL*IMG/CAPD)*(1.0-CAPW)
      Z(1)=((CAPK+((1.0/ALPHA)-1.0))+(SIG*CAPL*IMG*(1.0-CAPW)))*EPS1
     &  +(((ALPHA*RMU2ST)/(DELQ*RMU1ST))**2-1.0)*EO+
     &  (1.0+(1.0/DELQ)**2)*EI
      Z(2)=CGAM*EPS1+(1.0-CGAM)*ETAI-CGAM*(1.0+(1.0/DELQ)**2)*EI
      CALL SOLMAT(X,Z,EHAT,ETAHAT,DET)

C     USE EQUATION TO GET EHAT PAGE 73 MILLSAPS [16]
C     C1 = (1.0/ALPHA-1.0)+CAPK+SIG*CAPL*(1.0-CAPW)*IMG
C     C2 = 1.0+(SIG*CAPL/(4.0*CAPD*CAPH))*(RLAMS-RLAMR*(1.0+2.0*
C    &  CAPH/CAPL)*(1.0-CAPS))+SIG*CAPL*(1.0-CAPW)*IMG/CAPD
C     C3 = SIG*CAPL*IMG*CGAM/CAPD
C     C4 = 1.0/(DELQ**2)+((ALPHA*RMU2ST)/(DELQ*RMU1ST))**2+(SIG*CAPL/
C    &  GAMMA*CAPD)*(1.0-CAPW)*IMG
C     C5 = SIG*CAPL*IMG/CAPD
C     C6 = (SIG*CAPL/(8.0*GAMMA*CAPD*CAPH))*(RLAMS-RLAMR*(1.0+2.0*
```

```
C     &  CAPH/CAPL)*((CAPS-1.0)**2))-CGAM/(DELQ*DELQ)+CAPL*IMG/((DELQ**2)
C     &  *SIG*RMU1ST*RMU1ST*CAPD)
C          EHAT = (C1*C2-C3)*EPS1/(C4*C2-C5*C6)

           EHATR=REAL(EHAT)
           EHATI=AIMAG(EHAT)
           PHEHAT=ATAN2(EHATI,EHATR)

C          SET SIGNS OF THE PHASE ANGLE SUCH THAT:
C          EHATI>0 THEN PHEHAT>0
C          EHATI<0 THEN PHEHAT<0
           IF(EHATI.GT.0.0) THEN
                 IF(PHEHAT.LT.0.0) PHEHAT=-1.0*PHEHAT
           END IF
           IF(EHATI.LT.0.0) THEN
                 IF(PHEHAT.GT.0.0) PHEHAT=-1.0*PHEHAT
           END IF

           WRITE(12,*)
           WRITE(12,*) 'EHAT=',EHAT
           WRITE(12,*) 'MAGNITUDE OF EHAT =',CABS(EHAT)
           WRITE(12,*) 'PHI EHAT =',PHEHAT
           WRITE(12,*) 'ETAHAT =',ETAHAT
           WRITE(12,*) 'DET =',DET
           WRITE(12,*)

           Y(I,J)=CABS(EHAT)
           YPHI(I,J)=PHEHAT*(360.0/(2.0*PI))
           FN(I,J)=-1.0*PI*RS*RL*CABS(EHAT)*PST*COS(PHEHAT)
           FT(I,J)=-1.0*PI*RS*RL*CABS(EHAT)*PST*SIN(PHEHAT)
           FNND(I,J)=-1.0*PI*CABS(EHAT)*COS(PHEHAT)
           FTND(I,J)=-1.0*PI*CABS(EHAT)*SIN(PHEHAT)

           ANGLE = (RADD)*360.0/(2.0*PI)

C          WRITE(9,*) CABS(ETAI),',',CABS(EHAT)
C          WRITE(13,*) CABS(ETAI),',',CABS(EHAT)
C          WRITE(14,*) CABS(ETAI),',',PHEHAT*(360.0/(2.0*PI))
C          WRITE(15,*) CABS(EI),',',ANGLE,',',-1.0*PI
C     &  *RS*RL*CABS(EHAT)*PST*COS(PHEHAT),',',EI,',',ETAI
C          WRITE(16,*) CABS(EI),',',ANGLE,',',-1.0*PI
C     &  *RS*RL*CABS(EHAT)*PST*SIN(PHEHAT),',',EI,',',ETAI

 5         CONTINUE
           EIMAG(J+1)=EIMAG(J)+0.001
           ETAIMAG(J+1)=8.3975*EIMAG(J+1)
           EOMAG(J+1)=EOMAG(J)+0.001
 15        CONTINUE

           WRITE(15,*) 'ANGLE,',(EIMAG(J),',',J=1,NCNV)
           WRITE(16,*) 'ANGLE,',(EIMAG(J),',',J=1,NCNV)
           DO 6 I=1,NCNT
           RADD = 2.0*FLOAT(I-1)*PI/FLOAT(NCNT-1)
           ANGLE = (RADD)*360.0/(2.0*PI)
           WRITE(15,*) ANGLE,',',(FN(I,J),',',J=1,NCNV)
           WRITE(16,*) ANGLE,',',(FT(I,J),',',J=1,NCNV)
 6         CONTINUE

           EOMAG(1)=0.0
 25        CONTINUE

           END

C          GEOMETRY OF SEAL
```

```
      SUBROUTINE SETGEOM(RS,RL,H,DELST1,DELST2,R,OMGS,OMGW)
      REAL*4 RS,RL,H,DELST1,DELST2,R,OMGS,OMGW
      READ(10,*) RS,RL,H,DELST1,DELST2,R,OMGS,OMGW
      RETURN
      END

C     FLOW DATA
      SUBROUTINE SETFLOW(PIST,POST,TEMP,VIST)
      REAL*4 PIST,POST,TEMP,VIST
      READ(11,*) PIST,POST,TEMP,VIST
      RETURN
      END

C     REMAINING VARIABLES
      SUBROUTINE SETREST(DELST1,RL,H,CC,DH,RNURO,RMU1ST,RMU2ST)
      REAL*4 DELST1,RL,RLE,H,CC,DH,RNURO,RMU1ST,RMU2ST,ALPHA,BETA
C     CONTRACTION COEFFICIENT & MU1, MU2
      CC = 0.65
      RMU1ST = CC
      RLE=RL/0.342020143326
      ALPHA = 8.52/((RLE/DELST1) + 7.23)
      BETA = 1.0/SQRT(1.0 - ALPHA)
      RMU2ST = CC*BETA
C     HYDRALIC DIAMETER
      DH = 4.0*(H+DELST1)*RL/(2.0*(H+DELST1)+2.0*RL)
C     ABSOLUTE VISCOSITY OF FREON
      RNURO = 0.0000127
C     ABSOLUTE VISCOSITY OF AIR
C     RNURO = 0.0000173
      RETURN
      END

C     CALCULATE SENSITIVITY
      SUBROUTINE FINDK(DELST1,RL,RK)
      REAL*4 DELST1,RL,RLE,RK,A,B,C,CC
      CC = 0.65
      A = 8.52*CC*RL/(2.0*(DELST1**2))
      B = 8.52/((RL/DELST1)+7.23)
      C = RL/DELST1+7.23
      RK = A/(((SQRT(1.0-B))**3)*C*C)
      WRITE(12,*) '*********************************************'
      WRITE(12,*) 'THE SENSITIVITY K=',RK
      RETURN
      END

C     FINDS DARCY FRICTION FACTOR FOR THE WALL
      SUBROUTINE LAMDAS(VST,DH,RNU,RLAMS)
      REAL*4 VST,DH,RNU,RLAMS,RES,SGN1
      SGN1=SIGN(1.0,VST)
      RES = ABS(VST*DH/RNU)
      RLAMS = SGN1*0.3164/SQRT(SQRT(RES))
C     WRITE(12,*) 'SGN1=',SGN1,' VST=',VST,' RES=',RES,' RLAMS=',RLAMS
      RETURN
      END

C     FIND DARCY FRICITION FACTOR FOR THE ROTOR
      SUBROUTINE LAMDAR(VST,DH,RNU,OMGS,RS,RLAMR)
      REAL*4 VST,DH,RNU,OMGS,RS,RLAMR,VREL,RER
      VREL=OMGS*RS-VST
      SGN2=SIGN(1.0,VREL)
      RER=ABS(VREL*DH/RNU)
      RLAMR = SGN2*0.3164/SQRT(SQRT(RER))
C     WRITE(12,*) 'SGN2=',SGN2,' VST=',VST,' RER=',RER,' RLAMR=',RLAMR
      RETURN
```

```
      END

C     SOLVES A 2X2 COMPLEX MATRIX
      SUBROUTINE SOLMAT(X,Z,EHAT,ETAHAT,DET)
      COMPLEX X(2,2),Z(2),EHAT,ETAHAT
      EHAT=(Z(1)*X(2,2)/X(1,2)-Z(2))/(X(1,1)*X(2,2)/X(1,2)-X(2,1))
      ETAHAT=(Z(1)-X(1,1)*EHAT)/X(1,2)
      DET=X(1,1)*X(2,2)-X(1,2)*X(2,1)
      RETURN
      END
```